Analysis of the electron cyclotron heating and current drive system in the ST-F1 spherical tokamak

van de Giessen, Peter

Award date:
2021

Graduation Project ap/fusion

Department of Applied Physics

Analysis of the electron cyclotron heating and current drive system in the ST-F1 spherical tokamak

Author:
P.L. van de Giessen

Supervisors:
P. Buxton (Tokamak Energy)
S. McNamara (Tokamak Energy)
H.J. de Blank (TU Eindhoven, DIFFER)
J. van Dijk (TU Eindhoven, EPG group)

March 5, 2021

Contents

Abstract

Spherical tokamaks have various benefits as compared to conventional tokamaks. They are smaller, inherently more stable to plasma magneto-hydrodynamic instabilities, and cheaper. Due to space constraints in the centre column, the spherical tokamak configuration has little to no place for a central solenoid, leading to the necessity of non-inductive ways of driving the plasma current. Non-inductive current drive methods typically consume a lot of energy and are a significant factor in the attainable energy gain in fusion devices.
The high-field spherical tokamak ST-F1 that is in the design phase at Tokamak Energy, aims to achieve a ratio of fusion-energy/consumed energy Q_{fusion} at or larger than 3. To accomplish this goal, it needs to achieve a non-inductive current-drive efficiency that is as high as possible, with the target for $Q_{\text{fusion}} = 3$ at 0.15 A/W. For the ST-F1 spherical tokamak, the method that is currently considered for heating and non-inductive current-drive is electron cyclotron heating and current-drive. The electron cyclotron system will also be used to heat the plasma, suppress MHD instabilities and tailor the profile of the current. Understanding how well this system can drive current in different discharge scenarios, where the power is absorbed, and how much current can be driven is important for ST-F1's operation and design.
This study uses the GENRAY ray-tracing code and the coupled CQL3D Fokker-Planck code to model the power absorption, optimal current-drive efficiency, and dependence of current-drive on minor radius for different scenarios, wave frequencies, and wave launcher configurations in ST-F1. A high-performance ($Q_{\text{fusion}} = 3$), a high density and a low density scenario are taken into account. Furthermore, available frequencies and wave launcher locations are considered and scanned, to obtain the configuration with the highest current-drive efficiency. The results show that an electron cyclotron system would likely have a lower current-drive efficiency in the design point scenario. These findings are in good agreement with the theoretical and experimental findings of current-drive in conventional tokamaks.

Chapter 1

Introduction

A rise in the availability of readily deployable energy has increased the ease of living. From transportation to food and communication, every aspect of life is influenced by the fact that energy in some form is available. For the future, this trend of energy consumption increase is no different; the total energy consumption is expected to increase between $50 - 100\%$ by $2050 - 2060$ [1, 2]. Today, 81% of this energy is generated by burning fossil fuels that are depletable and release the greenhouse gas CO_2 into the air, leading to climate change and its various detrimental effects. Although the share and volume of renewable energy is quickly increasing, the absolute energy consumption from fossil fuels is not expected to decrease [2]. More energy that does not emit greenhouse gases is necessary. To continue to provide energy without depleting the planet's resources or changing the climate, there is a need for sustainable, safe, and clean energy sources.

1.1 The broader perspective of nuclear fusion

One of the future possibilities for such a sustainable and safe energy source is Nuclear Fusion. This process provides energy from the mass defect that occurs when two light particles fuse. The technology has promises abound, from safe, near CO_2-less energy production, to the ability to provide the current world energy demand for millions of years [3, 4].

The main technology that is envisaged to achieve energy production is called magnetically confined thermonuclear fusion. There are multiple types of devices that work with the same basic idea, but the leading device that has seen the most development is called the tokamak. The idea: having extremely hot ionised particles in the form of a plasma, confined by large magnetic fields in a vacuum chamber shaped like a torus. These particles then have so much energy that they can tunnel through the Coulomb potential, fuse and produce energy from the resulting mass defect.

A schematic of a tokamak is shown in Figure 1.1. The plasma inside the machine usually is fully ionised, which means that all the particles gyrate along the magnetic field lines. The toroidal magnetic field, is made to keep the particles within the torus by generating circular magnetic field lines, trapping the particles. Due to the $E \times B$ drift, which is dependent on the particle charge, the oppositely charged electrons and ions have the tendency to move away from each other, leading to a confinement loss. Therefore, a second magnetic field is necessary, the poloidal field that is generated by the toroidal plasma current (green arrows in figure). This field makes the field lines helical and keeps the electrons and ions well mixed and the plasma confined. This plasma current is typically generated by induction using a central solenoid; the inner poloidal field coils.

To achieve nuclear fusion, there can be different combinations of light particles to use as fusion fuel. Each of these particle combinations creates a different amount of energy, dependent on the increase in the binding energy of the resulting particles. For each combination of light particles fusing, there is an optimal temperature that trades off the collisionality to the tunnelling chance. The higher the temperature of the

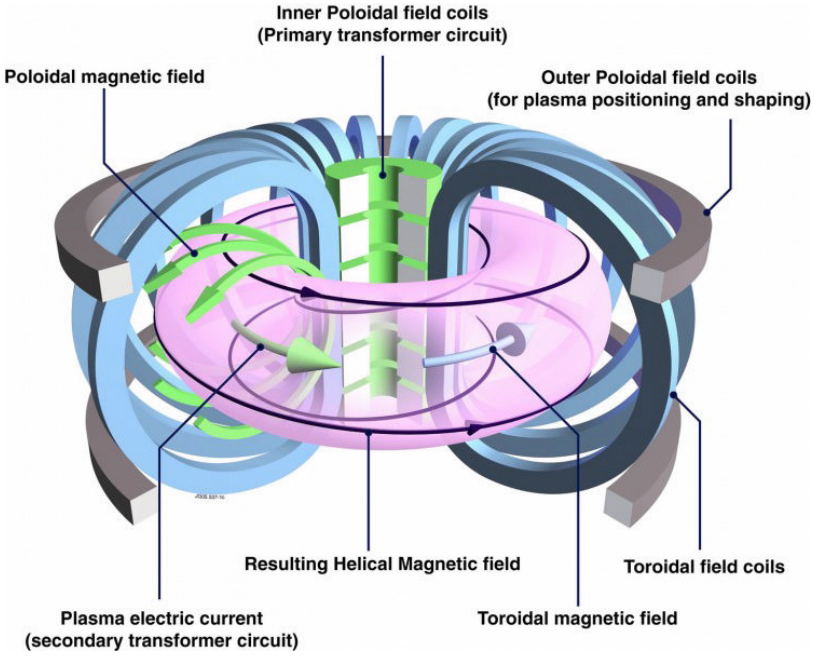

Figure 1.1: The schematic of a tokamak *image: EFDA*

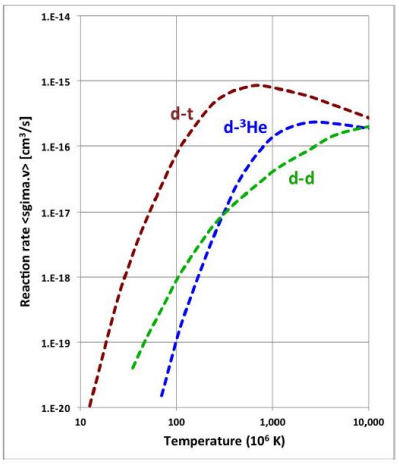

Figure 1.2: Reaction rates of relevant fusion reactions from [5]. The d-t reaction has the highest reaction rate, and at the lowest temperature. The energy released in each reaction is higher than d-d, and similar to d-3He.

particles, the easier they can overcome the Coulomb potential. However, this increased speed also means that the possibility of a collision decreases due to relativistic effects. Each combination of particles has a different fusing probability and released energy. The reaction rates for the main fusion options are given in Figure 1.2. Based on this plot, it is clear that deuterium (d) - tritium (t), having the highest reaction rate for all relevant temperatures, is the best choice of fuel. The reaction in formula is the following:

$$ {}^{2}_{1}\mathrm{D} + {}^{3}_{1}\mathrm{T} \rightarrow {}^{4}_{2}\mathrm{He}(+3.5\mathrm{MeV}) + {}^{1}_{0}\mathrm{n}(+14.1\mathrm{MeV}) \tag{1.1} $$

1.2 The energy balance

Unfortunately, as of yet, more energy is needed to operate fusion reactors than they generate. With the use of necessary auxiliary systems, from giant cryostats to keep the superconducting magnets cold and superconducting, to heating the plasma to fusion temperatures, more energy is spent than gained. The record for energy gained from fusion divided by the energy spent operating the system (Q_{fusion}) stands at 0.64 ± 0.04, and this value of Q_{fusion} was held on to for half a second in a shot at the Joint European Torus (JET) [6]. That means that in the record shot, less energy was produced than used. This value, 'Q_{fusion}', only illustrates the energy balance in the reactor itself. No Carnot (heat energy to electricity) conversion costs or secondary system energy costs have been accounted for in that 0.64 ± 0.04. The scheme in Figure 1.3 shows an overview of the systems directly involved in the energy balance of a fusion reactor and which of these are involved in the calculation of Q_{fusion}. The amount of power relative to the amount of energy spent will have to increase drastically for nuclear fusion to become a viable energy source.

Another way to look at the energy balance is to express the net generated electrical power in a formula, adapted from Pamela et al. [7]. Here, the power necessary for the heating and current drive is dependent on the achievable current drive efficiency and wall-plug efficiency of the chosen method:

$$ P_{\mathrm{e}} = P'_{\mathrm{e}} - P_{\mathrm{eHCD}} - P_{\mathrm{pump}} - P_{\mathrm{eBoP}} = P_{heat} \cdot \eta_{Carnot} - \frac{I_{\mathrm{CD}}}{\eta_{\mathrm{WP}}\eta_{\mathrm{CD}}} - P_{\mathrm{pump}} - P_{\mathrm{eBoP}}, \tag{1.2} $$

with P'_e the gross electrical power, P_{eHCD} the power necessary for the heating and current drive system, P_{pump} the power used by the coolant pumping system, P_{BoP} the power necessary for the rest of the operation i.e. cryostat and extraction. To design a tokamak that can produce net energy, two types of strategies

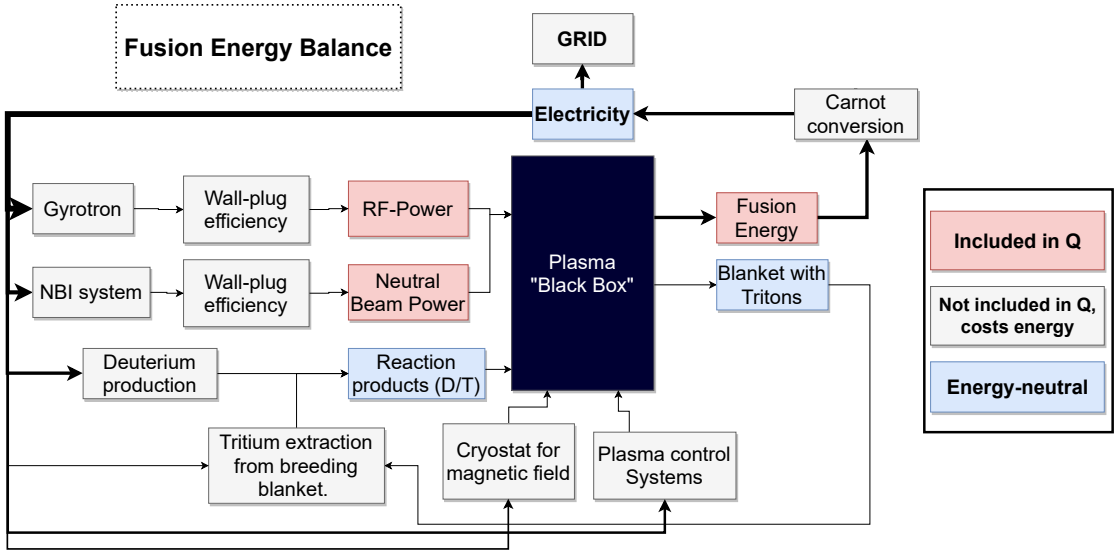

Figure 1.3: Schematic energy balance of a tokamak. The red blocks are currently included in the calculation of Q˙fusion, the white/grey blocks are not included but cost energy, the blue blocks are energy neutral.

can be employed: increasing the electricity production by increasing P_{heat} and/or η_{Carnot}, or minimising the circulated power given by P_{eHCD}, P_{pump} and P_{BoP}.

1.3 The Spherical Tokamak case

Spherical Tokamaks (ST's) are tokamaks that have a lower ratio of major radius/minor radius, or aspect ratio, that leads to a squashed shape, as in Figure 1.4. In tokamak terms, a tokamak is a spherical tokamak when they have a low aspect ratio ($A = R/a < 2$). This configuration leads to subtle but possibly important differences with respect to conventional tokamaks (CT's).

The interest in ST's is primarily based on three characteristics, 1) a high amount of plasma current that is run for free, the bootstrap current fraction f_{bs}, 2) the demonstration of operating at high relative plasma pressures β and 3) a relatively high magnetic field gradient inside the plasma that leads to a more robustness against magneto-hydrodynamic (MHD) instabilities [8].

The bootstrap current is a pressure-driven effect; it is self-generated by the plasma's density and pressure gradients in combination with the particles that are trapped in banana orbits by the magnetic field [9]. The bootstrap current generates a part of the necessary plasma current for free and scales approximately as follows:

$$f_{bs} \propto \epsilon^{1/2} \cdot \beta_p, \tag{1.3}$$

with ϵ the inverse aspect ratio (high in ST's) and β_p the relative poloidal plasma pressure (also favorable for ST's). The relative plasma pressure β signifies the upper limit of the plasma thermal pressure compared to the magnetic pressure. As the thermal pressure is the product of temperature and density, operating at the highest possible β for a given magnetic field is the most efficient. As the produced fusion power is proportional to T^2 and n^2 in the fusion reactor relevant regime, for a fixed magnetic field the produced fusion power scales approximately as:

$$P_{fusion} \propto n^2 \cdot T^2 \cdot V \propto \beta^2 \cdot V, \tag{1.4}$$

with V the volume of the reactor. This β is an important factor in the economics of a reactor; a large part of the extremely high costs of fusion reactors resides in the magnetic fields and the necessary steel

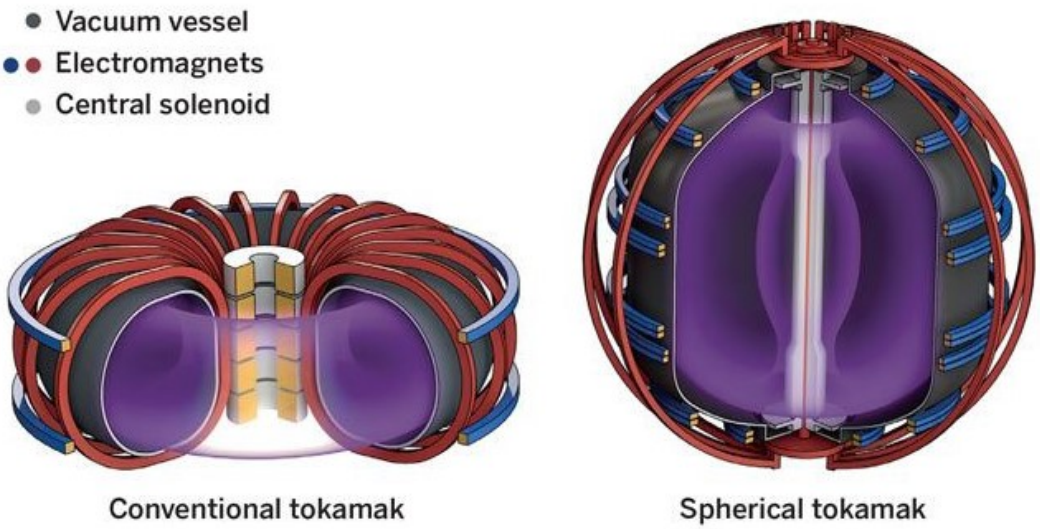

Figure 1.4: Both the conventional tokamak and the spherical tokamak operate on the same principles. The plasma is kept in place by a set of magnetic coils that provide a toroidal magnetic field, and there is a plasma current that supplies the poloidal field. The difference resides in the size of the central column and the relatively large amount of device one needs per unit volume for a conventional tokamak.

chamber to withstand the magnetic pressure. So achieving a high plasma pressure for the available magnetic pressure, is economically very good. The Spherical Tokamak (ST) typically has very high values for this parameter; the configuration holds the record for operating at high β [10]. Where the design of CT's is based on increasing V, leading to ever larger and more expensive reactors, the design of ST's is based on a very high β, leading to reactors that are relatively smaller and cheaper. The development of these smaller and cheaper reactors, aside from attempting to reach energy gain, could make for cheap(er) neutron sources and/or fusion research facilities [11, 12, 13] .

Unfortunately, the ST approach also has downsides. Most of these reside in the size of the central column. As is quickly visible, the free engineering space in the centre column is relatively small for ST's. This is a challenge; this space is used for neutron shielding, the central magnet, a central solenoid to inductively drive the plasma current and for the coolant to carry away the heat from the plasma-facing components. As the magnets and shielding are essential, this space will have to be taken from the central solenoid [14, 15]. As the flux swing that is achievable with a central solenoid is related to its surface, this means that no, or very little, inductive current can be driven to sustain the plasma current and thus poloidal magnetic field. This poloidal magnetic field is essential for the operation of a tokamak, and the lack of space for a central solenoid is difficult to overcome. In order to still be able to sustain a poloidal magnetic field to prevent charge separation, another method of current-drive has to be used. This leads to the necessity of non-inductive current drive methods.

1.4 Tokamak Energy's ST-F1 heating and current drive

Tokamak Energy Ltd. is a private company researching nuclear fusion and is based in the United Kingdom, Abingdon. Tokamak Energy 's route to fusion power is to use a high magnetic field with High Temperature Superconductors (HTS) as magnets. This approach is based on scaling studies [8, 16]. They have already built two ST's, the ST-25 (also with HTS magnets) and the ST-40 (with copper coils) and are in parallel developing a HTS-demo wherein they aim to demonstrate the use of HTS magnets in a toroidal configuration. Tokamak Energy's plan is to converge the HTS-demo with the ST design into the ST-F1 tokamak by 2025, to make the first tokamak to get to $Q_{\text{fusion}} > 1$, with the goal of achieving $Q_{\text{fusion}} = 3$. If this succeeds, it would mean a major breakthrough to making nuclear fusion an energy source.

The ST-F1 device is planned to operate with a toroidal magnetic field of 4 T and with a plasma current of 5 MA without a central solenoid. Thus, the total plasma current of 5 MA has to be supplied by non-inductive methods. The largest fraction of this current should be supplied by the bootstrap current, the bootstrap fraction is projected to be $f_{bs} = 0.7$, so this supplies 3.5 MA. The remaining 1.5 MA of the current has to be supplied by the non-inductive current drive systems. ST-F1's design goal is to reach a Q_{fusion} value of 3, and it is planned to operate completely without a central solenoid. These two goals are inextricably linked, as the Q_{fusion} value will depend heavily on the auxiliary power necessary to drive the plasma current. In the design of ST-F1, an auxiliary system current drive efficiency of $\eta = 0.15$ A/W is assumed. This would indicate a net power cost of $\frac{1.5\text{MA}}{0.15\text{A/W}} = 10$ MW. With the design currently aiming at a fusion power of $P_{fus} \sim 30MW$, the fusion power gain Q_{fusion} is highly dependent on the actual current drive efficiency. Furthermore, this power necessary to sustain the plasma current, is also necessary to heat the plasma. If the current drive efficiency turns out to be lower than 0.15 A/W, the necessary power to supply the current increases and the achievable Q_{fusion} decreases. Finding out what this efficiency might be is thus crucial in the design of this spherical tokamak.

Apart from being important for the general operation of a (spherical) tokamak, the total driven current and its radial profile also have implications for magnetohydrodynamic (MHD) stability. These instabilities can seriously degrade plasma performance and even cause disruptions to the discharge, causing the operation to stop or even damage the machine. MHD instabilities happen at specific values of the safety factor q: at rational surfaces of toroidal windings m over poloidal windings n of the magnetic field $q = \frac{m}{n}$. These are the surfaces where magnetic field lines reconnect with each other. The main instabilities happen at the flux surfaces where $q = 1$, $q = 3/2$ or $q = 2$. Due to their smaller size, Spherical Tokamaks generally operate at high values of q and are therefore more robust to MHD instabilities. However, in different operating scenarios and ST's, such as the Mega Ampere Spherical Tokamak (MAST), these instabilities are known to occur [17]. Being able to navigate the MHD instabilities is necessary for a future ST.

There are multiple options to drive the toroidal plasma current, the method that is currently envisaged to supply heating and a plasma current in ST-F1 is Electron Cyclotron Heating (ECH) and Current Drive (ECCD). In conventional tokamaks like ITER and DIII-D, the central solenoid is responsible for driving most of the current, and the EC system is chiefly used for current profile tailoring, MHD control, impurity control [18, 19]. Although this method is not known to have the highest current drive efficiency of the available options[20, **?**, **?**], the practical benefits are abound. The EC waves propagate in vacuum, can couple to the plasma efficiently and can propagate as a narrow beam, which means the launcher can be far away from the plasma [21]. Furthermore, its localised power and current deposition make it an interesting option for fusion devices as they can be used to shape the temperature and current profiles if necessary. The method works by inserting electromagnetic waves that are resonant in the plasma where the electrons gyrate at the electron cyclotron frequency, and can achieve heating and current drive at the resonant surfaces. There are two general mechanisms to drive the plasma current with cyclotron waves, the Ohkawa mechanism (OKCD) and the Fisch-Boozer mechanism (ECCD) [22, 23]. In CT's, the considered mechanism is ECCD, as it has the best efficiency for CT geometry and has been widely utilised experimentally. However, the OKCD mechanism relies on a high fraction of trapped particles and high β_e. These are both larger in ST's than in CT's. A recent study has shown that OKCD could potentially achieve higher current drive efficiencies in tokamak devices with low aspect ratios in specific scenarios [24].

A second consideration is the launcher location(s). For steady state current-drive in a fusion reactor, one can consider the Low Field Side (LFS) launch, or the Top Launch (TL) configurations. There could be large differences between the two configurations. A study on the DIII-D tokamak in San Diego shows that the TL configuration has twice as high off-axis current-drive efficiency than the conventional LFS launcher because it can interact with the higher-energy electrons [25]. This, however, does not necessarily extrapolate to central bulk current-drive or from machine to machine. Therefore, both Launchers are taken into account in this study of ECCD in ST-F1.
The options for the launch of EC-frequency waves are broad and consequential. The electromagnetic waves can be injected from the Low- or High Field Side (LFS - HFS) of the plasma, they can be launched at

different resonant frequencies, with different polarisation, modes, and different toroidal or poloidal angles. For conventional tokamaks, this efficiency has been investigated in multiple papers [26] [20] [27]. In ST's, especially large ST's with high magnetic fields like ST-F1, the body of literature is less extensive. In general, it is theorised that there are substantial differences in non-inductive current drive between ST's and CT's [28]. One of the reasons for that is the substantial toroidal magnetic field (B_t) gradient. This could for instance lead to second *and* fundamental resonance heating and current drive. Modelling the EC-efficiency for larger ST's is therefore very relevant.

1.5 This project

This project initially set out to obtain two goals: 1) chart the effect of ECCD on MHD stability and the safety factor profile, 2) find the ECCD current drive efficiency, power/current deposition location. During the project, the focus was shifted away from the first goal and towards the second. This was mostly related to the codes. Codes have become available that allow for study of Electron Cyclotron Heating and Current Drive, where the ASTRA model that was used for the safety factor calculations proved to come with difficulties. Exploring both options proved to not be possible within the time frame of this project, thus the choice was made to focus on the second goal.

The focus for this thesis is thus on the second goal, to find the optimal current drive efficiency and the attainable power/current deposition locations with electron cyclotron frequency waves. For the bulk current drive, mainly the efficiency in $\frac{\mathrm{A}}{\mathrm{W}}$ is of import. This part will be investigated by answering the research question:
What is the expected EC current drive efficiency in $\frac{\mathrm{A}}{\mathrm{W}}$ for ST-F1 in different discharge scenarios and for different launcher locations?.
For the power and current deposition location, how much of the power is absorbed is important, and where in the plasma the current can be driven. This will be researched by answering the following question:
How efficient is current-drive at different radial locations in the ST-F1 plasma?
For the design of ST-F1, it is important to know how the current-drive efficiency scales with the different discharge scenarios, thus with temperature and density.
How does the maximum current-drive efficiency scale with the central temperature and density in ST-F1?

1.6 Approach and outline

ST-F1 is in the design phase. This means that to answer the research questions, a resort has to be taken to different types of modelling. There is no a priori analytical way to find the maximum current-drive efficiency, power deposition location or absorption for different types of launchers. To find these characteristics, this research takes the following approach: to use existing codes that can calculate the values of interest, define the relevant parameters that can impact these, and perform parameter scans over them. The outcomes are analysed to answer the research questions. In order to do this, this research is structured as follows. First, an understanding of the physics of cyclotron wave propagation, absorption and the ensuing current drive have to be built up. In Chapter 2, the theory and physics behind waves in plasmas, EC wave propagation, heating and current drive are described. This chapter develops a broad understanding of the relevant phenomena, and references more in-depth literature where necessary. Then, the codes that are used have to be described. Chapter 3 describes the GENRAY ray-tracing code and the CQL3D Fokker-Planck code. In this chapter, the structure of the codes and the physics taken into account are focused on. This chapter is meant to give an understanding of the phenomena, to be able to appreciate the results and put them into context. These codes are well tested in different studies, and the codes are compared to each other in a test case, but the core infrastructure of the codes is only referenced, not in any way changed or evaluated. Chapter 4 presents the results, starting from the results of the different parameter scans, to zoom in on the localisation of the current-drive, the absorbed power, the current-drive mechanisms and different ways of calculating the current-drive. Chapter 5 discusses the results and their validity, and Chapter 6 concludes the thesis and puts it in context.

Chapter 2

Physics of cyclotron heating and current-drive

This chapter goes into the fundamental physics of ECCD. A broad overview of the existing literature with a relevance to this thesis is given. First, a background on the theory of waves in plasmas is given. Then, the current-drive mechanisms and different physical effects relating to current-drive are discussed.

Fusion plasmas are so hot that they are fully ionised. Understanding the response of the ionised plasma to electromagnetic waves is essential before one can think of doing anything like heating or driving a toroidal current in them. Calculating the response to an electromagnetic perturbation, such as a Radio Frequency (RF)-wave, is non-trivial. The response is highly dependent on the polarisation, frequency, wave injection angle and on the characteristics of the plasma medium itself: the magnetic field strength and its temperature and density. The wave phenomena such as absorption and reflection are quite important (one could think of the harm done to a machine, when injecting 10 MW of power to find that it is entirely reflected by the plasma and is now incident on one specific location of a wall). The theory on this subject is well developed, so we will benefit from the existing theory to navigate and understand the phenomena at hand. In this chapter, a general overview of the basic elements of plasma wave theory is given, starting from Maxwell's equations and the cold plasma magnetised dielectric tensor, to hint at hot plasma approximations and relativistic effects. This description is based largely on Stix [29] [30], Westerhof [9] and particularly Swanson [31, 32]. The discussion then progresses to also address the mechanisms of absorption and actually driving a current, large parts are found from Fisch [33, 22], Prater [21] and Ohkawa [23].

2.1 Waves in plasmas

Electromagnetic waves in charged plasmas are dominated by many different effects in different regimes. In this study, the focus will mainly be on the ability of waves to propagate in fusion plasmas and how they couple their energy to the plasma. For that, a general description is necessary. To study the physics of electromagnetic waves in plasmas, first, the most general case is observed, that of the magnetised cold plasma, where ions and electrons have no thermal motion of their own. The propagation of waves is governed by the dispersion relation, the relation between the wavenumber k and the wave frequency ω in a medium. The dispersion relation of waves in plasmas can be obtained by starting with Maxwell's equations:

$$\nabla \times \boldsymbol{E} = -\frac{\partial \boldsymbol{B}}{\partial t}, \tag{2.1}$$

$$\nabla \times \boldsymbol{B} = \mu_0 \boldsymbol{j} + \epsilon_0 \mu_0 \frac{\partial \boldsymbol{E}}{\partial t}, \tag{2.2}$$

with $\boldsymbol{j}$ the current density given by $\boldsymbol{j} = \boldsymbol{\sigma} \cdot \boldsymbol{E}$, $\boldsymbol{E}$ and $\boldsymbol{B}$ the electric and magnetic fields respectively, $\boldsymbol{\sigma}$ the conductivity tensor, ϵ_0 the permittivity of a vacuum and μ_0 the permeability of a vacuum. Eliminating

$\boldsymbol{B}$ by taking the time derivative of equation 2.2 and substituting $\frac{\partial B}{\partial t}$ from equation 2.1, and substituting $\boldsymbol{j} = \boldsymbol{\sigma} \cdot \boldsymbol{E}$ gives a version of the Helmholtz equation:

$$\nabla \times (\nabla \times \boldsymbol{E}) + \frac{\partial}{\partial t}\left(\mu_0 \boldsymbol{\sigma} \cdot \boldsymbol{E} + \epsilon_0 \mu_0 \frac{\partial}{\partial t}\boldsymbol{E}\right) = 0. \tag{2.3}$$

Then, assuming the electric field behaves like a wave with a slow-changing amplitude, i.e. $\boldsymbol{E} \sim E \cdot e^{i(\boldsymbol{k}\cdot\boldsymbol{r}-\omega t)}$ so that $\nabla \times \boldsymbol{E} = \boldsymbol{k}$ and $\frac{\partial E}{\partial t} = -\omega$, introducing the dielectric tensor as $\boldsymbol{\epsilon} = \left(\mathbf{1} + \frac{i}{\omega\epsilon_0}\boldsymbol{\sigma}\right)$, this combines into the general dispersion relation for waves in plasmas as:

$$\det \left| \mathbf{kk} - \mathrm{k}^2 \cdot \mathbf{1} + \frac{\omega^2}{c^2} \cdot \boldsymbol{\epsilon} \right| = 0, \tag{2.4}$$

where the definition $c^2 = \frac{1}{\mu_0 \epsilon_0}$ is used. This expression indicates that the behaviour of waves in plasmas is determined by the dielectric tensor $\boldsymbol{\epsilon}$, and thus the conductivity tensor σ. There are a couple of methods to do this, but the simplest and most generally used is the cold plasma dispersion approximation.

2.2 Cold plasma dispersion

The cold plasma description of the dispersion captures most of the physics that we are interested in the EC regime. The individual thermal movement of the particles is ignored, which leads to a well-defined problem. This description will turn out to be correct in most of the plasma, except when nearing the resonances. The basis for the cold plasma description is to apply mass and momentum conservation to every constituent of the plasma (i.e. ions and electrons):

$$m_s \left(\frac{\partial \mathbf{v_s}}{\partial t} + (\mathbf{v_s} \cdot \nabla)\,\mathbf{v_s}\right) = q_\mathbf{s}\left(\mathbf{E} + \mathbf{v_s} \times \mathbf{B}\right), \tag{2.5}$$

where the subscript s stands the species, m for the mass, v for the velocity and q for the species' electric charge ($\pm e$). As this is a cold plasma, significant simplifications arise from linearising the momentum equation as small deviations around a steady value. The first order linearisations are the following:

$$\begin{aligned} n &= n_0 + n_1 \\ \mathbf{v} &= \mathbf{v}_1 \\ \mathbf{E} &= \mathbf{E}_1 \\ \mathbf{B} &= \mathbf{B}_0 + \mathbf{B}_1, \end{aligned} \tag{2.6}$$

with the species subscript dropped for clarity. Static velocities and electric field are dropped, which makes sense as this is a cold plasma and thus the electric field is shielded and the velocity very low. This leads to the following linear formulation of the momentum conservation:

$$m_s \frac{\partial \mathbf{v}_{s\mathbf{1}}}{\partial t} = q_s\left(\mathbf{E_1} + \mathbf{v}_{s\mathbf{1}} \times \mathbf{B_0}\right). \tag{2.7}$$

To avoid most cross-terms, now the z-axis is aligned with the steady magnetic field $\boldsymbol{B_0}$. Also, assuming all the perturbations can be described as waves, so go as $\sim e^{i(\boldsymbol{k}\cdot\boldsymbol{r}-\omega t)}$. The relationship between $\boldsymbol{v}_1$ and $\boldsymbol{E}_1$ can be shown to be:

$$\begin{pmatrix} -\mathrm{i}\omega & -\Omega_{cs} & 0 \\ +\Omega_{cs} & -\mathrm{i}\omega & 0 \\ 0 & 0 & -\mathrm{i}\omega \end{pmatrix} \boldsymbol{v}_{s1} = \frac{q_s}{m_s}\boldsymbol{E}_1, \tag{2.8}$$

here, $\Omega_{cs} = q_s B/m_s$ is the general cyclotron frequency. In a relativistic treatment, the Lorentz factor $\gamma_s = (1 - (\frac{v_s^2}{c^2}))^{-1/2}$ should be used to account for relativistic mass effects. Throughout this thesis, this is not always necessary , if it is necessary, the Lorentz factor is written outside of the cyclotron frequency. This matrix can be solved with matrix inversion for ions and electrons. Following the reasoning of [30], the

conductivity tensor that was sought results from the summation of the solutions of the inverted matrices and turns out to be:

$$\sigma = \epsilon_0 \sum_s \begin{pmatrix} \mathrm{i}\dfrac{\omega\omega_{ps}^2}{\omega^2-\Omega_{cs}^2} & -\dfrac{\Omega_{cs}\omega_{ps}^2}{\omega^2-\Omega_{cs}^2} & 0 \\ +\dfrac{\Omega_{cs}\omega_{ps}^2}{\omega^2-\Omega_{cs}^2} & \mathrm{i}\dfrac{\omega\omega_{ps}^2}{\omega^2-\Omega_{cs}^2} & 0 \\ 0 & 0 & \mathrm{i}\dfrac{\omega_{ps}^2}{\omega} \end{pmatrix}, \tag{2.9}$$

where $\omega_{ps} = \sqrt{n_s q_s^2 \epsilon_0 m_s}$ is the plasma frequency of the particle species s with n_s the number density. To shorten, the conductivity tensor is substituted in the dielectric tensor, with the following form:

$$\varepsilon = \begin{pmatrix} S & -\mathrm{i}D & 0 \\ \mathrm{i}D & S & 0 \\ 0 & 0 & P \end{pmatrix}. \tag{2.10}$$

A physical interpretation hereof, is that S and D are the sum and difference of the response to right and left handed polarised waves, and P is the parallel plasma response to the electric field. Written out this gives the following components:

$$\begin{aligned} &S \equiv \frac{1}{2}(R+L), \quad D \equiv \frac{1}{2}(R-L), \\ &R \equiv 1 - \textstyle\sum_s \dfrac{\omega_{ps}^2}{\omega\left(\omega+\Omega_{cs}\right)}, \\ &L \equiv 1 - \textstyle\sum_s \dfrac{\omega_{ps}^2}{\omega\left(\omega-\Omega_{cs}\right)}, \\ &P \equiv 1 - \textstyle\sum_s \dfrac{\omega_{ps}^2}{\omega^2}, \end{aligned} \tag{2.11}$$

R, L, and P can be interpreted as the response of the plasma to a waved polarised righthandedly, lefthandedly or parallel to the electric field. Since the sign of Ω_{cs} differs from specie to specie due to their charge, the wave polarization matters for which species is affected by the wave. Specifically, the response to the righthanded polarized wave becomes infinite (absorption) at the electron cyclotron frequency $\omega = \omega_{ce}$ and for the lefthandedly polarized wave at the ion cyclotronω_{ci}. As P is the plasma response to a wave polarized parallel to the magnetic field, and the movement of electrons and ions is thus unimpeded by the magnetic field, so this reaction of the plasma to plasma waves is the same as in an unmagnetized plasma. Substituting the identity of the refractive index; $N = \dfrac{ck}{\omega}$, implementing θ as the angle between k and B and then substituting the obtained dielectric tensor into the dispersion relation, a dispersion tensor Λ is obtained:

$$\mathbf{\Lambda} = \begin{pmatrix} S - N^2\cos^2\theta & -\mathrm{i}D & N^2\cos\theta\sin\theta \\ \mathrm{i}D & S - N^2 & 0 \\ N^2\cos\theta\sin\theta & 0 & P - N^2\sin^2\theta \end{pmatrix}. \tag{2.12}$$

In order to satisfy the dispersion relation, the determinant of this tensor has to be zero. One of the solutions that can be found is a biquadratic equation for the refractive index. The cold plasma dispersion relation now reads:

$$AN^4 - BN^2 + C = 0, \tag{2.13}$$

with the separate coefficients:

$$\begin{aligned} A &= S\sin^2\theta + P\cos^2\theta, \\ B &= RL\sin^2\theta + PS\left(1+\cos^2\theta\right), \\ C &= PRL, \end{aligned} \tag{2.14}$$

and the mathematical identity:

$$S^2 - D^2 = RL. \tag{2.15}$$

One can now solve the dispersion relation for N^2 in these terms to be:

$$N^2 = \frac{B \pm \sqrt{B^2 - 4AC}}{2A}. \tag{2.16}$$

For propagation parallel $\theta = 0$ and perpendicular $\theta = \pi/2$ to the magnetic field, the solutions for this become: $P = 0, \quad N^2 = R, \quad N^2 = L$ $(\theta = 0)$ and $N^2 = RL/S, \quad N^2 = P$ $(\theta = \pi/2)$. As the interest here will be in the electron cyclotron frequency range, and since $\frac{m_i}{m_e} = \frac{\Omega_e}{\Omega_i} \sim 1000$, one can safely assume the ion contributions are relatively small compared to the electron contributions in the high-frequency range. Applying these, one obtains the 'electron', or Appleton-Hartree dispersion relation:

$$N^2 = 1 - \frac{X[1-X]}{1 - X - \frac{1}{2}Y^2\sin^2\theta \pm \sqrt{\left(\frac{1}{2}Y^2\sin^2\theta\right)^2 + [1-X]^2Y^2\cos^2\theta}}, \tag{2.17}$$

with $X = \left(\omega_{pe}/\omega\right)^2$ and $Y = |\Omega_{ce}|/\omega$.

When considering wave propagation in an inhomogeneous magnetised plasma, such as exist in a (spherical) tokamak, the inhomogeneity is mainly perpendicular to the magnetic field. In these cases the parallel refractive index $N_\parallel$ is conserved along the propagating wave. Here, $N_\parallel = (\boldsymbol{N}\cdot\boldsymbol{B})/B$ and $\boldsymbol{N}_\perp = \left(\boldsymbol{N} - \boldsymbol{N}_\parallel\right)$. Then, $N^2 = N_\perp^2 + N_\parallel^2$ and the biquadratic equation can be re-written for $N_\perp^2$:

$$A'N_\perp^4 - B'N_\perp^2 + C' = 0, \tag{2.18}$$

with the coefficients:

$$\begin{aligned} A' &= S, \\ B' &= (S+P)\left(S - N_\parallel^2\right) - D^2, \\ C' &= P\left(\left(S - N_\parallel^2\right)^2 - D^2\right). \end{aligned} \tag{2.19}$$

One can now solve for $N_\perp^2$ as $N_\perp^2(B, N_\parallel, n_e, \omega)$ with n_e the local electron density. Of these, n_e, ω and B are all functions of $\boldsymbol{r}$. For perpendicular propagation, in which for the purpose of this thesis there is the most interest (electromagnetic waves will have to travel at least partly perpendicularly to the magnetic field to penetrate into the plasma at all), two wave modes can be identified: waves with a polarisation parallel to the magnetic field (O-mode), or waves with a polarisation perpendicular to the magnetic field (X-mode). Their respective refractive indices are characterised in the following way [34]:

$$O - \text{Mode} \quad N_\perp^2 = 1 - \frac{\omega_{pe}^2}{\omega^2}, \tag{2.20}$$

$$X - \text{ Mode} \quad N_\perp^2 = 1 - \frac{\omega_{pe}^2\left(\omega^2 - \omega_{pe}^2\right)}{\omega^2\left(\omega^2 - \omega_{pe}^2 - \omega_{ce}^2\right)}. \tag{2.21}$$

These are the two modes that are of interest for heating and current drive in a tokamak. The 'O - Mode', or ordinary mode, has the same propagation dispersion relation as an unmagnetized plasma except near cyclotron resonances, as will become clear. This makes sense when one considers that the polarisation is parallel to the magnetic field, and thus the particles do not experience any effect of the magnetic field.

2.3 Resonances and cut-offs

The regions of the plasma response that we are interested in are the resonances and cut-offs. The cut-offs are to be avoided at all cost, as they create the unwanted phenomenon of reflection. At plasma resonances, which are only there for the X-mode polarisation, interesting physics can occur. For this study, the focus is on avoiding the cut-offs, as the plasma resonances will prove hard to reach. Nonetheless, attempting to reach the upper hybrid resonance (UHR) to achieve mode conversion, is a very active field of research for

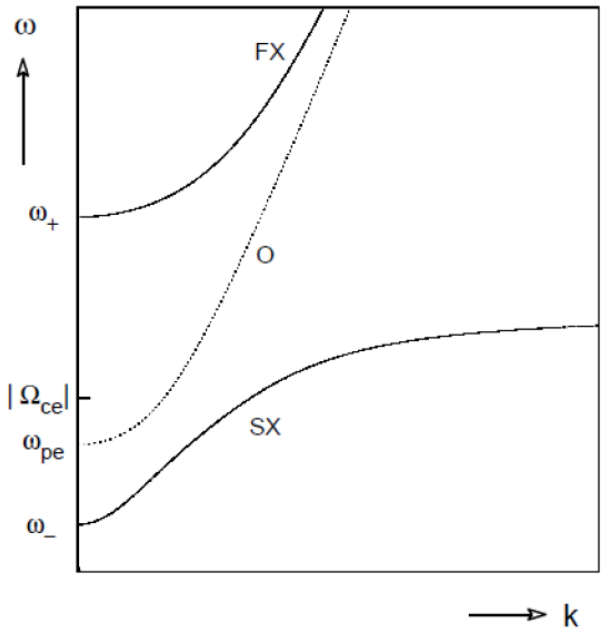

Figure 2.1: Dispersion relation in the high frequency domain, here the lines represent the cutoffs, FX represents the fast X-mode, SX the slow X-mode and O the O-mode cutoff.

spherical tokamaks with overdense operation, where the plasma frequency is several times the cyclotron frequency [35]. In ST-F1, this is not a problem, as the plasma frequency is of the order of the fundamental cyclotron frequency. At plasma resonances, i.e. $N \to \infty$ the energy and momentum of the wave is imparted on the plasma. At cut-offs, i.e. $N = 0$ the wave direction is reversed, so the wave is reflected. For the O-mode, $N = 0$ if $\omega = \omega_{pe}$, and for X-mode there are two cut-offs, the upper $(+)$ and the lower $(-)$ cutoffs, represented by the following frequencies:

$$\omega_{\pm} = \pm\frac{1}{2}\left|\omega_{ce}\right| + \sqrt{\left(\frac{1}{2}\omega_{ce}\right)^2 + \omega_{pe}^2/\left(1 - N_{\parallel}^2\right)}. \tag{2.22}$$

The X-mode also introduces two hybrid resonances, the upper hybrid resonance (UHR) and the lower hybrid resonance LHR:

$$\omega_{uh} = \sqrt{\omega_{ce}^2 + \omega_{pe}^2}. \tag{2.23}$$

At this hybrid resonance, the wave-power is absorbed by the plasma, and a multitude of things can happen. At this resonance for instance, mode conversion can occur. There is a region between this upper hybrid resonance and the upper cutoff, that is called the evanescent region, where the X-mode wave is evanescent. In this region, the X-mode waves cannot propagate. This evanescent region splits the so-called 'slow' X-mode, and the 'fast' X -mode. The dispersion relation for the high frequency limit can be visualised as in Figure 2.1.

2.4 Cyclotron resonances

The cyclotron resonances are the relevant locations where the wave frequency matches the cyclotron frequency, here, energy is coupled to electrons. The cyclotron resonances are a consequence of the motion of electrons gyrating around magnetic field lines at the cyclotron frequency, which is dictated by the strength of the magnetic field. Absorption by individual electrons occurs in the regions where the frequency of the electromagnetic wave satisfies the resonance condition:

$$\omega - k_{\parallel} v_{\parallel} - n\omega_{\mathrm{ce}}/\gamma = 0. \tag{2.24}$$

Here, ω is the wave frequency, γ is the relativistic mass factor, $k_\parallel v_\parallel$ is the Doppler shift, $\omega_{\rm ce} = 2\pi\Omega_{\rm ce}$ and n is an integer that specifies the cyclotron harmonic. The definition of cyclotron heating and current drive is when $n \geq 1$. For current drive with this mechanism, a Doppler shift is necessary, as this shift will turn out to be the selection mechanism by which right-moving electrons can be differentiated from left-moving electrons. When $k_\parallel = 0$, there is perpendicular injection so no directionality selection and no current-drive. It is important to note that the Doppler shift term only comes into play in the case of oblique propagation, so when $k_\parallel \neq 0$. For injection in the direction of increasing magnetic field, the electrons with positive $k_\parallel v_\parallel$ are absorbed first, leading to the selection of directional electrons.

2.5 Propagation: Ray tracing

A widely used method to determine the propagation of cyclotron waves in plasmas, is ray tracing. This is also the method that will be used in the GENRAY code, then generalised to tokamak geometry. This method relies on the Wentzel, Kramers, Brillouin (WKB) approach, to follow the group velocity of a wave in, and therefore its energy density [31]. This theory holds up when the dispersion relation and electric and magnetic field vary on length scales larger than the thermal motion of electrons, which is the case in most fusion plasmas except near resonances, which is discussed later. In GENRAY, ray tracing is based on the geometrical optics approximation as layed out by Friedland and Bernstein [36]. In this method, the wave vector and number are advanced through derivatives of the dispersion relation, thereby finding the propagation of the wave. A derivation is given in [31], [30] or [37], and the set of three Ordinary Differential Equations (ODE) ray equations that come out of this are the following:

$$\frac{d\boldsymbol{r}}{d\tau} = \frac{\partial D}{\partial \boldsymbol{k}}, \tag{2.25}$$

$$\frac{d\boldsymbol{k}}{d\tau} = -\frac{\partial D}{\partial \boldsymbol{r}}, \tag{2.26}$$

$$\frac{d\omega}{d\tau} = \frac{\partial D}{\partial t}, \tag{2.27}$$

where τ is the trajectory to be solved for and $D(\mathbf{k}, \omega, \mathbf{r}, t) = det|\boldsymbol{\epsilon}| = 0$ the dispersion relation. For these equations, the dispersion relation acts as a Hamiltonian. The geometric optics approximation uses a hermitian and non-hermitian plasma dielectric tensor, i.e. $\epsilon = \epsilon_H + \epsilon_A$. This theory uses the planar wave approximation and the non-hermitian part of the dielectric tensor relevant for hot plasmas to come to a dispersion relation based on the complex roots of the frequency $\Omega = \omega + i\nu$. Here, the real part ω is used to generate the waves, and the imaginary part $i\nu$ is used to find the amplitude of the electric field E that is relevant for the transport of momentum and energy. In ray-tracing codes, these equations are simplified to derivations based on the product of the dispersion relation and its hermitian conjugate DD^H.

Ray-tracing can model a Gaussian beam only by a spatial arrangement of multiple rays. This maintains some of the physics that one would expect from a Gaussian beam. Spatial effects, such as the deviation from a Gaussian deposition profile for a ray with an incoming angle with respect to the resonance are maintained. However, there is no interaction between the waves, so phenomena such as interference or diffraction are not included. Furthermore, the absorption of one ray of the beam has no effect on the propagation of the other beams in the bundle.

2.6 Dispersion relation corrections

Until now, the assumption has been that the plasma is cold, when considering the plasma dispersion relation for ray-tracing or otherwise. Most of the understanding of the behaviour of waves in plasmas can be gathered from the previous paragraphs. However, the addition of hot plasma effects is necessary for a self-consistent treatment of waves in fusion plasmas [21]. The addition of an anti-Hermitian part, finite temperature terms dependent on T_e and the density n_e are necessary because of the hot plasma dielectric tensor. Especially when the ray travels parallel to a resonance (i.e. in top launch), the ray-tracing condition that $\epsilon_H > \epsilon_{aH}$ can be violated [21]. For fusion purposes, relativistic effects must always be included

in the calculation of current drive and power absorption.

There are multiple ways one could correct for the hot plasma effects, here just the dispersion relation corrections and methods are given that also exist in the GENRAY code. There are different implementations of these dispersion relations for calculation purposes that take into account different physical effects.
The Mazzucato relativistic dielectric tensor [38] takes into account corrections for the finite larmor radius (FLR) effects that arise in hot and dense plasmas. The FLR effects can an effect on $N_\perp$ particularly for X-mode waves travelling parallel to the resonance in plasmas where $\omega_p \sim \omega_{ce}$.

Westerhof and Tokman implemented a solution to the problem that the anti-Hermitian part of the dielectric tensor becomes non-negligible for waves propagating near the cyclotron resonances [39]. This has an impact on the calculation of the energy flux and hence the propagation and absorption behaviour. Even though the requirements for the geometric optics (or WKB) approximation [36] are satisfied for waves near these resonances, the anti-Hermitian part becomes so large that the direction of the energy flux was wrong. This was resolved by adding a term to the wave energy flux equation that takes into account the effect of the change in the wave polarisation of the anti-Hermitian part of the dielectric tensor [40].

2.7 Absorption

To know the rate and location of absorption, is necessary for ECCD and heating. The absorption itself is necessarily a hot-plasma effect, as it makes use of the finite Larmor radius of the electrons. If a wave satisfies the resonance condition, this does not mean that it is entirely absorbed. For that, the optical thickness has to be considered:

$$\tau = \int_0^l \alpha \, \mathrm{ds}, \tag{2.28}$$

with τ the optical thickness, s the space coordinate along the ray path of length l, and α the absorption coefficient. Along this path, $P_{abs} = P_0 \cdot e^{-\tau}$ is then the absorbed power. The absorption coefficient varies in the plasma and is dependent on density, polarisation, frequency and the specific harmonic. The absorption coefficient is important for the localisation, as well as for the total absorbed power fraction of the wave. Bornatici finds the absorption at the cyclotron resonances to be the following [41, 42].

For O-mode:

$$\tau_n^{(0)} = \frac{\pi n^{2(n-1)}}{2^n (n-1)!} \left[1 - \left(\frac{\omega_p}{n\omega_{ce}}\right)^2\right]^{n-1/2} \left(\frac{\omega_p}{\omega_{ce}}\right)^2 \left(\frac{T}{mc^2}\right)^n \frac{\omega_{ce} R}{c}, \tag{2.29}$$

and or X-mode ($n \geq 2$):

$$\tau_n^{(X)} = \frac{\pi n^{2(n-1)}}{2^n (n-1)!} \left(\frac{\omega_p}{\omega_{ce}}\right)^2 \left(\frac{T}{mc^2}\right)^{n-1} \mu_n^{(X)} \left(\theta = \frac{\pi}{2}\right) \frac{\omega_{ce} R}{c}, \tag{2.30}$$

and for fundamental ($n = 1$) X-mode:

$$\tau_1^{(X)} = \frac{5\pi}{\sqrt{2}} \left(\frac{\omega_{ce}}{\omega_p}\right)^2 \left(\frac{T}{mc^2}\right)^2 \frac{\omega_{ce} R}{c}, \tag{2.31}$$

for $2\frac{T}{mc^2} < \left(\frac{\omega_p}{\omega_{ce}}\right)^2 < 1$. Here, $\mu_n^{(X)}$ in the limit of quasi perpendicular propagation is $\mu_n^{(X)}(\theta) = \left[N_\perp^{(X)}\right]^{2n-3} \left[1 + \frac{(\omega_p/\omega_c)^2}{n\left[n^2 - 1 - (\omega_p/\omega_c)^2\right]}\right]^2$, θ is the angle between the magnetic field direction and the wave vector and R is the major radius at the point of absorption. The absorption scales with $\frac{T}{mc^2}$ for each harmonic, so it becomes weaker and weaker for higher n. Furthermore, X-mode in general has a higher absorption rate than O-mode. Especially first harmonic O-mode and second harmonic X-mode are interesting for heating and current drive purposes. The first harmonic X-mode has a negative scaling with density, while the other modes have positive scalings.

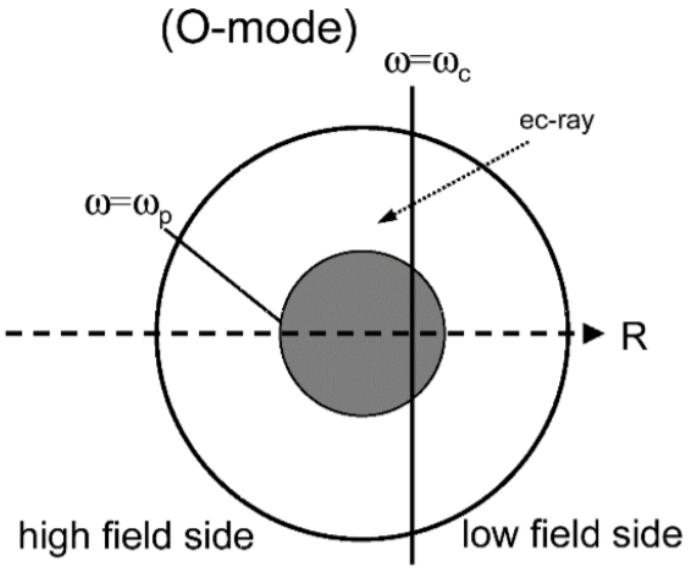

Figure 2.2: Accessibility for O-mode EC-launch. The fundamental frequency where the wave is absorbed is $\omega = \omega_c$, and the plasma frequency where $\omega = \omega_p$ is where the O-mode is cut-off. Figure from [21]

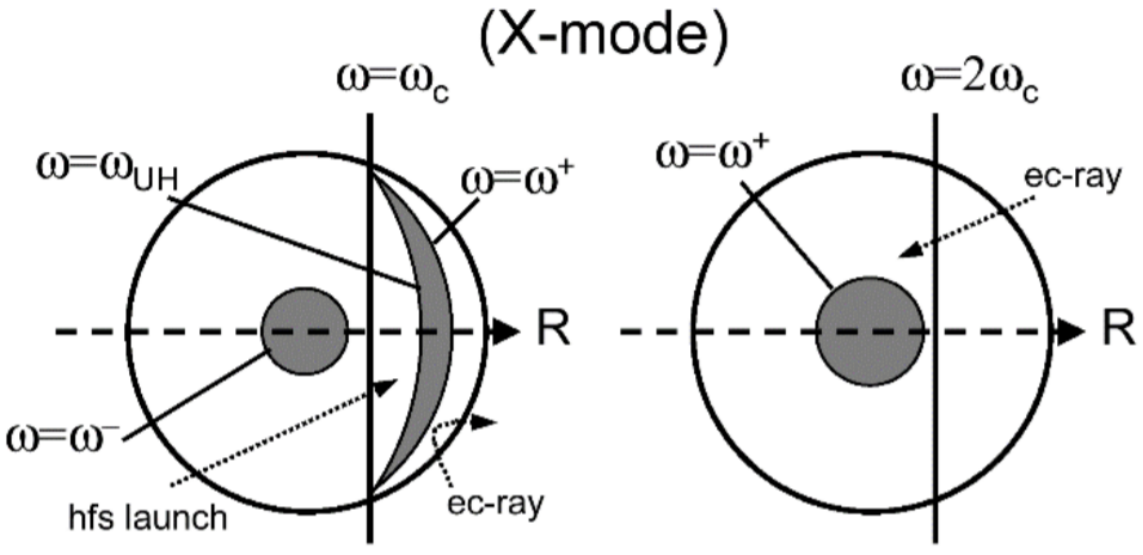

Figure 2.3: First ($\omega = \omega_c$) and second ($\omega = 2\omega_c$) harmonic X-mode accessibility. From [21]

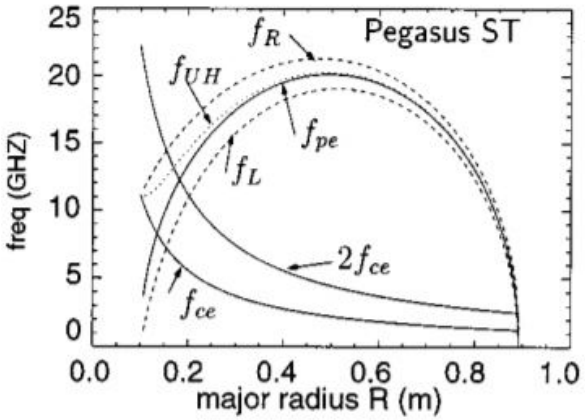

Figure 2.4: Accessibility in the Pegasus spherical tokamak from [43].

2.8 Accessibility

To efficiently heat or drive a current in a plasma, it is important to stave off cut-offs, and have an a priori sens of which frequencies might be able to propagate into the machine. To ascertain whether this is the case, we consider the accessibility of a tokamak. The accessibility is governed by the electron density n_e and the magnetic field B. Power absorption and current drive happen at the cyclotron resonances, but these have to be reached. O-mode waves are reflected at the plasma frequency, and X-mode waves at the fast or slow X-mode cut-offs. The cut-offs must be avoided and the resonances reached at the locations where one would want to heat the plasma, drive a current in it or both. It is then helpful to show these resonances and cut-offs in general tokamak geometry. The case is relatively simple for O-mode, as shown in Figure 2.2, where only the plasma frequency is an issue. For X-mode the case is a bit more complicated, as shown in 2.3.

For most spherical tokamaks, the magnetic field is relatively small due in part to the little space there is in the centre column. The ratio of the plasma frequency to the electron cyclotron frequency is of the order of $\omega_{pe}/\Omega_{ce} > 5$ in most operating scenarios, making the plasma 'overdense' [43, 44]. This high ratio means that the accessibility for first or second fundamental electron cyclotron resonance heating or current drive is normally a problem, as shown in Figure 2.4. Therefore, the literature on current drive with cyclotron frequency waves in ST's generally focuses on the Electron Bernstein Wave (EBW) mode conversion mechanism.

The high toroidal magnetic fields $B_t \approx 4$ that are envisaged for the ST-F1 combined with a number density of $n_e = 13.7 \cdot 10^{19} m^{-3}$ give a ratio of $\frac{\omega_{pe}}{\Omega_{ce}} = \frac{110\text{GHz}}{112GHz} \approx 0.99$, so conventional ECCD at the fundamental or second harmonic resonances can also be a good option for this type of high-field ST. For ST-F1, We now have expressions for the different cut-offs and resonances as a function of magnetic field, density, temperature and velocity. These can be plotted as a function of minor radius. For the ST-F1, three scenarios are taken into account with design-point density, high density and low density as will later be introduced in Figure 4.1. For the ST-F1 tokamak this leads to the different accessibility plots shown in Figures 2.5 and 2.8.

The accessibility figures for ST-F1 illustrate different possibilities depending on the density. In the design point and low density scenario, the fundamental O-mode resonance and second harmonic X-mode resonance are accessible. In the high density scenario, only the second harmonic O-mode, and parts of the second harmonic X-mode resonance are accessible. Note that these values are the values as they are at the centre of the machine, and that it is possible to launch waves from the top of the machine, a minor radius of 160 cm for instance, into the plasma without it being directly reflected, as the density is still low in the edge

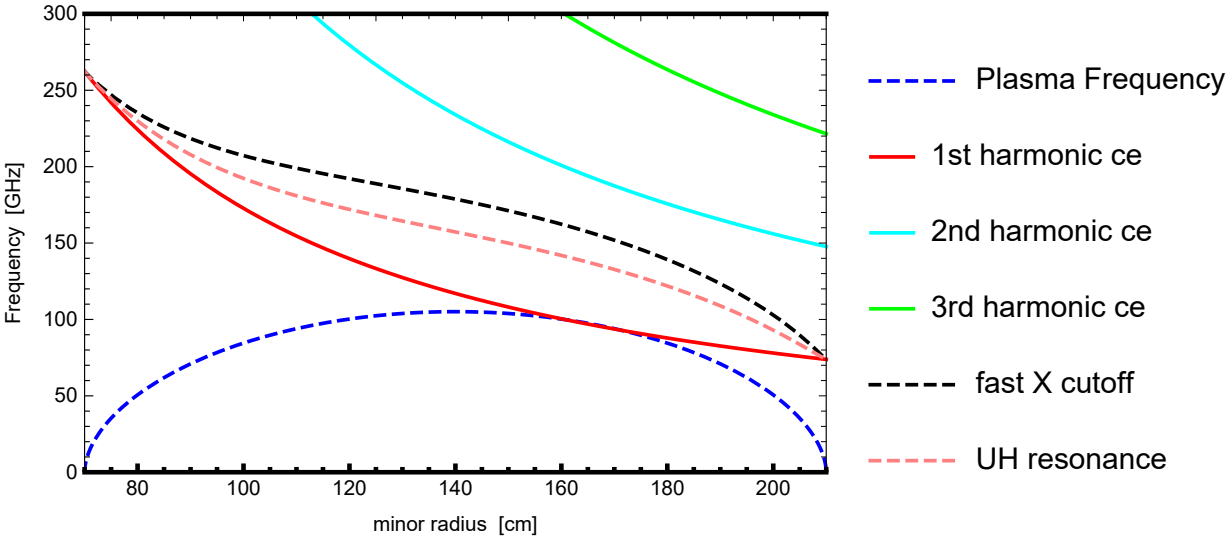

Figure 2.5: Accessibility for the ST-F1 design point.

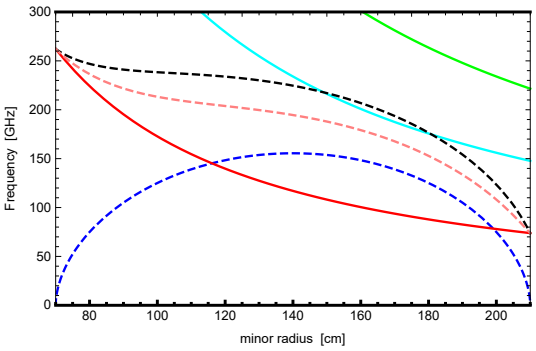

Figure 2.6: High density scenario accessibility.

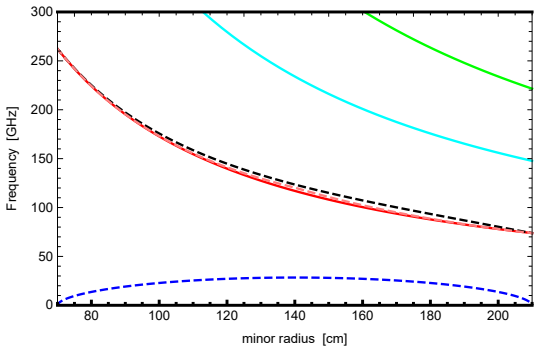

Figure 2.7: Low density scenario accessibility

Figure 2.8: Accessibility for the high and low density scenarios.

of the machine. This can also be inferred from Figure 2.3.

2.9 Current drive

Now that there is a theoretical model for the propagation and absorption of cyclotron waves, the question is how to use this for the purpose of driving a toroidal plasma current. One would assume that this is done by imparting parallel (to the magnetic field lines) momentum. And in fact, early current drive research focused on depositing toroidal momentum to electrons, and specifically slow electrons, which were believed to be more efficiently push-able. This has to do with the fact that, generally, increasing the momentum of a slow particle takes less energy than increasing the momentum of a fast particle by a factor $\sim v$. However, the current, which then consists of moving electrons, is cancelled by collisions. And the collision rate goes as $\nu \sim 1/v^3$. The relativistic scattering rates of electron-electron collisions are given by the following function [45]:

$$\nu_{\mathrm{ee}}(u) = \nu_{\mathrm{e0}}\gamma \left(\frac{u_{\mathrm{e}}}{u}\right)^3 . \tag{2.32}$$

Combining these factors, it is actually the fast electrons that carry current in hot fusion plasmas. Further problems arise for low-temperature electron heating, in that the low-energy particles are typically the particles that are trapped in the magnetic trap that comes with the gradient in the magnetic field. This trapping means that they reverse toroidal direction while moving on their flux surface and that they, thus, cannot carry current. Later, the necessity of imparting parallel momentum was found to be unnecessary for current drive in the Fisch-Boozer mechanism [22]. The trapping effect was also turned into a source of current-drive by selectively trapping electrons. Trapping particles in a directional way also incites a current in the Ohkwawa current drive mechanism [23]. For both mechanisms, the theoretical ECCD efficiency in A/W is written as [46]:

$$\frac{I_{\mathrm{ec}}}{P_{\mathrm{ec}}} = \frac{\epsilon_0^2}{e^3}\left(\frac{kT_e}{\ln\Lambda R n_e}\right)\zeta\left(Z, \epsilon, \theta_{\mathrm{pol}}, w\right), \tag{2.33}$$

where $\ln\Lambda$ is the Coulomb logarithm, and ζ is a form factor that is dependent on the polarisaton, velocity distribution, the dielectric and the charged particle mass distribution.
In wave-current drive, as might have been gathered from one of the previous paragraphs, there are two competing effects: collisions moving the electrons back to a Maxwellian distribution, and the RF-waves attempting to establish directional particle-movement to sustain a current. To find an evolution of the distribution of the phase space plasma particles, described by f, one can write a Fokker-Planck equation for this system. This equation describes the evolution of the plasma particle distribution function as a function of the different forces acting on the system, in this case same-particle collisions, inter-particle collisions and the wave-induced flux. The Fokker-Planck equation is also what the CQL3D code is built to solve. Calculating the different moments of the distribution function f from this equation allows you to find the velocity and distribution of the particles, hence also the driven current:

$$\frac{df_e}{dt} = \frac{\partial f_e}{\partial t}\Big|_{collisions} + \frac{\partial f_e}{\partial t}\Big|_{ECH} + \frac{\partial f_e}{\partial t}\Big|_{transport} + \frac{\partial f_e}{\partial t}\Big|_{E\parallel}, \tag{2.34}$$

with $E_\parallel$ the parallel electric field, ECH the wave-induced velocity diffusion and $\dfrac{df_e}{dt}$ the total derivative of the electron velocity distribution over time. Here, the collision part represents the collisions between electrons as ions are neglected, the transport term representing the radial transport, and the wave-induced ECH flux depends on the type of wave-particle interaction and the velocity-space gradient of the electron distribution function:

$$\frac{\partial f_e}{\partial t}\Big|_{ECH} = \frac{\partial}{\partial \boldsymbol{u}} \cdot \boldsymbol{S}_w \equiv -\frac{\partial}{\partial \boldsymbol{u}} \cdot \boldsymbol{D}_{QL} \cdot \partial f/\partial \boldsymbol{u}, \tag{2.35}$$

with $\boldsymbol{D}_{QL}$ the quasi-linear diffusion coefficient. Note that the electron energy distribution function f is generally unknown. Therefore, the energy distribution is mostly assumed to be Maxwellian before perturbation. A large amount of information can be deduced about $\boldsymbol{S}_w$. The direction of it can be found to be perpendicular for the cyclotron resonance (and parallel for Landau damping) by considering the resonance condition [33]. Its place in velocity space can be found by considering the wave spectrum of the launcher. The magnitude is more difficult, and can be found only by linearisations. For lower levels of injected

power, linear damping theory should be appropriate, as these do not alter the electron energy distribution function (EEDF). At higher powers, the wave-induced change in the velocity distribution should be taken into account.

Fisch-Boozer current drive

The Fisch-Boozer current-drive mechanism (ECCD) is the mechanism that is most commonly used in tokamak experiments. This has to do with the fact that it can drive on-axis current efficiently and has a higher current drive efficiency in present day experiments [24]. This method injects plasma waves at a toroidal angle that preferentially pushes electrons moving in one direction, as the particles moving to the 'left' in the tokamak have a different Doppler shift than the particles moving to the 'right'. The imparting of perpendicular momentum and energy to these electrons moving in one direction causes them to have a lower collision rate, hence creating a net directional current. Note that this current is produced in the absence of parallel momentum-input. The choice of which 'direction' of electrons to heat is then a choice of which Doppler shifted part of the electron distribution to heat, determined by the angle of the incident wave. This process works better for faster electrons, as the probability of cancelling the current (a collision) is also a function of the initial velocity space distribution of the current.

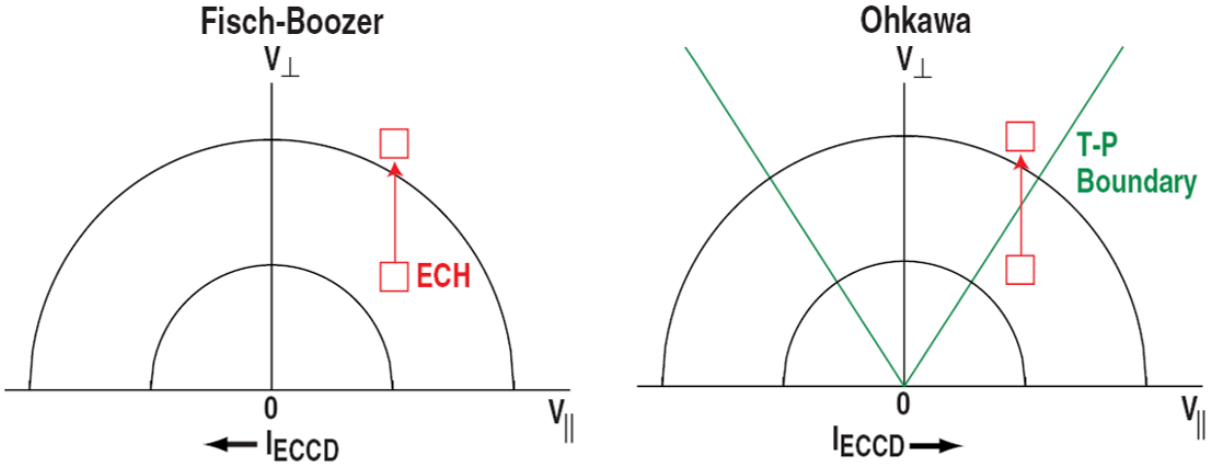

Figure 2.9: Visualisation of the Fisch-Boozer and Ohkawa method of current-drive. Both mechanisms rely on increasing the perpendicular velocity, the Fisch-Boozer one to decrease the collisionality of directional electrons, and the Ohkawa mechanism to push particles over the T-P boundary. The Trapped-Passing (T-P) boundary given by $(v_\perp/v_\parallel)^2 = B_{min}/(B_{max} - B_{min})$, where $B_{min/max}$ are the minimum and maximum values of the magnetic field on the flux surface. Figure adapted from [21].

There is an upper limit for Fisch - Boozer current drive efficiency because of relativistic mass increase. As the cyclotron wave pushes a relativistic electron perpendicularly, the mass of the electron increases, which causes the electrons' parallel velocity to decrease to conserve parallel momentum. The upper limit to the current drive is the negative side effect of this indirect method of current drive, with the current drive efficiency $\eta_{CD} \to 0$ as $p \to \infty$. Luckily, this effect is most often not dominating, but it is clear that this effect has to be taken into account in the current drive calculation. On the other hand, there is also an increase of η_{CD} due to the dragging of bulk electrons by these resonant relativistic electrons. This happens because the difference in velocity of particles moving in the same direction as the relativistic electrons is smaller than the ones moving in the counter-direction. Therefore the co-moving particles are dragged by collisions more than the counter-moving particles are stopping the collisions. The dragging effect highlights the importance of a collision operator that conserves momentum in collisions.

Ohkawa current drive

The Ohkawa current drive mechanism (OKCD), is based on asymmetrically trapping electrons by selectively heating trapped electrons travelling in one direction [23]. This relies on a high trapped electron

fraction, which is mostly the case in the outer half of tokamaks where the mechanism can outperform ECCD [24]. This method of current-drive is generally considered to be less effective than the ECCD mechanism, especially in on-axis current drive. However, it can have a cancelling effect on ECCD as the sign is different, and it gets more efficient with smaller aspect ratio (as with ST's) and higher β_e (as with ST's). Therefore, this method might be especially relevant for the ST-F1 tokamak in driving large amounts of off-axis current-drive for the purpose of tailoring the safety factor profile q or creating inverse pressure profiles. For current drive on the $q = 2$ profile for a high inverse aspect ratio, earlier analysis [24] shows that OKCD outperforms ECCD, sometimes by a factor 2.

Power-dependence of ECCD

Harvey et al. [47] found that there is a non-linear relation between ECCD efficiency and injected power at rf powers above a certain power per volume:

$$P_{\mathrm{rf}}\left(\mathrm{W/cm^3}\right) / \left[n_e \left(10^{13}\mathrm{cm^{-3}}\right)\right]^2 \gtrsim 0.5. \tag{2.36}$$

This effect can be explained by realising that although it takes progressively more energy to increase the momentum of a particle, with a factor $\sim v$, the collisionality goes down with $\sim v^3$. Increasing the total power leads to a larger perturbation of the EEDF, i.e. more electrons with high momentum, i.e. higher current drive efficiency. This effect is found to be small in DEMO scenarios under an injection power of 100MW, but DEMO would have a factor of somewhere between 10 and 1000 (depending on deposition location and scenario) more electrons to heat on one flux surface, so nonlinear effects might be apparent in ST-F1.

Chapter 3

The numerical set-up

Chapter 2 describes the theory of cyclotron waves and wave-particle interaction. In this chapter, first, the codes that are used to calculate the heating and current-drive of ST-F1 are detailed. Then, the codes and their different options are compared. Lastly, the research process is laid out.

To find the maximum achievable current drive efficiency and power deposition, there is the need to calculate the wave propagation, absorbed power, power deposition profile, total driven current and current drive profile for electron cyclotron waves. The equations at hand cannot be solved analytically in tokamak geometry; a resort must be taken to modelling. This chapter presents the two codes, GENRAY and CQL3D, that were used in this research to calculate these questions.

GENRAY and CQL3D were chosen in this project for a combination of their availability and that they have been used and benchmarked in multiple studies of ECH and ECCD [48, 49, 50, 51]. Also, they have been tested on experiments that come closest to the operation of the ST-F1 tokamak, such as the DIII-D tokamak [52, 53]. Furthermore, there was support available for these codes because of a collaboration between PPPL and Tokamak Energy. The two codes are a suit-code, with the output from GENRAY going into CQL3D, and they are developed by the company Compxco.

GENRAY is a modular ray-tracing code developed by Smirnov and Harvey [50]. The GENRAY code was designed with the purpose of being able to modularly use different dispersion and absorption relations to calculate the propagation of waves in plasmas. Furthermore, it is used for the purpose of calculating the wave-propagation and for general linear absorption and current-drive calculations.

CQL3D (Collisional quasi-linear 3D) is a 2D momentum space, multi-species, relativistic, bounce-averaged, collisional/quasi-linear Fokker-Planck equation solver with the capacity of running on non-circular flux surfaces [51]. The CQL3D Fokker-Planck (FP) code is built to calculate the absorption and current drive profiles through solving the bounce averaged FP equation. CQL3D takes the GENRAY ray-tracing output as input to its model, and solves the FP equation on equi-flux surfaces in the plasma. The FP absorption, current-drive and collision model is considered to be 'more physical' than GENRAY. Benchmarking of multiple EC codes for the ITER scenario shows that the absorption and current drive calculations of different codes (also GENRAY and CQL3D) show similar absorption profiles [48]. However, that study also shows that there are physical effects such as momentum conservation in collisions, collisions in general and possibly quasi-linear effects that could have effect on particularly the driven current leading to differences in the two codes [48].

3.1 GENRAY

GENRAY is a modular ray-tracing code developed by Smirnov and Harvey [50]. This code was developed to simplify the use of different dispersion relations for ray-tracing and absorption calculations. The modular set-up of the code gives a high level of flexibility, this code can for instance also be used for Lower Hybrid Current Drive and can work with cold, warm, hot, (non/weakly/fully) relativistic, and combinations of

these options as dispersion relations. Furthermore, it has different options for the calculation of ECCD and absorption. The code calculates the damping of energy and current drive efficiency linearly.
An overview of the code is given in Figure 3.1.The input is the magnetic equilibrium, the launcher location, angle and power and the wave characteristics (frequency, polarisation). The relevant output is the ray trajectory, the power deposition profile, the current drive profile and a lot of wave characteristics along the ray, which are outputted in a file either to be read-out or to be coupled to CQL3D which uses them as input.

Magnetic equilibrium and kinetic profiles

The kinetic profiles can be specified as the combination of a central density and temperature and an exponent. This is a trivial step, and they are specified according to the different scenarios that are considered.

The magnetic equilibrium provides information on the pressure, poloidal current function, q profile on a uniform flux grid from the magnetic axis to the plasma boundary and the poloidal flux function on a rectangular computation grid. GENRAY computes from this the axisymmetric flux surfaces and the magnetic field. GENRAY also has the possibility to perturb the magnetic field to simulate the influence of the magnetic ripple, but this capability is not exercised. The way the magnetic equilibrium is defined is in itself not unique, there are many ways that it is defined and not every specified magnetic equilibrium works with GENRAY. However, for this project the magnetic equilibrium that was found using the ASTRA-spider transport code [54] which proved to be compatible. This option was a fortunate legacy from the earlier attempts at MHD-stability modelling with ASTRA. This ASTRA-spider code [54] allows the calculation of the magnetic equilibrium for user-specified kinetic profiles and magnetic field. These are chosen to be the same as the relevant scenarios.

Launcher specification

The specification of the hardware is where most of the variables are that are tuned in this thesis. Here, the wave frequency, polarisation, amount of rays, launcher location and angle, and launched wave power are specified. The launched wave itself can be changed by specifying its frequency in GHz and its polarisation: X - or O-mode. The other characteristics reside in the launcher specification. For the launcher, there are more options. The launcher location can be specified to be anywhere outside the plasma. The launcher can have two angles: the toroidal angle, α, which is the angle relative to the vector pointing outward from the centre of the machine to the launcher, the poloidal angle, β, which is an angle defined in the X-Z plane deviating from the plane of the launcher height. These angles determine the parallel refractive index, $N_{\|}$, the trajectory of the wave through the plasma and where the wave is absorbed.

GENRAY is a linear code, so the launched wave power is a scalar factor. This factor is, important for the coupling to the quasi-linear Fokker-Planck codes and therefore taken into account. For the same purpose, the electric field polarisation is calculated along the wave for coupling to Fokker-Planck codes (such as CQL3D).

Lastly, there is the option to specify the proxy for a Gaussian beam, multiple rays. These rays are spatially separated, and the distribution of them is determined by the specified amount of rays. Somewhere between 30 and 100 rays should suffice to artificially simulate a Gaussian Beam [48].

Physical model

In most of the literature that is found, the cold and sometimes the relativistic dispersion relations are used [48] [49]. Then, there is an absorption module, that calculates the absorption of wave power by the imaginary part of the perpendicular refractive index. Here also, there is a choice between different calculation options of the absorption coefficient α,

$$\alpha = \mathrm{Im}(\boldsymbol{k}) \cdot d\boldsymbol{l} = \frac{\mathrm{Im}(\boldsymbol{k}) \cdot \boldsymbol{V}_{gr}}{V_{gr}} d\boldsymbol{l} = \frac{\omega}{c} \frac{\mathrm{Im}(N_{\perp}) V_{gr_{\perp}}}{V_{gr_{\perp}}} dl_p. \tag{3.1}$$

GENRAY then has several possibilities for calculating $\mathrm{Im}N_{\perp}$, which are the absorption calculation choices.

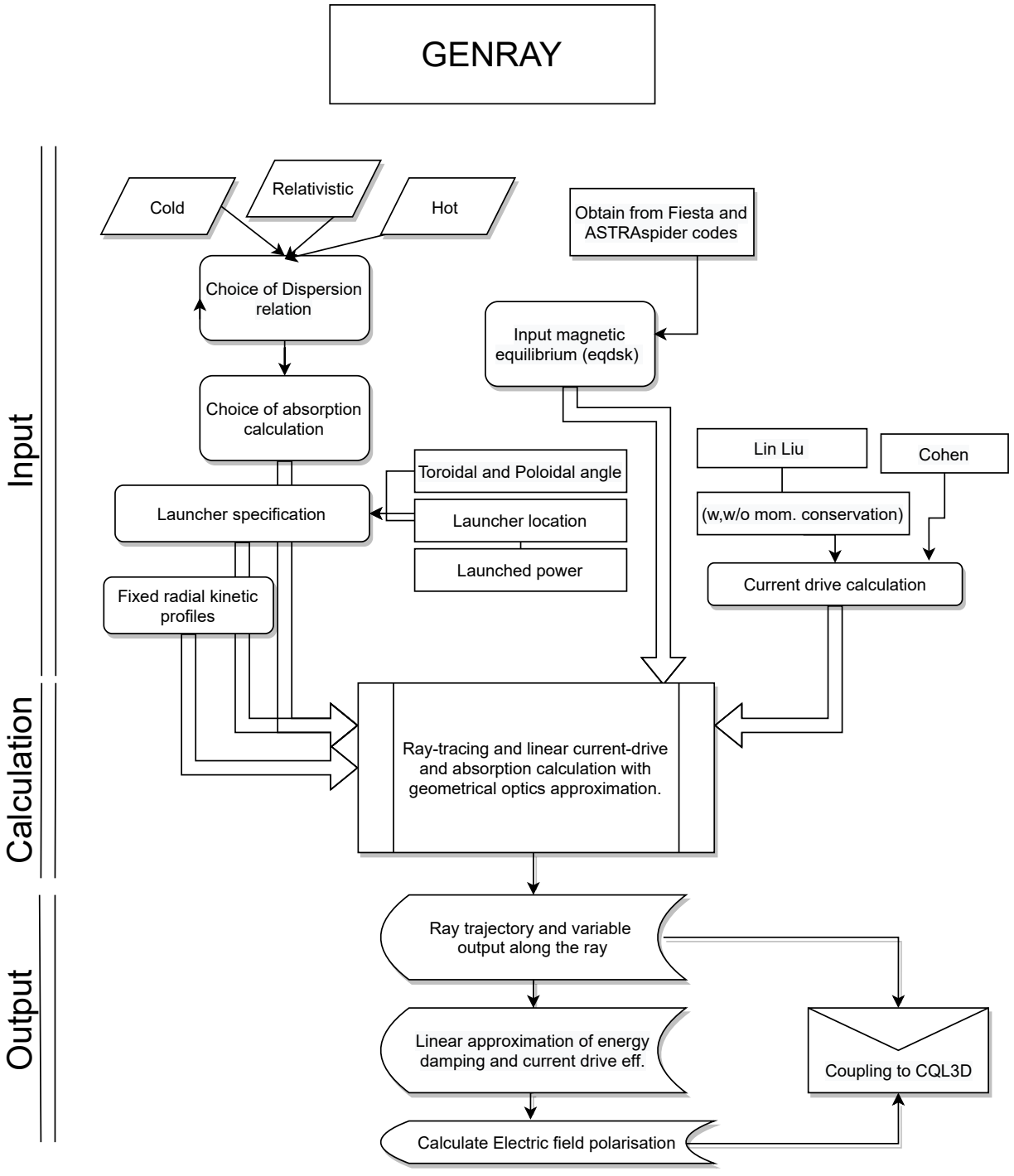

Figure 3.1: GENRAY structure interpreted from [50] specifically for EC waves.

Lastly, there is the calculation of the current-drive. For EC waves there are three options in GENRAY, of which one is just a scalar multiplication of the power absorption profile. This does not seem to be an accurate representation of ECCD, so the other two options are used, the Cohen module [55] and the Lin Liu module [26]. Both models are based on a Green's function formulation of current drive efficiency and they approximate the high-velocity collision operator by an expansion in T/mu^2 where u is the momentum per unit mass [45]. The Lin Liu version is a modification of the Cohen calculation that includes arbitrary magnetic field geometry and fully relativistic electron dynamics. Furthermore, the Lin Liu module has an option to include momentum conservation in electron-electron collisions, which is interesting as that can give insight in the physics at hand. The additional physics accounted for in the Lin Liu module make it the option used in this thesis. Comparisons show that the current-drive prediction by both modules generally differs little, except when the electron-electron collision operator is turned on.
The GENRAY model assumes that the launched beam does not perturb the electron energy density function (EEDF), so that the electrons can be defined as a Maxwellian distribution with a central temperature. Ray-tracing does not take into account the effects of the beam on itself: diffraction and interference. The only way to get something that looks like a Gaussian beam, is to simulate a bundle of multiple beams, where 30 to 100 pinpoint beams are necessary [48].

3.2 CQL3D

CQL3D (Collisional quasi-linear 3D) is a 2D momentum space, multi-species, relativistic, bounce-averaged, collisional, quasi-linear Fokker-Planck equation solver with the capacity of running on non-circular flux surfaces [51]. A high-level overview of the code for EC purposes is shown in figure 3.2. The three dimensions consist of two dimensions in velocity space, where the third dimension arises from the bounce-averaging over flux surfaces, leaving only one 'configuration space' dimension which is the radial dimension. The assumption that the bounce time of the particles is shorter than the collision time $\tau_{\mathrm{b}} \ll \tau_{\mathrm{coll}}$ leads to the variables being constants of motion on flux surfaces. CQL3D takes the ray tracing output along the ray from GENRAY, or other ray-tracing codes for that matter, and uses the Stix [30] theory of EC quasi-linear diffusion in velocity space as input to the Fokker-Planck equations to calculate absorption and current drive. The code solves the different moments of the FP equations on flux surface averages determined by user specified mesh points. Then, along the inputted ray lines, it calculates the different moments of the bounce averaged Fokker-Planck equations. This code allows for a more complete account of the effects relating to absorption and current drive than the GENRAY modules: The Fokker-Planck approach allows the taking into account of the actual velocities in the collision operator (instead of the high velocity limit used in the adjoint approach) [48], CQL3D retains momentum conservation in electron-electron collisions, and takes into account the change in the velocity distribution function due to wave absorption.

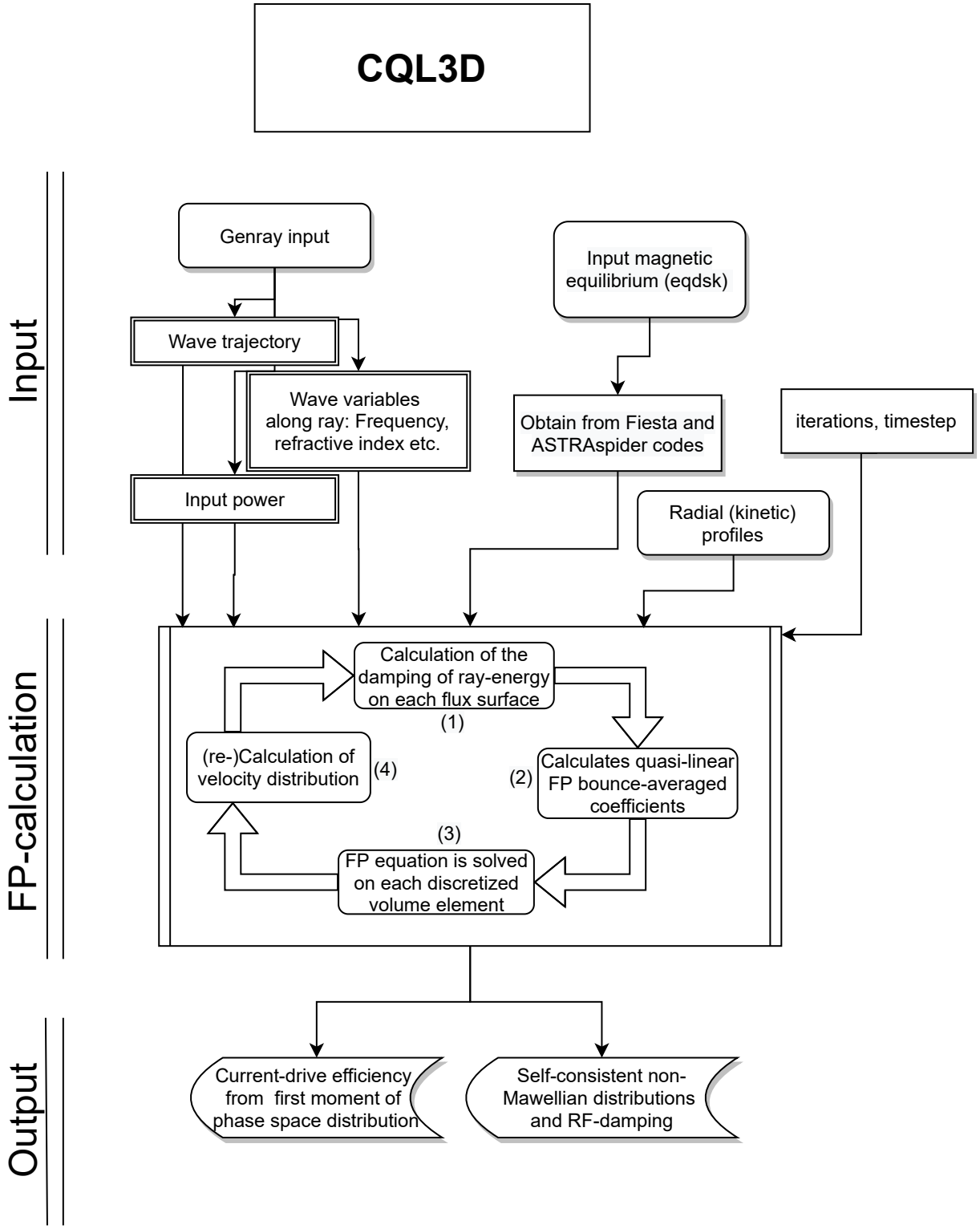

Figure 3.2: CQL3D structure adapted from [51] specifically for EC waves.

The Fokker-Planck equation

A Fokker-Planck solver solves for the different moments of a particle distribution function in velocity space. The inputs are the different operators working on the distribution function as in equation 2.34. This distribution function in velocity space is then a variable of time and the specified inputs. The velocity distribution is taken to be Maxwellian in the first step, but perturbed by the different acting effects in the following calculation steps. This way of modelling the distribution function does take into account the perturbation of the Electron Energy Distribution Function (EEDF) by ECH and is therefore more physical than the linear approach, which just assumes an unperturbed Maxwellian with a specified central average velocity. The same reasoning goes for the collision operator, where the Fokker-Planck models can include the change in the velocity of particles to calculate the collisionality of the species.

The $E_{\|}$ term signifies the parallel electric field at the point of evaluation. In the case of the ST-F1 FP modelling, this will be unimportant, because there is no central solenoid generating a parallel electric field in the design. Only a small value for this $E_{\|}$ is implemented, because otherwise the model does not run, this is detailed later.
One major difficulty for specification of this approach is the transport term. Transport in a tokamak is often anomalous, and not very well understood. This term is not taken into account in this thesis. There are studies on tokamaks that show that this can have a significant effect on ECCD [21], but in these studies the electron confinement is low, and electron transport is relatively high [19]. With the high-field approach and high density operation, ST-F1 is expected to fall in the good electron confinement regime.

Model input

For CQL3D, the kinetic profiles and magnetic equilibrium are defined to be the same as in GENRAY. Furthermore, all the wave specifications are retrieved from the GENRAY outputs. Apart from these, the user is left to specify the mesh points, the time and timesteps and the different physics to take into account. Furthermore there are different simulation parameters to specify, some of which are treated below.

Physical model

CQL3D is a code that is 2D in momentum space, where the third dimension comes from the bounce-averaging over flux surfaces. CQL3D's physical model starts by taking the drift-kinetic version of the Fokker-Planck equation for the velocity distribution in a plasma:

$$\frac{df}{dt} = -\nabla_{\boldsymbol{u}} \cdot \boldsymbol{\Gamma}_{\boldsymbol{u}} + R(f) + S, \tag{3.2}$$

with $\frac{df}{dt}$ the total derivative of the particle guiding centre, S a particle source/sink term (not applicable to ECH/CD), $R(f)$ the radial transport operator and :

$$-\nabla_{\boldsymbol{u}} \cdot \boldsymbol{\Gamma}_{\boldsymbol{u}} = C(f) + Q(f) + H(f). \tag{3.3}$$

Here, $C(f)$ is the collision operator, $Q(f)$ is where the absorption of EC waves is taken into account; the quasi-linear diffusion operator, and $H(f)$ the synchrotron radiation term which is not used in this thesis. The assumption is then made that there is 'zero-banana-width', which means that the guiding centers of the particles are assumed to move on flux surfaces identified by the radial coordinate ρ. This means that there is no perpendicular drift and that the magnetic moment is conserved. The following assumption is the bounce-averaging part. One bounce is defined as the time it takes an electron to complete a closed orbit in a magnetic trap. Bounce-averaging entails that only processes of time-scales longer than the bounce-period are taken into account and particles are evaluated from the lowest magnetic field point until they return, so one 'bounce'. The bounce average integral is then:

$$\langle\langle()\rangle\rangle \equiv \frac{1}{\tau_{\mathrm{B}}} \oint' d\tau(), \tag{3.4}$$

with the integral being over one bounce, and τ_B:

$$\tau_B = \int_p \frac{dl}{v_{\|}(\epsilon_p, \mu)}. \tag{3.5}$$

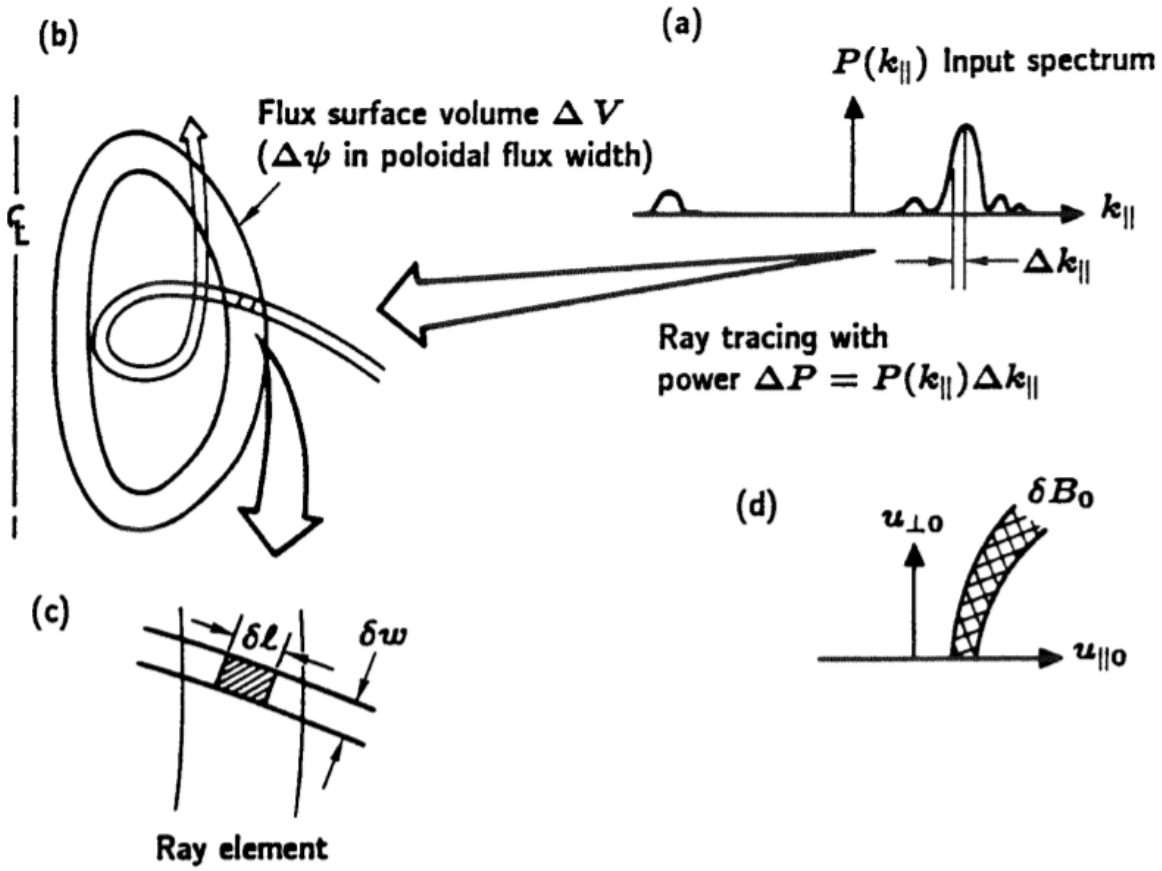

Figure 3.3: Here, δB_0 is the contribution to the quasi-linear coefficient B_0. Figure from CQL3D manual [51].

The terms for the quasi-linear diffusion operator are reconstructed from the ray-tracing data. The equation is expanded and bounce-averaged to obtain equations that can be solved numerically.

The QL diffusion coefficients are calculated based on the input ray-tracing data data. A visualisation of the calculation of coefficients that go into the QL diffusion is given in Figure 3.3. The input power spectrum is discretised in $k_{\|}$, leading to a ray power of $\Delta P = P(k_{\|})\Delta k_{\|}$. The ray trajectory input from GENRAY, and the contributions to the diffusion coefficient (δB) are calculated by integrating over the flux averaged volume and path. The change in the electron energy distribution function is then given:

$$\left.\frac{\partial f}{\partial t}\right|_{q\ell} = \frac{\partial}{\partial \boldsymbol{u}} \cdot \left(\boldsymbol{D}_{q\ell} \cdot \frac{\partial f}{\partial \boldsymbol{u}}\right), \tag{3.6}$$

where $\boldsymbol{D}_{q\ell}$ is the quasi-linear diffusion operator found by integrating over the different contributions δB along the ray.

The other input to the Fokker-Planck equation is the collision operator. This collision operator is the following [51]:

$$\left.\frac{\partial f_a}{\partial t}\right|_c = -\nabla_{\boldsymbol{u}} \cdot \boldsymbol{\Gamma_c}, \tag{3.7}$$

with Γ_c the collision-induced flux vector. The treatment of collisions in CQL3D is fully relativistic based on Ref. [56]. The collision operator used in CQL3D is more sophisticated than the one used in GENRAY, in that it self-consistently conserves momentum in electron-electron collisions [48]. This consideration keeps intact the 'dragging' effect fast electrons have on slower electrons and is consistent with other Fokker-

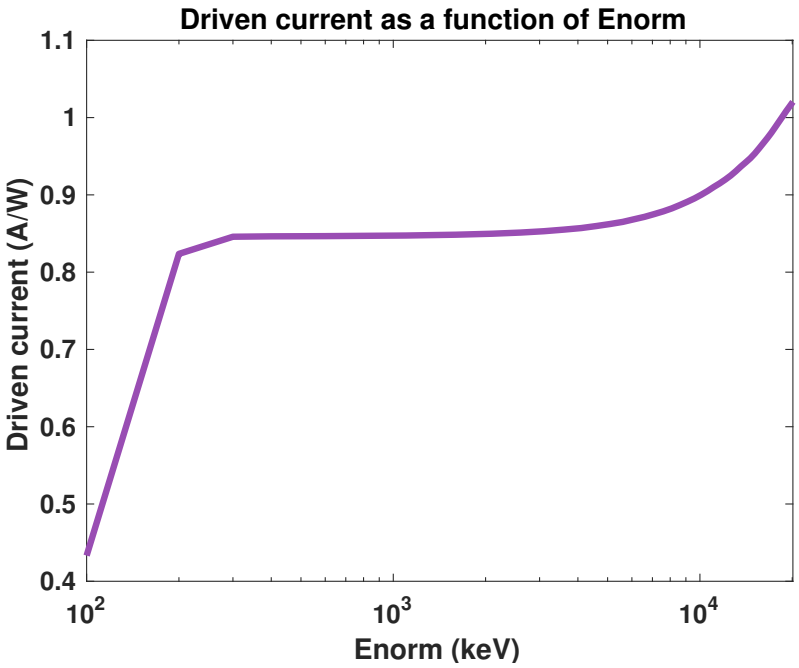

Figure 3.4: Driven current calculated by CQL3D for a 112 GHz LFS launch case, with a toroidal angle of 200 degrees as a function of the energy normalisation parameter Enorm.

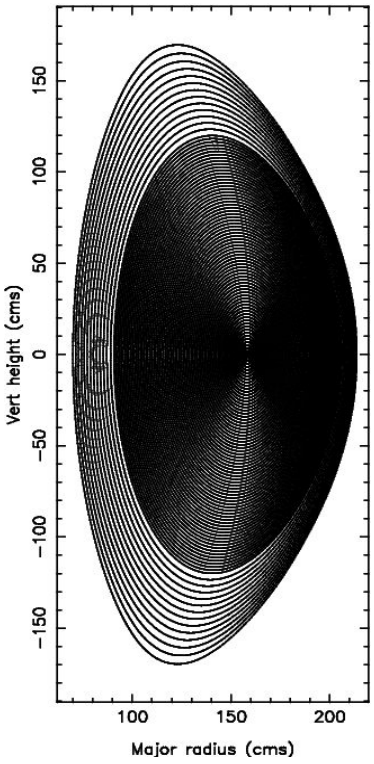

Figure 3.5: The employed CQL3D calculation mesh, each black line shows a location where the Fokker-Planck equation is evaluated.

Planck findings [48].

Some physics handling can be turned on or off in CQL3D. It is possible to switch on or off relativistic effects, electron-electron collision momentum conservation, time evolution of temperature profile, radial diffusion/transport, and synchrotron radiation.

CQL3D simulation parameters

Choices were made with respect to the simulation parameters in CQL3D. Non-trivial choices or choices that were made due to problems encountered are explained here.
In the **mesh** definition, a compromise is made between CQL3D run-speed and precision. In the outer regions, the mesh is defined at every 0.02 rho, and in the inner regions at every 0.01 rho, leading to 84 mesh points. This compromise has mostly shifted to precision, and the mesh that is used for all of the presented runs is shown in Figure 3.5. This mesh specifies the flux surfaces at which the Fokker-Planck equations are solved. The evaluation of the code starts at the outer mesh point and loops over them for each time-step. The CQL3D code had some unexplained issues with values of rho higher than 0.97. So the code skips over the 0.98 and 1.00 rho flux surfaces. The region between $\rho = 0.96 - 1$ is thus treated as one flux surface. No significant problems are expected from this one 'large' flux surface, as this region is not the main region of interest for electron cyclotron absorption and current-drive.

Enorm is the cut-off maximum energy in keV at which the distribution function is evaluated [57]. Initially, the setting for this was 100 keV in the CQL3D namelist file. The results that were found with this were unexpected: Particularly the current-drive was very different and lower than the current-drive obtained with GENRAY. After comparison with namelist files for DIII-D and attempting to recreate the results for

ITER runs in [48], the Enorm variable was found to be the value in the runs that was different. The value is a cut-off for the used electron energy, and it is particularly important as the higher energy electrons tend to carry a large fraction of the current (they collide less often and move fast). Enorm values of lower than 200 keV give very low current drive prediction, indicating that the value might be too low. This can also be seen in Figure 3.4, where the current-drive for the same launch parameters is calculated. Everything is kept the same but the Enorm value. The driven current stabilizes after 300 keV, and only goes up after the unrealistic values of 10000 keV. In accordance with one of the few studies that comments on Enorm [57], a value of 2500 keV is used in this project.

The parallel **electric field** is user-specified in CQL3D. As stated before, the inductive parallel electric field is non-existent due to the absence of a central solenoid. To find agreement with experiments, this parameter should be taken into account [21], but the This parameter cannot be set to zero in the code. It should however be set low enough to not drive any current of its own as ST-F1 does not have a central solenoid. At values of $E_{\|}$ below 10^{-13}V/m, the contribution to the driven current is less than 0.1% at an input power of 1 kW. The electric field is thus specified to be 10^{-15}V/m in the runs.

3.3 Test case: comparison of CQL3D and GENRAY deposition profiles

Here, as one benchmark case, the power and current deposition profiles calculated by CQL3D and GENRAY are shown using different dispersion relations. For the absorbed power, the power density is multiplied by the flux-surface volume to show the absorbed power for each grid point.

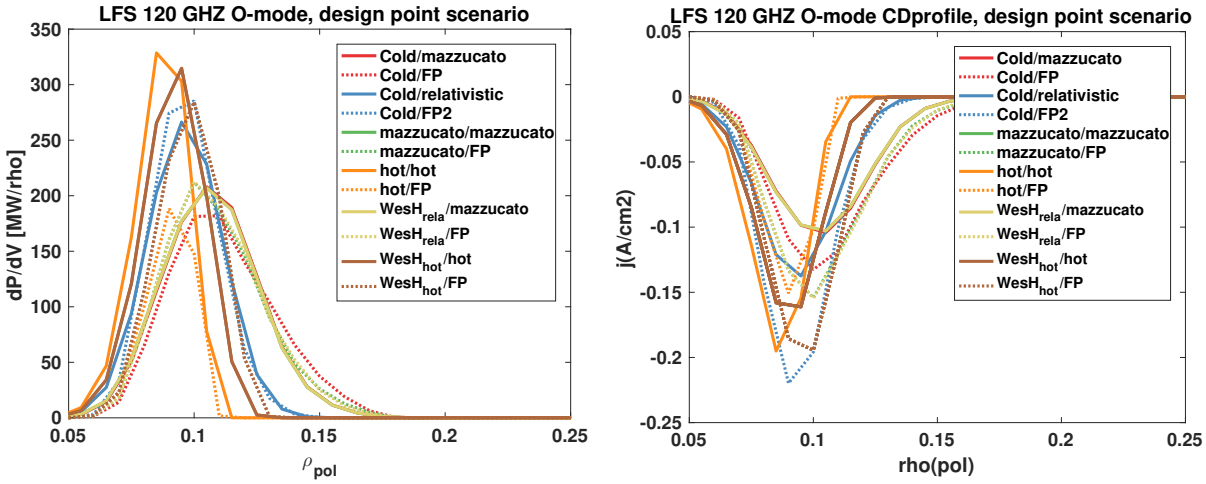

Figure 3.6: Absorption (left) and current drive (right) profiles for different dispersion and absorption choices for a 120GHz O-mode LFS heating scenario. Dotted lines are CQL3D calculations, straight lines GENRAY. The current-drive is calculated with the LinLiu subroutine without momentum conservation.

In the calculation where a hot dispersion relation is used, with CQL3D FP absorption and current drive (Orange dotted line in Figure 3.6, the absorption is about half of what it is in the GENRAY calculation with a hot dispersion relation and hot absorption calculation. This discrepancy might be caused by a coupling error in this case. One indicator of this, is that the Westerhof hot dispersion relation does not show this discrepancy, which means that it is not an artefact of hot dispersion in general. The total driven current is consistently 15% higher for the CQL3D calculations than in GENRAY (except for the hot dispersion as there is less absorption there). This is precisely the expected size of including momentum conservation in current-drive calculations [48].

3.4 Research method

This section lays out the method that is used to find answers to the research questions. First, the variables that are taken into account are given. Then, the constraints, ranges and choices in the variables are summarised. It is not possible for this thesis to make a continuous scan over all the variables to find an absolute maximum. Not only would this be computationally impossible, it also makes little sense to absolutely calculate something for a device that is still in the design phase. The choice is therefore made to perform a discretized scan. This entails that there is a discretisation of the modelling parameters based on reasoning for each parameter.

Relevant parameters

The variables of the cyclotron current-drive system are: the location of the launcher, the frequency of the waves launched, the polarisation of the waves (O- or X- mode), the power from each launcher and the toroidal and poloidal angles β and α of the injected waves.

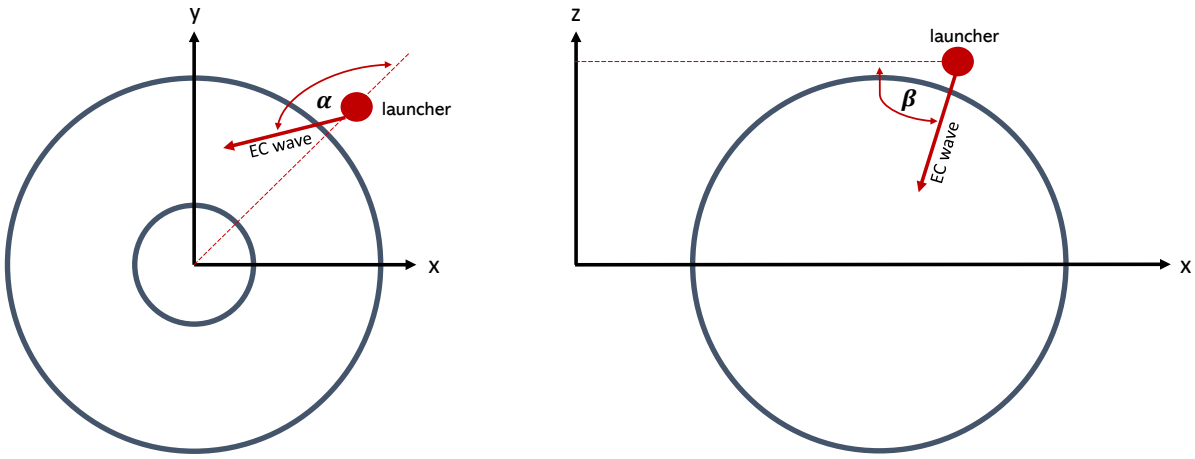

Figure 3.7: The launcher location is specified by the height Z and the toroidal radius R. Then, the angle coordinate system of GENRAY is such that it is oriented with respect to a line through the 'origin'. Then, the angle α determines the angle in the X-Y plane with respect to this line, and the angle β determines the angle in the X-Z plane with respect to this line. Together these angles span all possible launch angles.

The constraints on the *location* of the launcher are in the engineering and control space. No waves can or should be launched through the divertor X-point due to the high density and therefore chances of distortion and reflection there, there are difficulties associated with HFS launch due to possible plasma breakdown in the wave-guide and in general the LFS and, less problematically the TL have to deal with the change in the magnetic field pitch angle during start and ramp-up of the plasma current. Because of the lack of space on the HFS, only low field side and top launchers are considered.

For the low field side launcher, the horizontal launch of EC waves is considered. This is done for the following parameters:

- Toroidal angle α varied from 180 to 230 degrees in steps of 2.
- Frequency from 110 GHz to 235 GHz in steps of 5
- Launcher radial location at R = 2.2 m.
- Poloidal angle $\beta = 0$
- Launcher height $Z = 0$

For the top launcher, two different types of parameter scans are considered. First, a broad scan was considered using different launcher locations. This had the following parameters:

- Toroidal angle α varied from 9 to 81 degrees in steps of 3.
- Frequencies: 112, 140, 170, 200, 224, 240 GHz.
- Launcher radial location from R = 1.4 − 1.9 m in steps of 0.1 m.
- Poloidal angle β form -92 to -161 degrees in steps of 3 degrees.
- Launcher height $Z = 1.8$ m.

This gave some uncertainty in the very broad frequency steps, so another scan was performed for a top launcher with a fixed location but with a smaller frequency step:

- Toroidal angle α varied from 9 to 81 degrees in steps of 3 degrees.
- Frequencies: 110 to 230 GHz in steps of 5 GHz.
- Launcher radial location at R = 1.5 m.
- Poloidal angle β form -92 to -161 degrees in steps of 3 degrees.
- Launcher height $Z = 1.8$ m.

All the scans are performed with GENRAY with a cold dispersion relation, Mazzucato absorption, relativistic resonances and a Lin Liu current-drive calculation routine with momentum conservation. These settings had enough run-speed to perform a large fraction of the runs within a week time. The corrections are taken into account in the following section.

Physical options and probability estimate

The parameter scan should yield different optimal parameters in terms of current drive. These optima are what we are interested in, but these optima have an error margin. To make a probability estimate for these optima, understand the physics and effect of the launched power and to analyse where the power is absorbed and where and how much current is driven, these optimal parameters are taken, and different launched powers, dispersion and absorption relations are used to re-calculate the current-drive and absorption. These new calculations serve as a probability range. Especially in the Top Launch scenario, it is expected that these might show a relatively large spread, due to the absorption calculation and dependence of the absorption on the velocity distribution (i.e. T_e). The waves are launched vertically and often do not directly pass the resonance layer. For the LFS the difference is expected to be smaller, as the waves always travel through the resonance and absorption is therefore more localised and more easily interpreted.

After these steps, there should be an estimate of the achievable current-drive efficiency in the different scenarios. For the design of the ST-F1 machine it is also relevant to investigate the scaling of these current-drive efficiencies with temperature and density. Here, the expectation is to regain the theoretical scaling of equation 2.33, so $\eta_{\mathrm{CD}} \propto \dfrac{T_e}{n_e}$.

Chapter 4

Results

In this chapter, the research question is addressed by showing the modelling results. First, the results of GENRAY and CQL3D in terms of current-drive are compared. Then, the parameter scan results are treated by showing the top cases. Thirdly, the specific cases with the highest current-drive are investigated by comparing the GENRAY and CQL3D results for those launcher set-ups, and implementing different dispersion, absorption and current-drive options. Then, the scaling with temperature and density for these high current-drive cases is investigated. Next, the dependence of current-drive efficiency on power deposition are shown for three top launcher and three low-field-side launch options.

The kinetic profiles of the scenarios that are taken into account are shown in Figure 4.1. Here, the design point scenario is the scenario that is used to achieve a $Q_{\text{fusion}} = 3$, the high density scenario is there to chart the effect of higher densities on the achievable current-drive and accessibility, and the low density scenario is there to mimic a start-up scenario, with low density but relatively high temperatures.

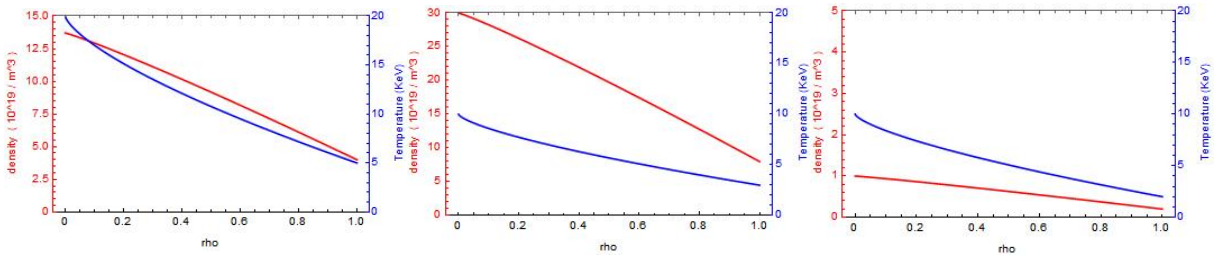

(a) Scenario 1:Design point (b) Scenario 2:High density (c) Scenario 3:Low density

Figure 4.1: Temperature and density profiles of considered scenarios.

4.1 Benchmarking GENRAY and CQL3D current drive

To verify that GENRAY and CQL3D give similar results and to start to understand the differences, parameter scans have been done with both GENRAY and CQL3D and the results are compared here. Three top launch cases are investigated, followed by two LFS launch cases. In all cases, the input power is kept low at $P = 1$ kW to rule out non-linear effects in CQL3D.

The three top launch cases are:

- Case 1: 140 GHz TL O-mode launch for the design point scenario with a launcher at $R = 1.5$ m, results in Figure 4.2.
- Case 2: 170 GHz TL O-mode launch for the high density scenario with a launcher at $R = 1.5$ m, results in Figure 4.3.
- Case 3: 224 GHz TL X-mode launch for the design point scenario with a launcher at $R = 1.5m$,

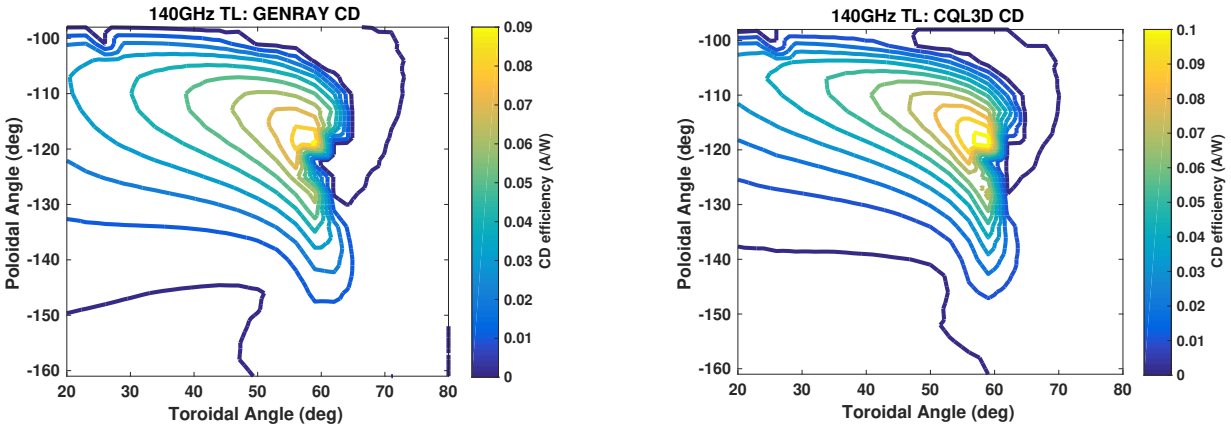

Figure 4.2: The GENRAY (left) and CQL3D (right) calculations of current drives efficiency in the design point scenario for a top-launcher with a frequency of 140 GHz O-mode launch at R = 1.5m as a function of toroidal angle and poloidal angle.

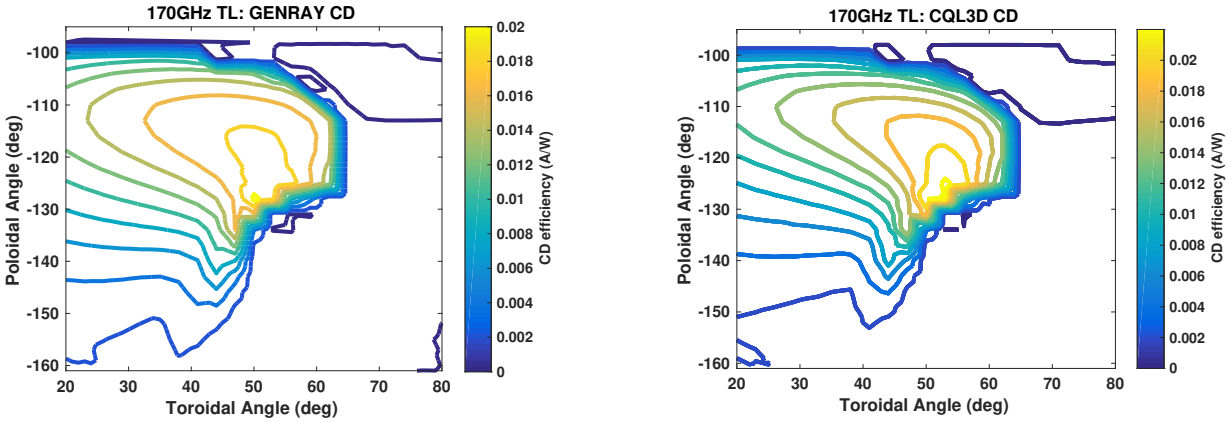

Figure 4.3: The GENRAY (left) and CQL3D (right) calculations of current drive efficiency in the high density scenario for a top-launcher with a frequency of 170 GHz O-mode launch at R = 1.5m as a function of toroidal angle and poloidal angle.

results in Figure 4.4.

The two LFS launch cases are:

- Case 1: 112 GHz O-mode launch from the LFS. Both the fraction of absorbed power and the current-drive efficiency are plotted against toroidal angle in Figure 4.5.
- Case 2: 200 GHz O-mode launch from the LFS. Both the fraction of absorbed power and the current-drive efficiency are plotted against toroidal angle in Figure 4.5.

The comparison of the two codes is especially interesting in the case where waves are launched from the top of the machine. In that case, the waves travel parallel to the resonance for multiple launch configurations. A priori, it is expected that these results are similar though some difference might arise. The current drive and absorption calculation is different in the two codes, and the absorption is dependent on the electron energy distribution where GENRAY uses the Maxwellian assumption and CQL3D uses a varying distribution.
Note that in Figure 4.4, a second harmonic X-mode wave being launched near its resonance is shown, with a 224 GHz X-mode launch on R = 1.5 m. This means that the wave is absorbed very quickly after it is injected, which leads to a somewhat dissimilar profile than the figures above. Furthermore, the quick

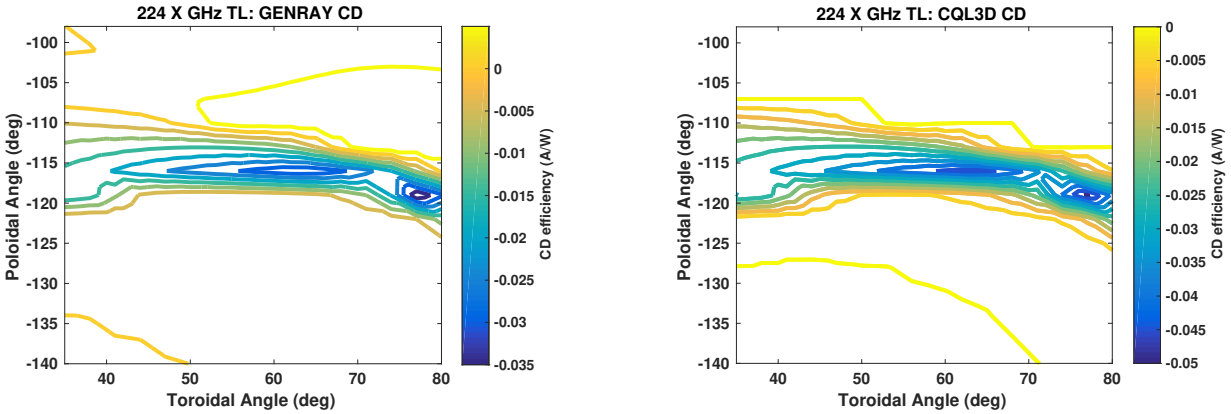

Figure 4.4: The GENRAY (left) and CQL3D (right) calculations of current drives efficiency in the design-point scenario for a top-launcher with a frequency of 224 GHz X-mode launch at R = 1.5m as a function of toroidal angle and poloidal angle.

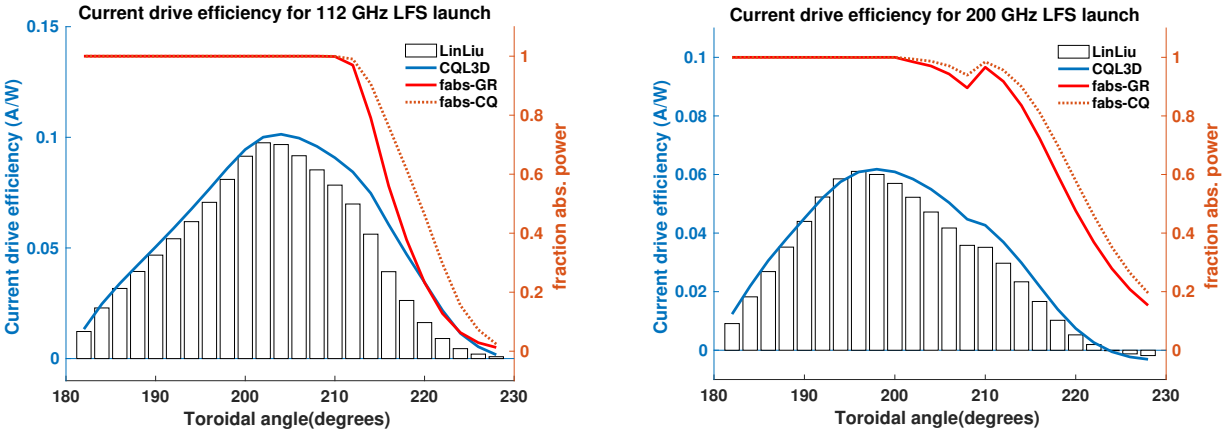

Figure 4.5: The GENRAY and CQL3D calculations of current drives efficiency and the fraction of absorbed power in the design-point scenario for LFS launch with 112 GHz and 200 GHz O-mode launch as a function of toroidal angle. Here, the bars and the blue line, are the current drive efficiency calculated by GENRAY and CQL3D respectively, fabs is the fraction of absorbed power calculated by GENRAY (red) or CQL3D (orange dotted).

absorption also means that the main current drive mechanism there is the Ohkawa current-drive.

For the LFS, GENRAY and CQL3D are also compared. In Figure 4.5, the current-drive efficiency and fraction of absorbed power are calculated with GENRAY and CQL3D for an equatorial launcher with different toroidal angles.
The most notable difference between the codes here is in the calculation of the absorbed power, which indicates that CQL3D finds more absorption at positions further away from the resonance. This might be due to the non-Maxwellian electron energy distribution that CQL3D uses, and due to the fact that the varying temperature could increase and therefore cause more absorption.

In this section, it becomes apparent that for these scenarios there is only a small qualitative difference between the two codes, and only a ~ 10 % absolute difference in the calculated current drive. Furthermore, the Ohkawa current drive mechanism that dominates in Figure 4.4 is also qualitatively similar in the codes, although the difference in magnitude is more sizeable with $\sim 30\%$. These results indicate that the two codes give similar results in terms of current drive, and give confidence in the settings of these codes and the overall results.

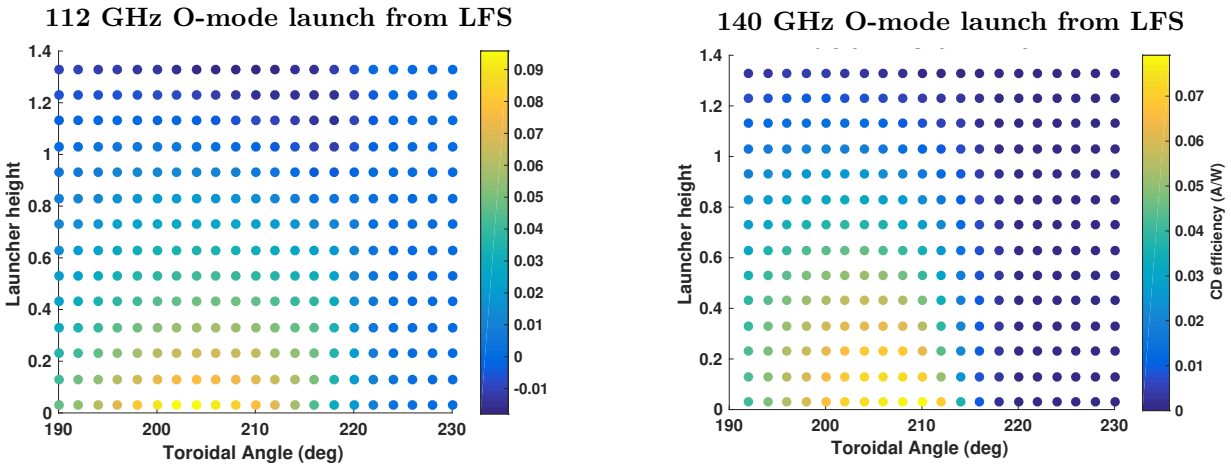

Figure 4.6: Scan of current-drive efficiency with launcher height for 112 GHz (left) and 140 GHz (right) LFS launch calculated by GENRAY with the Lin Liu subroutine and momentum conservation in collisions.

4.2 Parameter scan results

This thesis set out to identify the maximum current drive efficiency for the ST-F1 Spherical Tokamak. This section summarizes the results of the performed parameter scans, by highlighting the maximum current-drive efficiency for the parameter scans performed at different frequencies. The high-level function of the parameter scans is to create a good sense of the different current-drive efficiencies that can be obtained for different launchers.

For the Low Field Side launcher, the highest current drive efficiency is expected to be obtained with an equatorial launcher, so launched from the middle at the outer side of the torus, at a toroidal injection angle between 15 and 40 deg from perpendicular. For this configuration, the region of absorption should have the highest temperature and the angle should be such that there is an optimum in the selective heating of directional electrons. This is corroborated by Figure 4.6.

For the top launcher, the case is less intuitive and depends more on the plasma conditions. The waves are expected to drive a current the most efficiently when they travel parallel to the cyclotron resonance and are absorbed by the fast electrons. The population of fast electrons is dependent on T_e, the rate of absorption is dependent on a combination of temperature and n_e. Therefore, if there is a change in temperature or density, the optimal combinations of toroidal angle and poloidal angle will also change.

For the parameter scans, the cold dispersion relation is used combined with the Mazzucato absorption calculation. This combination is computationally light, which enabled the scanning of a wide range of parameters. The relativistic Westerhof-Tokman relation that mainly has a correction for absorption phenomena when the wave travels parallel to the resonance (i.e. in top launch) was used in multiple instances to verify the results. This yielded a maximum deviation of 3 degrees toroidally *and/or* poloidally for the combination of parameters that had the highest current-drive efficiency. The difference in the maximum calculated current-drive efficiency had a maximum of 5%.

LFS parameter scan

For the low field side parameter scan, we keep the launcher located at the equatorial line. The scan for each scenario is then over the frequency and toroidal angle. For the O-and X-mode, the current drive efficiency, location of maximum power absorption, and the fraction of absorbed power in the first pass are plotted. The following figures show this scan over parameters for the three scenarios, with the values calculated by the cold GENRAY dispersion relation with CQL3D absorption and current-drive. The power is kept at 1 kW.

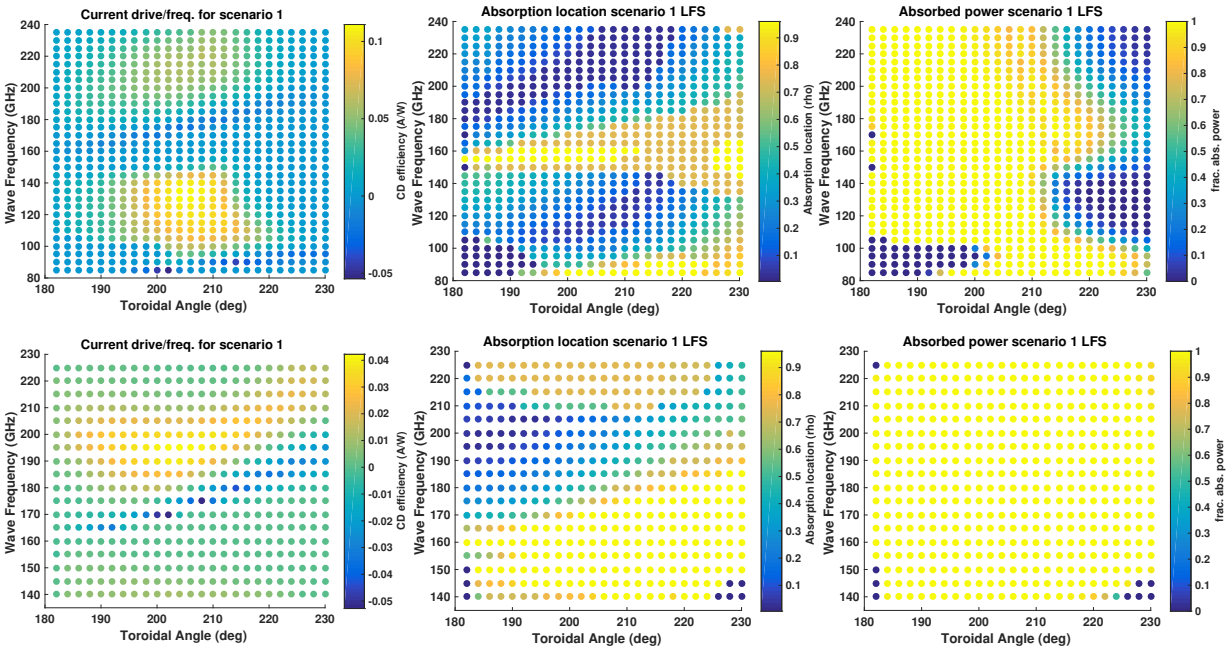

Figure 4.7: O-mode (top) and X-mode (bottom) LFS frequency scan for scenario 1, showing the current-drive efficiency, absorption location and absorbed power fraction calculated with a cold propagation dispersion relation with GENRAY, and absorption and current-drive by CQL3D.

From the scenario 1 plots, the maximum current-drive efficiency is 0.107 A/W for a 125 GHz O- mode launcher. It is visible that the O-mode launch has better current-drive properties for LFS launch. For a large part, this is because the second harmonic X-mode launch is absorbed before it can reach the centre, due to absorption at the edge by the (down-shifted) third harmonic resonance. This effect is evidenced from the maximum absorption location of the waves, and can also be gathered by looking back at Figure 2.8.
From the scenario 2 plots, a different picture arises. Here, the strongest current-drive efficiency is found for the second harmonic 170 GHz X-mode in the edge through Ohkawa current-drive: (-)0.239 A/W. The first harmonic O-mode is not reachable as it is in cut-off and the second harmonic O-mode does have some current-drive, but it is not as efficient. Also note that the effect of the down-shifted third harmonic is smaller for second harmonic O-mode, as the absorption coefficient is smaller than for second harmonic X-mode (as with Ref. [41]).
From the scenario 3 plots, the picture is again different. Here, the cut-off frequency is so close to the resonance, that fundamental X-mode absorption is possible when the toroidal angle and Doppler shift are large enough to put the resonance before the cut-off, leading to very high frequencies for the X-mode current-drive scan of 2 A/W for a 125 GHz LFS launcher. This is almost a magnitude higher than the 0.34 A/W current-drive in the first harmonic O-mode case. The first harmonic X-mode launch type might be very interesting for start-up and (very) low density runs, however, this option would already be cut-off for small increases in density. Another observation, is that the absorption does not appear to be localised enough for second harmonic X-mode Ohkawa current-drive in the edge for these parameters.

Top launch parameter scan

For the parameter scans of the top launcher, there are more parameters to take into account. So not all frequencies, launcher locations and angle combinations can be shown in one plot. Here, the frequencies with the highest current-drive are shown for each scenario when the launcher is located at R= 1.5 m, along with their absorption location and fraction of absorbed power.
This scan for 150 GHz top launch shows that efficient current-drive can be driven by a top launcher, with absorption around the $\rho \sim 0.5$ surface. It also shows that the maximum current-drive efficiency is obtained with a configuration that nearly misses the resonance. This is also the location where the highest energy

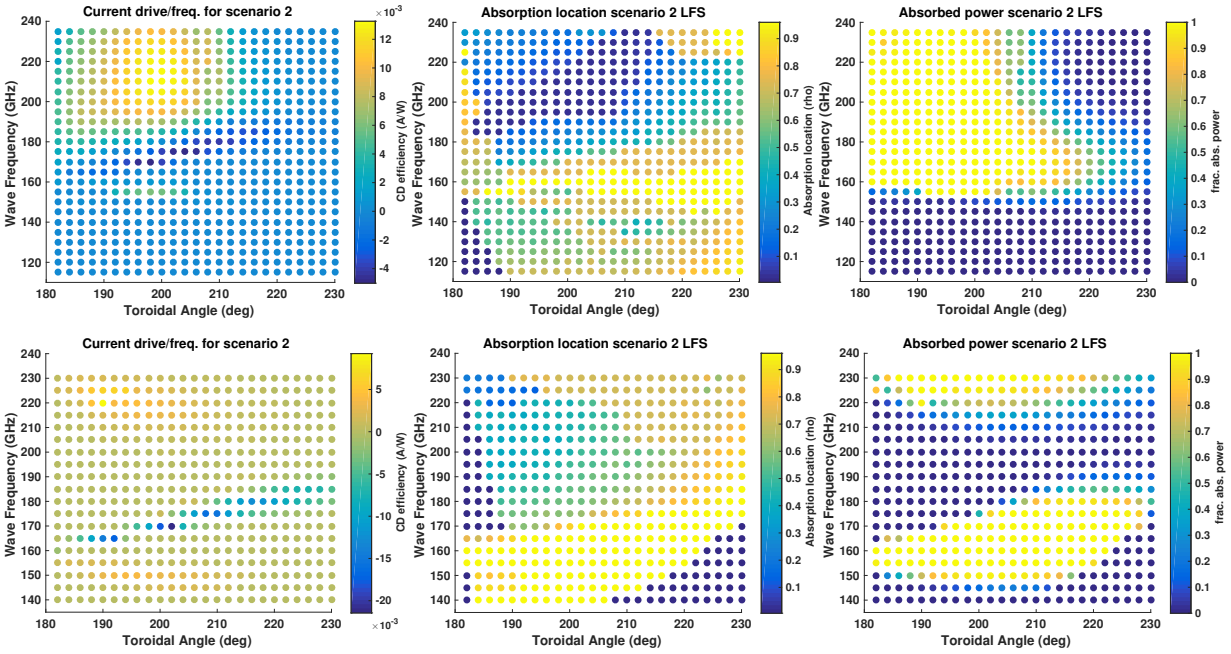

Figure 4.8: O-mode (top) and X-mode (bottom) LFS frequency scan for scenario 2, showing the current-drive efficiency, absorption location and absorbed power fraction calculated with a cold propagation dispersion relation with GENRAY, and absorption and current-drive by CQL3D.

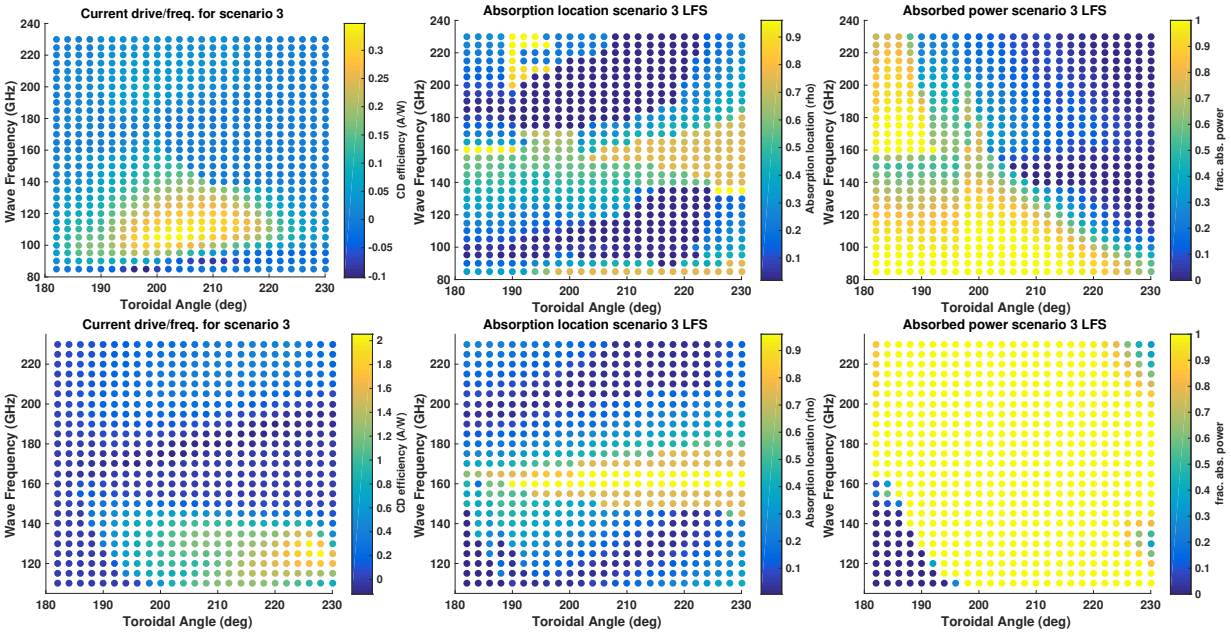

Figure 4.9: O-mode (top) and X-mode (bottom) LFS frequency scan for scenario 3, showing the current-drive efficiency, absorption location and absorbed power fraction calculated with a cold propagation dispersion relation with GENRAY, and absorption and current-drive by CQL3D.

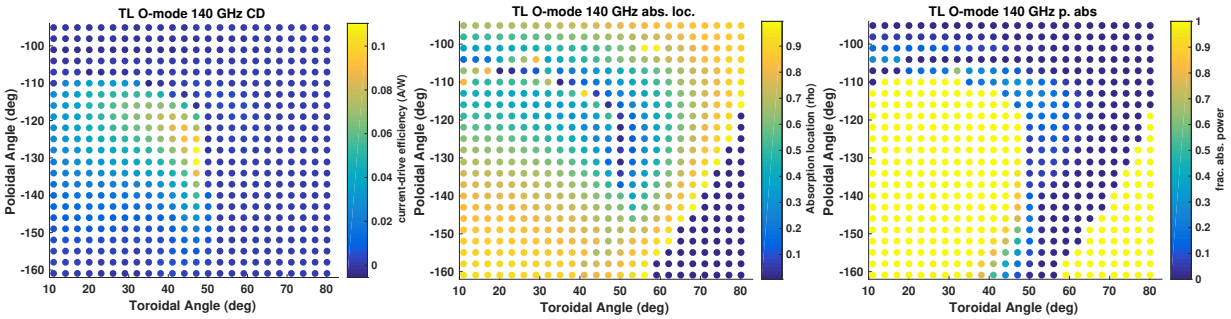

(a) Current drive efficiency (b) Absorption location (c) Absorbed power

Figure 4.10: 140 GHz O-mode top launch scan for a launcher at R = 1.8 m in scenario 1, calculated with the GENRAY cold dispersion relation, Mazzucato absorption and Lin Liu current-drive calculation with momentum conservation.

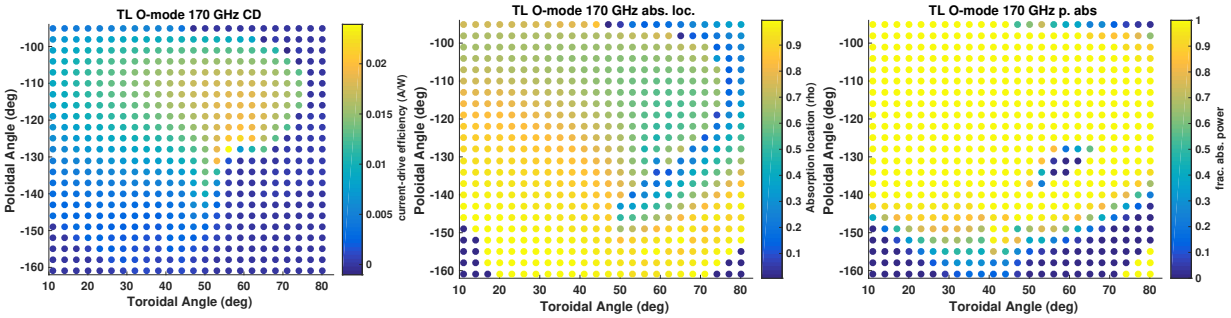

(a) Current drive efficiency (b) Absorption location (c) Absorbed power

Figure 4.11: 170 GHz O-mode top launch scan for scenario 2, calculated with the GENRAY cold dispersion relation, Mazzucato absorption and Lin Liu current-drive calculation with momentum conservation.

electrons cause the absorption, so that seems sensible. This fact does highlight the necessity of having real-time control of the top-launcher.
The top launch scan for 170 GHz O-mode in scenario 2 has a maximum current-drive of 0.02 A/W. It shows similar features as the one for scenario 1. However, the fraction of absorbed power *seems* to fall of less steeply after maximum current-drive. This is, however, not entirely true, as what happens is that the wave travels pas the resonance and is absorbed at a later point, where the lack of directionality causes it to drive no current but to still have a high fraction of absorbed power.

The top launch scan for scenario 3 in Figure 4.12, gives a maximum current-drive of 0.45 A/W. This is a higher efficiency than in the LFS O-mode scenario. In this scenario, the fraction of absorbed power is lower, due to a low density and therefore low(er) absorption coefficient.

The first harmonic O-mode has the highest current-drive efficiency for the top launch configurations, and for most of the LFS configurations. The reason for this, is that the second harmonic X-mode launches are interfered with by the down-shifted third harmonic. This is the downside of a compact machine, that the higher harmonics are very close to each other. For all investigated frequencies for the top launcher except the ones that are in cut-off, there are possibilities for complete absorption of power.

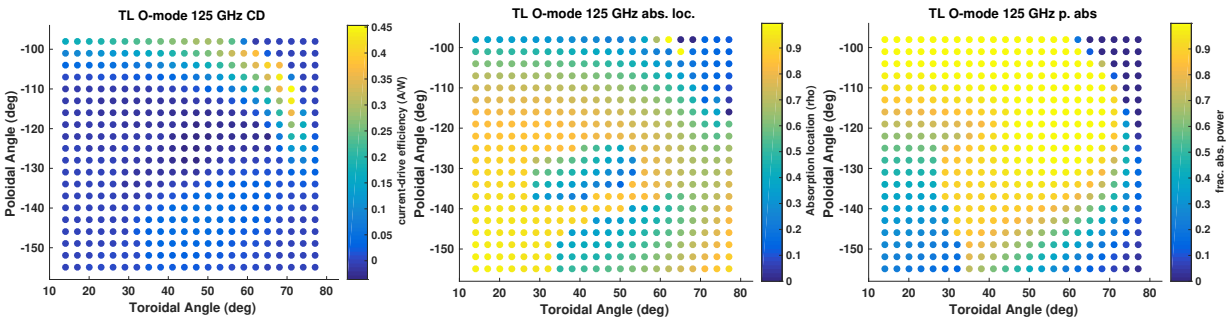

(a) Current drive efficiency (b) Absorption location (c) Absorbed power

Figure 4.12: 125 GHz O-mode top launch scan for scenario 3, calculated with the GENRAY cold dispersion relation, Mazzucato absorption and Lin Liu current-drive calculation with momentum conservation.

4.3 Scenarios and dispersion relation analysis

In this section, the specific cases with the highest current-drive for each scenario are assessed in more detail to verify and understand the results and to provide a probability estimate for the current drive efficiency. For each scenario, as given in Figure 4.1, the top launch and LFS launch cases (parameter combinations) with the highest current drive efficiency are investigated. To provide a more physical picture than in the parameter scans, different dispersion relations are used, the power input into CQL3D is changed to observe non-linear effects and in each case a Gaussian beam is approximated by 51 rays.

For each case, the absorbed power and current drive in terms of $dP/d\rho$ and $dA/d\rho$ are shown, which are the absorbed power density on a flux surface multiplied by is volume, and the current-drive density in A/cm^2 multiplied by the surface are of the flux surface, so this shows the absorbed power and current-drive at each 0.01ρ. Here, ρ is the radial coordinate that signifies the normalised flux surface.

The dispersion and absorption relations that are considered are shown in Table 4.1.

Label	Dispersion relation	Resonance	Absorption	ECCD	Input power (MW)
1	Cold	Relativistic	Relativistic	Lin Liu	(n.r.)
2	Relativistic	Relativistic	Mazzucato	Lin Liu	(n.r.)
3	Hot	non -relativistic	Hot	Lin Liu	(n.r.)
4	Relativistic Westerhof	Relativistic	Mazzucato	Lin Liu	(n.r.)
5	Hot Westerhof	non -relativistic	Hot	Lin Liu	(n.r.)
6	Cold	Relativistic	Mazzucato	Lin Liu	(n.r.)
7	Cold	Relativistic	Fokker-Planck	Fokker-Planck	0.1
8	Cold	Relativistic	Fokker-Planck	Fokker-Planck	1
9	Cold	Relativistic	Fokker-Planck	Fokker-Planck	10
10	Cold	Relativistic	Fokker-Planck	Fokker-Planck	100

Table 4.1: Table with the choices in dispersion, resonances, absorption, ECCD calculation and input powers used in computing the absorption and current drive profiles in the different scenarios. As GENRAY is linear code, the input powers are marked as (n.r.) or not relevant here.

Scenario 1: Design point

Scenario 1 is the design point scenario. This scenario is where the value of 0.15 A/W is the goal in terms of current drive. For this design point scenario, the highest current-drive was found with the 140 GHz top launcher. First, the importance of the toroidal location of the launcher and the general mechanism of current-drive will be investigated. Then, the different dispersion relations will be applied to the cases with the highest current-drive.

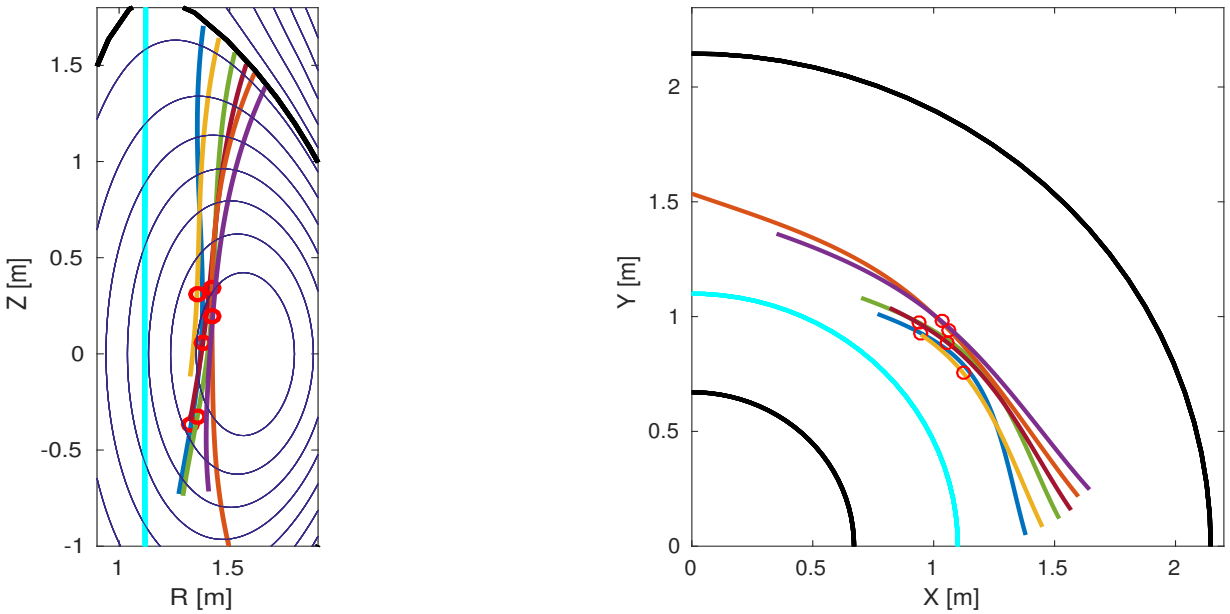

Figure 4.13: Poloidal (left) and toroidal (right) view of the rays for the cases with the highest current drive for every considered 140 GHz top launcher. The darker blue lines represent the flux surfaces. The cyan line indicates the location of the cyclotron resonance, and the red circles are the location where the current is deposited. The waves are absorbed away from the resonance due to the Doppler shift in the resonance. Each ray corresponds to a launcher with a different location on the toroidal radius. Going from blue at R=1.4 to purple on R=1.9. The rays 'start' at the moment they reach the plasma boundary. So the waves that are plotted begin at the last closed flux surface.

For a top launcher with 140 GHz O-mode launch, varying the toroidal location of the launcher from R=1.4 m to R = 1.9 m in steps of 0.1m has some effect on the current-drive, but the resulting current-drive is within a 5% range. In Figure 4.13, the poloidal and toroidal trajectory for the cases with the highest current-drive for each launcher are shown, the point where most of the power is absorbed is given by a red circle. The cases with the highest current-drive efficiency have absorption that is localized at a similar location in the poloidal view. The current that is driven here is driven by the Fisch-Boozer mechanism. This is a location where the waves travel parallel to the resonance at a distance from it. At this location, the waves are absorbed by the electrons with high parallel velocity that are Doppler-shifted to fulfill the resonance condition. Because they have a high parallel velocity, the added perpendicular momentum efficiently causes these electrons to lose collisionality and thus drive a current.

Of these different top launcher cases, the case with the highest current drive has a launcher located at $R = 1.8$ m, with toroidal angle of 44 degrees and a poloidal angle of -131 degrees. For the LFS launcher, the launcher with the highest current drive corresponded to a 112 GHz equatorial launcher with a toroidal angle of 204 degrees.

The dispersion relations and input powers for these cases were varied to investigate the effect that different corrections and calculations can have on the magnitude and deposition location of the power and current drive. The different absorption and current drive profiles are shown in Figures 4.14 and 4.15.

Disp/abs	1	2	3	4	5	6	7	8	9	10
CD. eff (A/W)	0.88	0.072	0.092	0.071	0.094	0.085	0.109	0.11	0.109	0.107
CD. eff mom. cons.	0.95	0.89	0.79	0.103	0.78	0.105	”	”	”	”
frac. abs. power	1	1	1	1	1	1	0.925	0.924	0.917	0.897

Table 4.2: Current drive of different dispersion/absorption relations in the TL case for scenario 1.

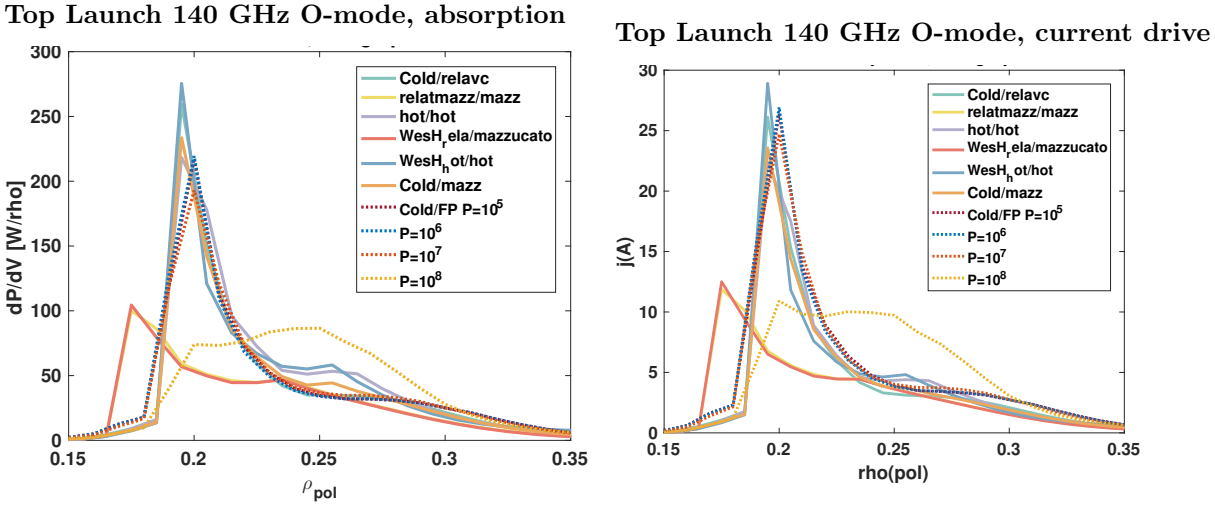

Figure 4.14: Absorption (left) and current-drive (right) profiles with different dispersion relations and launched powers using GENRAY (solid) and CQL3D (dotted) lines for the top case identified in the parameter scan. All results are divided by their input power and multiplied by 1000 to be able to compare them.

Most dispersion/absorption combinations give similar results in the top launch case of Figure 4.14, the Westerhof and Mazzucato relativistic dispersion relation cases however, show different behaviour with a different peak in absorption and current-drive than the others in the top launch case and lower current-drive overall. CQL3D (7-10) predicts a higher driven current in all cases, but also a lower fraction of absorbed power.

Disp/abs	1	2	3	4	5	6	7	8	9	10
CD. eff (A/W)	0.088	0.079	0.081	0.075	0.073	0.079	0.105	0.106	0.106	0.088
CD. eff mom. cons.	0.105	0.106	0.106	0.097	0.095	0.106	”	”	”	”
frac. abs.	1	1	1	1	1	1	0.996	0.996	0.992	0.922

Table 4.3: Current drive of different dispersion/absorption relations in the LFS case for scenario 1.

In the LFS launch case, the differences between GENRAY and CQL3D when not considering momentum conservation, are of the order of $15-35\%$ in terms of driven current depending on the dispersion and abosrption relation. However, when momentum conservation *is* considered, this difference becomes smaller: $0-13\%$. The results of the different dispersion relations in GENRAY give a current-drive between 0.073 - 0.088, but this difference changes to 0.095 - 0.106 when the Lin Liu momentum conservation operator is taken into account.

The non-linear effects are clearly visible in both figures, with the 100 MW beam's absorption being more spread-out than the lower powers, and the current-drive efficiency first increasing slightly (with 10 MW) and then decreasing (with 100 MW) in Figure 4.15. This can be explained by referring to section 2.9, first, the current-drive efficiency goes up due to more high-energy electrons being present. When the power increases after this point, the relativistic mass increase will decrease the momentum of the heated particles more than the collisionality decreases. Thereby decreasing the driven current.

These results show that a current-drive of 0.11 A/W is possible with a top launcher of 140 GHz as calculated with CQL3D and that a comparable current of 0.106 A/W can be driven from the low-field-side with a 112 GHz launcher. It appears that the use of different dispersion relations has a larger effect on the calculated current-drive in the top launch than in the low-field-side launch configuration. This is likely due to the larger effect of the corrections in the dispersion relations when travelling parallel to a resonance.

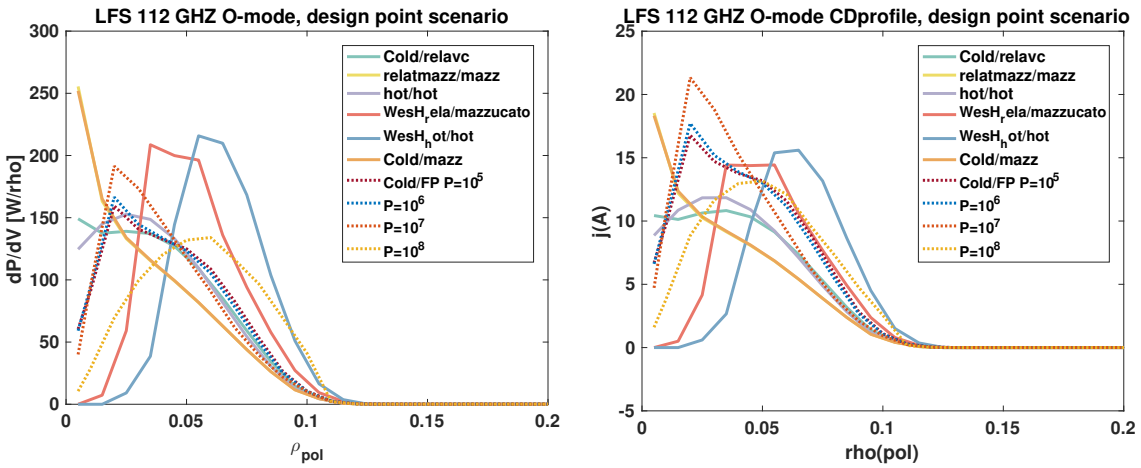

Figure 4.15: Absorption (left) and current-drive (right) profiles with different dispersion relations and launched powers using GENRAY (solid) and CQL3D (dotted) lines for the LFS top case identified in the parameter scan. All results are divided by their input power and multiplied by 1000.

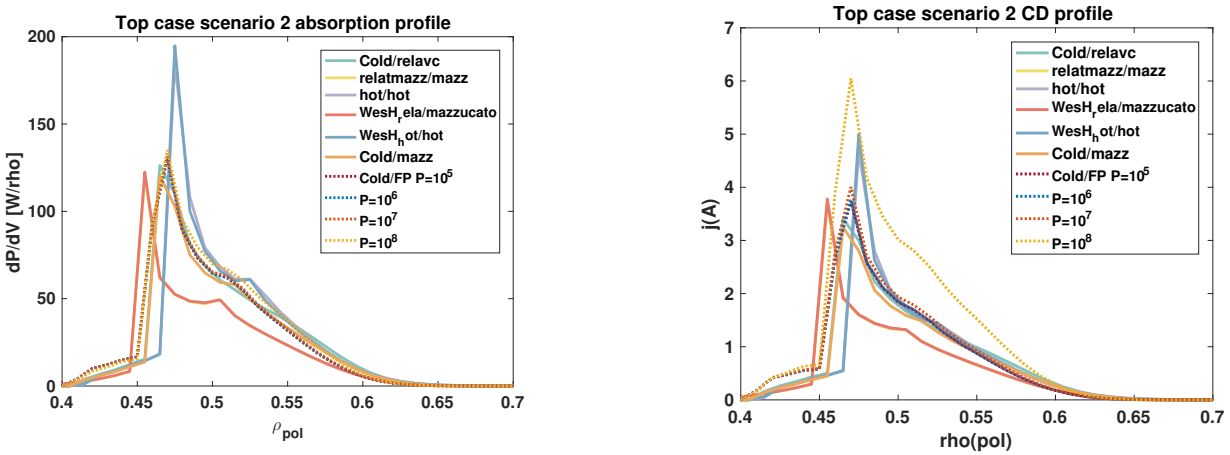

Figure 4.16: Absorption (left) and current-drive (right) profiles with different dispersion relations and launched powers using GENRAY (solid) and CQL3D (dotted) lines for the top case of 170 GHz O-mode identified in the parameter scan.

Scenario 2: high density

The high density scenario is a scenario that is taken into account to investigate the effect of higher density on accessibility and the current-drive performance. The wave accessbility in the high density scenario is shown in Figure 2.8. The central plasma frequency (O-mode cut-off) is 155.5 GHz, and the X-mode cut-off at the magnetic axis is 221 GHz meaning that waves below these values will not be able to reach the centre of the machine.

The cases with the highest current-drive that are investigated are the following. For the top-launcher, the highest current-drive was obtained in the case with a 170 GHz O-mode launcher at R = 1.4 m, a toroidal angle of 56 degrees and a poloidal angle of −128 degrees. The LFS launcher is a 170 GHz X-mode launcher with a toroidal angle of 202 degrees. Figures 4.16 and 4.17 show the absorption and current-drive profiles of these two cases.

Absorption in the top launch case of Figure 4.16 is located on the High Field Side (HFS) of the machine, which is why there is no detrimental trapping effect on the Fisch-Boozer current-drive. An effect that is noted in the top launch case, is the magnitude of the difference in current-drive efficiency at (very) high

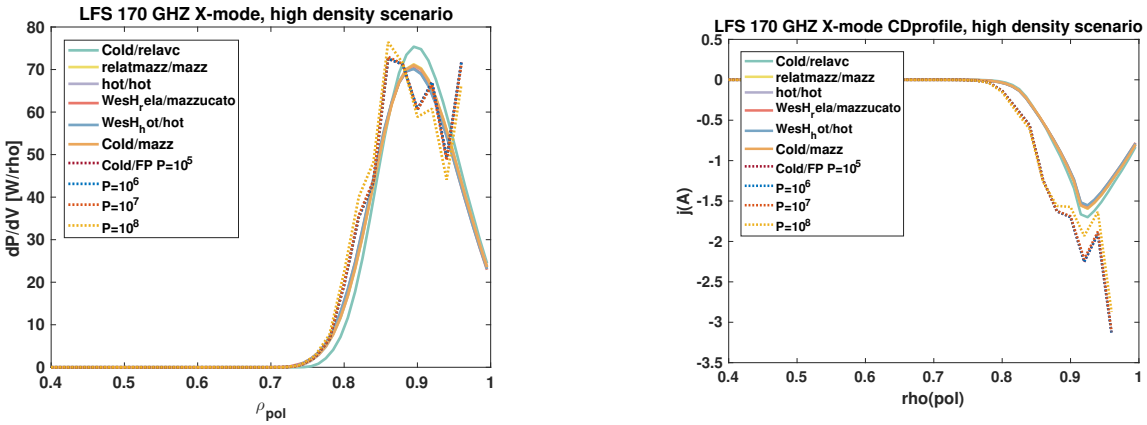

Figure 4.17: Absorption (left) and current-drive (right) profiles with different dispersion relations and launched powers using GENRAY (solid) and CQL3D (dotted) lines for the LFS top case identified in the parameter scan. A correction was made to account for the difference in mesh at this location between CQL3D and GENRAY.

power levels. The 100 MW case has a significantly higher current-drive efficiency than the cases with lower powers.

In the LFS case of Figure 4.17, the dominant current-drive mechanism is the Ohkawa mechanism. This is visible for instance by the change in direction of the driven current and that the current is driven at high values of rho, near the edge of the machine on the LFS where the fraction of trapped particles is high. The current-drive is negative here. Similar to what was seen earlier in 4.4, CQL3D calculates a higher current-drive in the Ohkawa mechanism than GENRAY. Note that in the edge region CQL3D has averaged the flux surface from $\rho = 0.95 - 1$, this flux surface now has a larger volume and surface, which is why there is such a large peak at the end of the curve.

In both figures, the driven current and absorbed power fraction was similar for all the considered runs in these scenarios. What stands out is the magnitude of the quasi-linear effect in the TL scenario in Figure 4.16 for 100 MW. This causes a $\sim$ 40 % increase in the driven current. This is different than the result for scenario 1. This probably has to do with the fact that there is a higher electron density, which also have a lower temperature to start with in scenario 2. This means that there is less power per electron *and* that the starting energy of electrons is also lower so the relativistic mass increase hass less impact on the driven current.

Scenario 3: low density/ramp-up

Scenario three is the low density scenario. This scenario is meant to simulate ramp-up conditions where the current is in the process of ramping up. In this scenario, some differences between the dispersion relations and especially between the injected powers is expected. The density of $10^{19}/\mathrm{m}^3$ is relatively low, which means that absorption might not always be complete. Furthermore, non-linear effects are expected to be more prominent since the density is lower and the criterion for non-linearity scales as $1/n_\mathrm{e}$ (Equation 2.36).

The cases that are plotted are the following. For the top launcher plotted in Figure 4.18, the case with the highest current-drive efficiency was the 125 GHz case with a toroidal angle of 65 degrees, and a poloidal angle of -107 degrees.

For the LFS launcher plotted in Figures 4.19, the case with the highest current-drive efficiency was the first harmonic X- mode launch of 125 GHz waves. Since this launch is considered to have a large associated risk of cut-off, here, the 112 GHz O-mode case is shown with a toroidal angle of 204 degrees.

The second power absorption peak observed in Figure 4.19 around rho(pol)=0.23 is due to the wave not

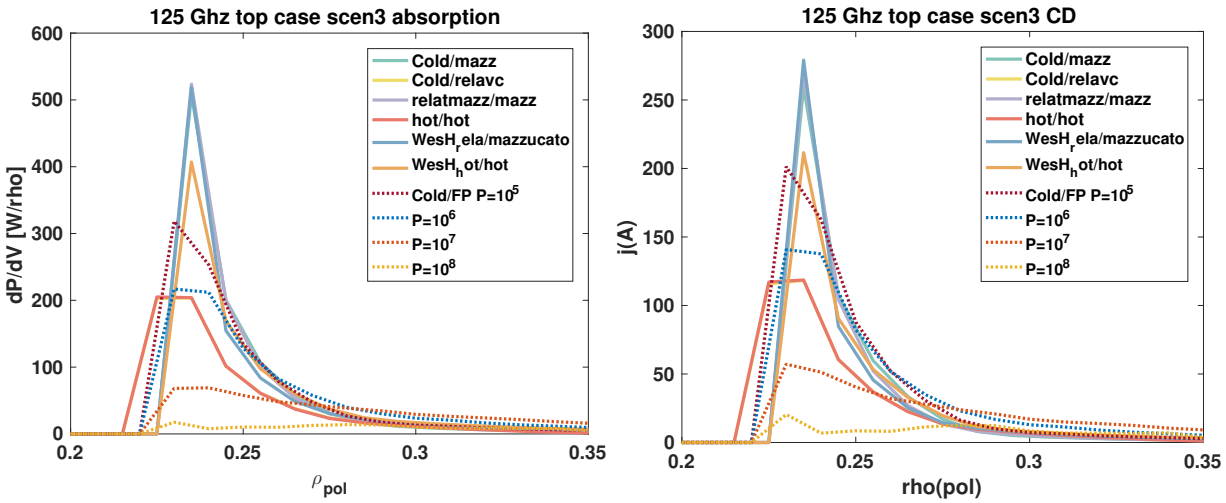

Figure 4.18: Absorption (left) and current-drive (right) profiles with different dispersion relations and launched powers using GENRAY (solid) and CQL3D (dotted) lines for case of 125 GHz O-mode identified in the parameter scan.

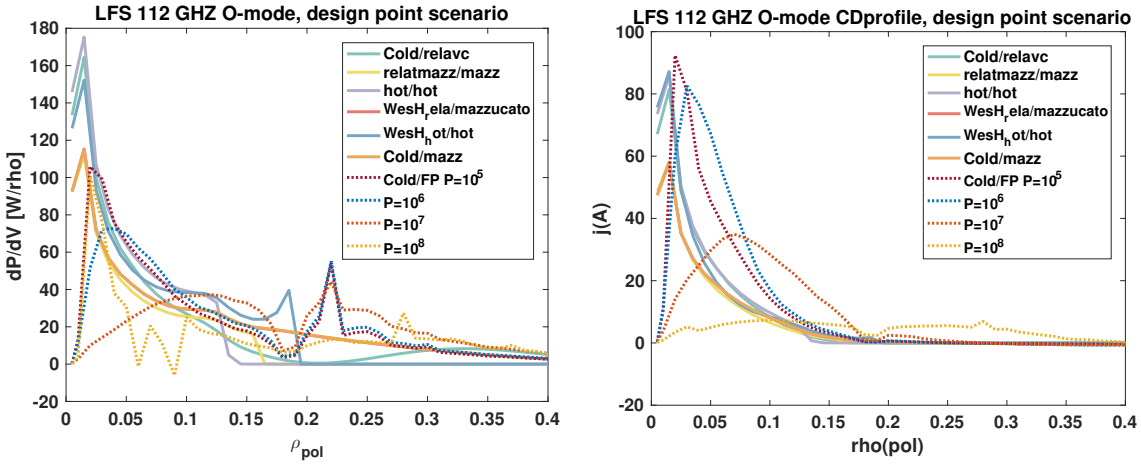

Figure 4.19: Absorption (left) and current-drive (right) profiles with different dispersion relations and launched powers using GENRAY (solid) and CQL3D (dotted) lines for the 112 GHz LFS case identified in the parameter scan.

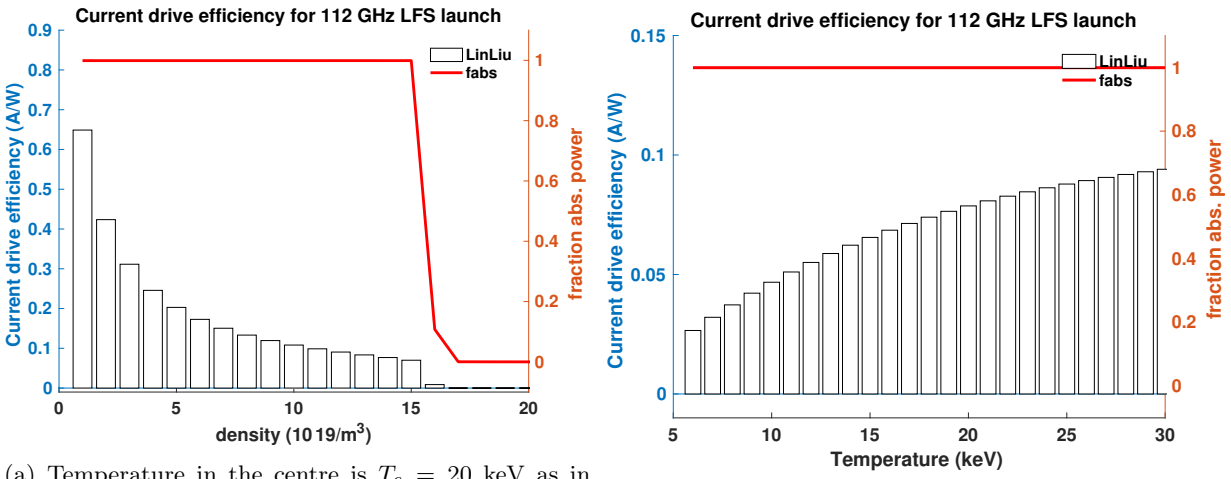

(a) Temperature in the centre is $T_e = 20$ keV as in design point scenario. The cut-off density for 112 GHz launch is $15.6 \cdot 10^{19}/\mathrm{m}^3$.

(b) Density in the centre is $n_e = 13.7 \cdot 10^{19}/\mathrm{m}^3$ as in design point scenario.

Figure 4.20: LFS density and temperature scan.

being fully absorbed in the first pass and travelling through the resonance again at the other side of the machine.

Note that these launchers with the highest current drive efficiency in scenario 3 have the same frequency as the ones in scenario 1. However, the absorption location and the angles for the optimal cases is different for both scenarios. Especially the top launcher has a different absorption location. This is due to the lower absorption coefficients for lower temperatures and densities. It is clearly visible that increasing the input powers leads to lower power absorption and current-drive.

4.4 Scaling with temperature and density

This section investigates the scaling of the current-drive efficiency with density and temperature. These results are interesting to inform the design process of ST-F1.

A scan over density, and a scan over temperature is performed for a TL (Figure 4.21) and a LFS launcher (Figure 4.20). The launcher locations are chosen to be the same as the high current-drive cases in scenario 1 in section 4.3. The scaling of the high current-drive cases for LFS and TL with temperature and density is shown here for the launcher configurations as given in scenario 1.

From these figures, it is clear that the current-drive efficiency is dependent on the temperature and density. The general trend is upwards for increasing temperature and downwards for increasing density. This trend is of course expected as with Equation 2.33, but the second derivative decreases. This makes sense for the n_e part as the general scaling goes as $1/n_e$, but for the temperature part one should also account for the change in the Doppler shift with temperature as the temperature increases the parallel velocity distribution. That means that the actual maximum achievable current-drive is likely somewhat higher than shown here in the temperature plots.

4.5 Current-drive as a function of absorption location

This section shows the relation between the power absorption location and the current-drive efficiency. Being able to drive a current on specific locations in the plasma, is important for purposes of tailoring the magnetic profile and suppression of MHD instabilities. This is especially true for ST-F1, where $\sim 70\%$ of the current is bootstrap current and at least difficult to control.

For multiple current-drive scenarios, the identified regions where the most power is absorbed are mapped

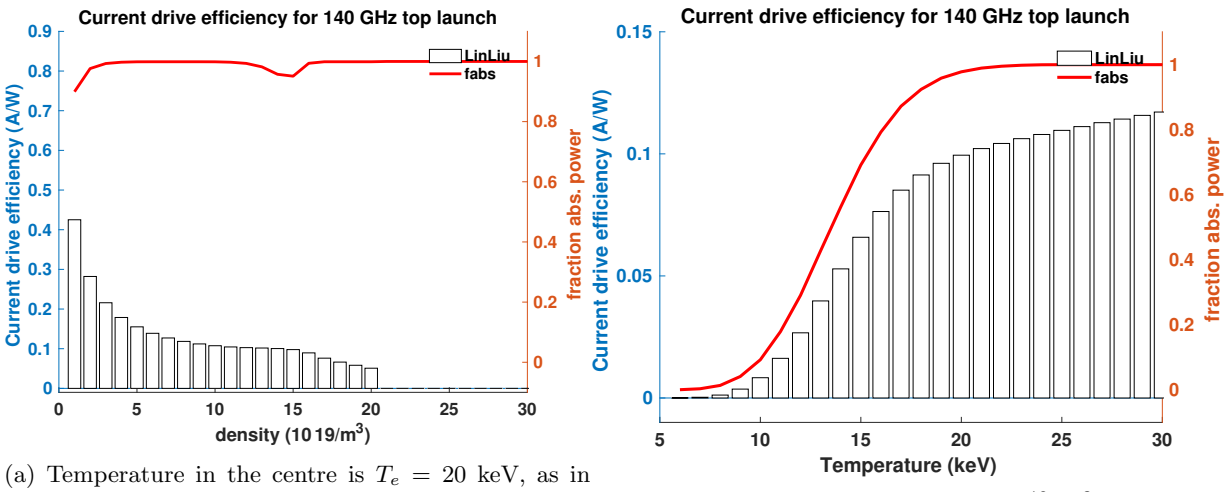

(a) Temperature in the centre is $T_e = 20$ keV, as in design point scenario. The cut-off density for 140 GHz launch is $24 \cdot 10^{19}/\mathrm{m}^3$.

(b) Density in the centre is $n_e = 13.7 \cdot 10^{19}/\mathrm{m}^3$ as in design point scenario.

Figure 4.21: Top launch density and temperature scan. At above the cut-off density for the 140 GHz top launch scenario, something interesting happens, the wave is actually in cut-off and reflected *into* the resonance, causing complete absorption again but no current-drive.

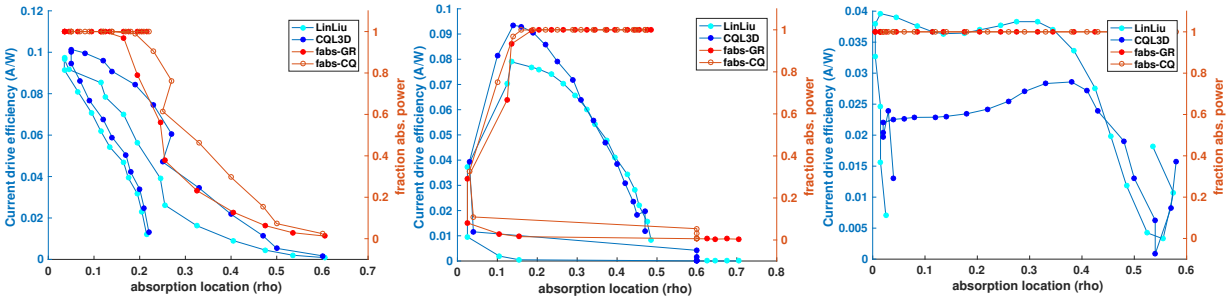

Figure 4.22: Current drive efficiency and fraction of power absorbed calculated with GENRAY and CQL3D against maximum absorption location for LFS launch with varying toroidal angles with 112GHz (left) and 140GHz (middle) O-mode launch and 200 GHz X-mode launch (right).

and are plotted against the driven current and fraction of absorbed power. Four LFS frequencies are considered and three TL frequencies. The expectation is that for ECCD, the absorption and current drive go up with more centralised deposition due to the increase in temperature there.

The cases that are taken into account are, LFS: all in scenario 1, 112 GHz O-mode, 140 GHz O-mode, 224 GHz O-mode, and 200 GHz X-mode. And for the TL: in scenario 1: 140 GHz O-mode, 170 GHz O-mode and in scenario 2: 170 GHz O-mode. Figure 4.22 shows the absorption location plotted against the current drive efficiency and fraction of absorbed power for the LFS cases. Then, Figure 4.23 shows the current-drive efficiency against the absorption location for the top launch scenarios.
From these figures it becomes apparent that the current-drive efficiency is strongly dependent on the absorption location. However, for the purposes of driving current in specific parts of the plasma, it seems like there is a reasonable option to use different frequency launchers to continuously drive current in regions of choice.

One can identify two effects, the choice of the optimal doppler shift and the centralisation of the current-drive. The angle at which the waves reaches the resonance and 'chooses' the directionality of the electrons to heat and the temperature at the location of absorption. Next to that, as visible in the 140 GHz plot in Figure 4.22, the wave can start to miss the resonance and thus not completely absorb.

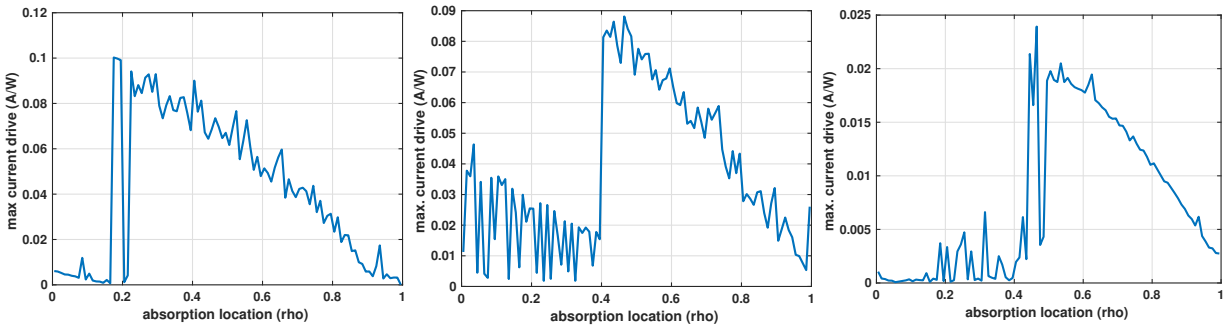

Figure 4.23: Current drive efficiency against maximum absorption location for top launch for all cases for (left) scenario 1 140 GHz O-mode and (middle) scenario 1 170 GHz O-mode launch and (right) scenario 2 170 GHz O-mode launch.

4.6 Low field side launch polarisation

In this section, the challenge that comes with the large shift in polarisation on the LFS when the magnetic field tilt changes is addressed. As the polarisation is determined with respect to the magnetic field, a change in the gradient (tilt) of the magnetic field can induce a change to the wave polarisation. For example, in fundamental O-mode launch, if the tilt changes and a part of the beam becomes X-mode, this part can be completely reflected to the launcher due to the fast X-mode cutoff.

The benefit of the LFS mode is that its launcher is simpler and (thus) easier to control. It would for instance only need steering the toroidal angle, with the optimal angle less sensitive to plasma conditions as the wave always travels through the resonance. Furthermore, the steering necessary for optimal current-drive has a maximum of a few degrees for optima current-drive.

Here, specific frequency scans are presented for the design point scenario, where the X-mode is not in cut-off and both modes drive a current in the same direction. One of these, is the 200 GHz LFS launcher, with the O-and X-mode current-drive and power absorption dependence on toroidal angle is shown in Figure 4.24.

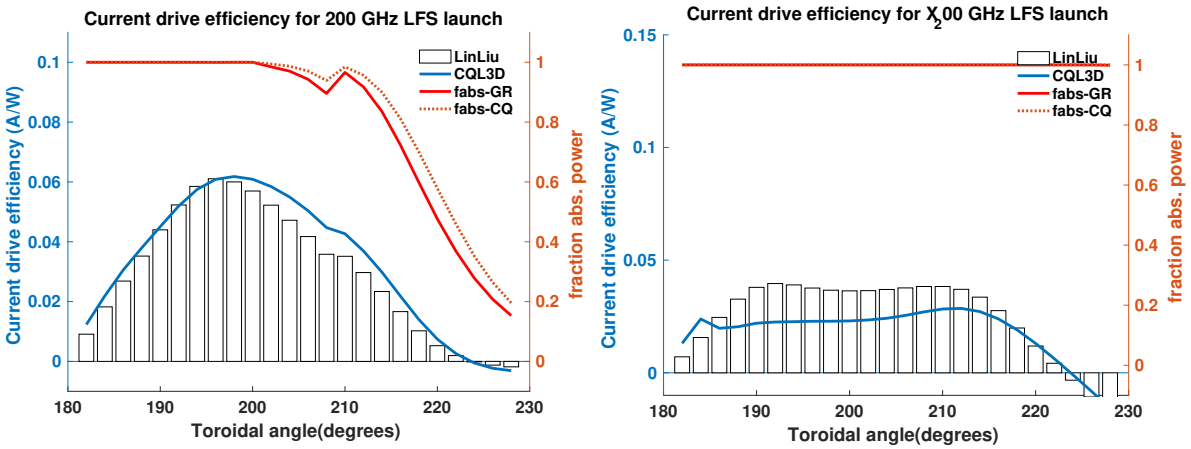

(a) O-mode.

(b) X-mode.

Figure 4.24: O-and X-mode current-drive efficiency and power absorption plots for the 200 GHz LFS launcher.

The absorption location and current-drive efficiency plots for both O- and X-mode launch are shown in Figure 4.24. A wave could be produced that is completely absorbed for both O and X mode and drive

a substantial current for both modes at multiple toroidal angles. The combination of these two modes would lead to a superposition of the O- and X-mode current drive and absorption. This would lead to two peaks in power absorption and current-drive. The difference in the calculation of current-drive in the X-mode scenario is due to the fact that CQL3D calculates more down-shifted absorption from the third harmonic resonance.

Chapter 5

Discussion

The efficient operation and the degree of control of a spherical tokamak are dependent on the availability of efficient current-drive and heating at multiple locations in the plasma. This research has aimed to find the potential of an Electron Cyclotron Heating and Current-drive system for the ST-F1 spherical tokamak that is being developed by Tokamak Energy in this respect. This chapter highlights the most important findings and discusses their relation with the research question and the implications for the design and operation of the ST-F1 tokamak and the wider research field.

5.1 Current drive efficiency

The maximum value of current-drive efficiency for the design-point that is found in this work, is 0.11 A/W. This value has been obtained for low field side and top launcher configurations. This value is lower than the current-drive efficiency assumed in the design of ST-F1. This means that, if only ECCD is used to drive the bulk plasma current in the design point scenario, the energy necessary to sustain the plasma current will be 36% higher than expected. For the goal of achieving an energy gain of $Q_{\text{fusion}} > 1$, this does not have to be a problem. The amount of injected power necessary to sustain the part of the plasma current that has to be driven by non-inductive means ($1.5MA$) would then be $\frac{1.5\text{MA}}{0.11\text{A/W}} = 13.6\text{MW}$ and assuming a P_{fusion} of 30 MW would lead to $Q_{\text{fusion}} = \frac{30}{13.6} = 2.2$. Still an achievement that has not been demonstrated on any fusion device yet.

Findings in other spherical tokamaks are mostly incomparable to the findings in this research, because most other spherical tokamaks operate in an overdense configuration. The first electron cyclotron harmonics are not reachable in those devices. It is more instructive to compare these results to conventional tokamak devices, which are similar in magnetic field, temperature and density to the planned operation of ST-F1. This can best be done by considering the dimensionless current-drive efficiencies. There are two notable dimensionless current drive efficiency metrics. The first has a dependency on temperature, [58]:

$$\zeta_{ec} = \frac{32.7 I_p(\text{A}) R(\text{m}) n_e \left(10^{20}\ \text{m}^{-3}\right)}{T_e(\text{keV}) P(\text{W})}. \tag{5.1}$$

The second dimensionless current drive efficiency is not normalised to temperature. The temperature dependence is contained in the attainable current drive:

$$\gamma_{\text{CD}} = \frac{I_p(\text{A}) R(\text{m}) n_e \left(10^{20}\ \text{m}^{-3}\right)}{P(\text{W})}. \tag{5.2}$$

For the case with the highest current-drive efficiency $\zeta_{ec} = 0.345$ and $\gamma_{\text{CD}} = 0.21$ in this work. With typical values of ζ_{ec} ranging from 0.2-0.3 for ECCD [20]. This value of dimensionless ECCD current drive efficiency is in good agreement with work on ITER with the maximum ζ_{ec} at $0.25-0.3$ [59] and $\gamma_{CD} = 0.2$, DIII-D with ζ_{ec} at $0.25 - 0.35$, and DEMO with ζ_{ec} at $0.25 - 0.3$ and $\gamma_{CD} = 0.35 - 0.45$ depending on the scenario [20]. This high value of γ_{CD} for DEMO can be explained by the high central temperature of $53 - 65$ keV, so this value also extrapolates well to the findings in this study.

Two types of uncertainties are identified for the current-drive results in this thesis. Firstly, in this study, an error margin in calculation of current-drive and absorption between codes is implicit. The code-to-code difference between CQL3D and other Fokker-Planck codes quoted in the manual to be up to 4% [51]. A benchmarking study for a case ITER however, shows a case where the Fokker-Planck code BANDIT-3D predicted 20% more driven current than CQL3D when both using ray-tracing, cold dispersion relations, relativistic resonances and Fokker-Planck absorption and current-drive [48]. In the same case, a difference of up to 10% was noted between FP codes OGRAY and CQL3D, with the difference that OGRAY had a beam propagation model instead of a ray. And these differences are only for one case in ITER, the differences could very well be larger in other cases. This indicates that the Fokker-Planck code-to-code difference in the calculation of current-drive can be up to 20% or might even be larger. That same study shows differences between linear codes such as GENRAY (like GRAY, TORAY, TORBEAM) of up to 10%. The second type of uncertainty that is identified falls in the category of known unknowns, and has to do with the design of ST-F1. In the treatment of this thesis, one magnetic equilibrium is used that probably does not fit the final design of ST-F1. All the results in this thesis will likely change due to choices made in the design phase. If the device were to turn out larger than expected or to have a magnetic field $B \neq 4$ T, that would lead to the necessity of recalculating the findings. Nevertheless, this project does give the insight that the dimensionless current-drive efficiency is similar to that found in other devices.

Although the difference between codes is potentially quite large $\approx 20\%$, the conclusions of this research would not change drastically by a deviation up-or downward of this magnitude. Confidence is gained in the results because they agree with existing studies on ECCD efficiency in tokamaks. The findings did give an estimate that was $\approx 10\%$ higher in dimensionless current-drive efficiency than in other studies, so the results may deviate from experiment in this range.

At the beginning of the project, a study of the grid convergence of CQL3D and GENRAY was done. This showed that the predicted current-drive did not change with increasing grid density anymore for the value of 100 grid points for GENRAY and the employed grid of 84 points for CQL3D. These were therefore used throughout the process. Upon closer inspection at the end of the project, the absorption and current-drive profiles do seem to lack some resolution (as visible in some figures in Section 4.3). The results for that section were re-run again for double grid density, the resolution improved but the predicted current-drive changed by less than 1%. The overall presented results are therefore considered not to be affected by a grid density that is too low.

5.2 On the scaling of the current-drive efficiency with temperature and density

Taking into account the scaling of the current-drive efficiency with temperature and density can be important for reaching the highest possible Q_{fusion}. This research identified the scaling of the ECCD current-drive efficiency with temperature and density for the top launch and low field side cases with the highest current drive in the design point. The findings agree well with the theoretical scaling of of $\propto \frac{Te}{ne \ln \lambda}$ with $\ln \lambda$ in [46]. These scalings might re-inform the design point to be pushed to higher T_e and lower n_e to obtain energy-optimal operation. It must be noted that the CD efficiency is not the only variable at hand in this case. Changing the kinetic profiles might well have an effect on the bootstrap fraction f_{bs} and the fusion power as well.

5.3 Localisation of current drive

The ability to drive a plasma current at specific locations and on specific flux surfaces, is an important task in the operation and control of a (spherical) tokamak. The 'tailoring' of the profile of the driven current in this way is necessary for a variety of reasons ranging from discharge optimisation to active control of MHD instabilities. This work has found that a current can be driven on each flux surface. As expected, the efficiency of the driven current with the Fisch-Boozer mechanism decreases when its driven farther away from the plasma centre, due to the higher temperature and more efficient absorption there. This means that, when applying ECCD for controlling MHD instabilities, this can also help drive a part of the plasma current. This work also finds that there are options for Ohkawa current-drive in the edges

of the plasma, and that the current-drive efficiency of this mechanism is higher in the edges than the Fisch-Boozer efficiency. This option is discussed more in detail in a following section. In both cases, the current-drive efficiency near the edge is several times lower than 0.11 A/W. If there turns out to be a large need for current-drive at locations far from the center, the overall current drive efficiency with ECCD will turn out to be lower than 0.11 A/W.

The results also indicate that the top launcher is probably a better option to drive current at a flux surface of choice. The top launcher configuration is evidenced to have more flexibility to drive current at different absorption locations. This is because the waves launched from the top have the ability to travel through the resonance for a longer time and they can impact on the higher energy tail of the electron population. To have this flexibility in absorption but maintain high current drive efficiencies, the top launcher needs to have active steering of the poloidal and toroidal angles.

Power and current deposition width

In this study, deposition profiles were found where a large fraction of the power was deposited in a narrow region of $\delta\rho < 0.05$. This narrow deposition profile would generally be good for suppression and active control of MHD instabilities. For suppression of these instabilities, the absorption width must be narrower than the critical island width. The figure of merit for suppression scales inversely with current-drive width $1/w_{cd}$ [60]. The deposition width is found in several studies to be broadened relative to the ray-tracing deposition width. The deposition width is sometimes found to be several times higher than expected. EC deposition broadening is found in multiple devices like the DIII-D tokamak [61], ASDEX upgrade [62], the TCV tokamak [19] and it is also theorised to occur on ITER [63]. This phenomenon could be explained by electron density fluctuations or (anomalous) transport, but this process is not completely understood yet. What it does indicate, is that ray-tracing calculations and deposition power profiles obtained numerically should be interpreted with this fact in mind. However, none of the factors potentially causing EC deposition broadening are taken into account in this study, indicating that the actual deposition width is probably broader than calculated in this study.

5.4 Ohkawa current-drive

For specific cases, the Ohkawa current was shown to have a current-drive efficiency of the same order as the Fisch-Boozer mechanism for this high field spherical tokamak. The Ohkawa current-drive mechanism has a higher current-drive efficiency in the edges of the plasma. This might be very interesting for purposes of driving off-axis current. This result is also in line with earlier findings of [24] that the Ohkawa current drive can have similar current-drive to the FB mechanism in low aspect ratio tokamaks with high β_e. This research finds agreement with the findings that current drive with the Ohkawa mechanism can be of the same order as the Fisch-Boozer mechanism for low aspect ratio tokamaks that were found in [24].

The Ohkawa mechanism has major uncertainties. Steady state current-drive with this mechanism has not been demonstrated on any experimental device, it currently only exists in modelling. Also, if considered for driving a part of the plasma bulk current, there might be an offsetting of the current driven with the Ohkawa mechanism, by a reverse trapped particle effect in the bootstrap current, effectively cancelling out the Ohkawa current [64, 65], although that is not experimentally verified.

5.5 Quasi-linear effects and launched power

Including the quasi-linear effects of a Fokker-Planck code like CQL3D leads to better agreement between theory and experiment for instance in DIII-D [52]. Non-linear effects were found in this thesis to possibly have an effect on the current-drive efficiency. Depending on the temperature and density of a simulation, the current-drive efficiency first increases with launched power. Then, a form of saturation and relativistic mass increase dominate, leading to a decrease in current-drive. Significant non-linear effects were mostly found for launched powers of $P \geq 10$ MW. That is, except in the low-density scenario, where a large fraction of power stopped being absorbed at 1 MW already. Here, it is good to note that in this study, all of this power was then deposited in one 'beam' of 51 rays. Experimentally, multiple launchers will be necessary to launch that power, which will decrease the likelihood of depositing the whole 10 MW of EC power on one flux surface. Furthermore, there is an interplay between non-linear effects and energy and

particle transport, as evidenced by [21]. This study not having included a radial transport operator, no definitive conclusions can be drawn on the effect of the launched power on current-drive, absorption and deposition width.

5.6 Reflection on method and models used

In the use of the GENRAY and CQL3D models in this thesis, two elements are identified that give a form of uncertainty: the core coding of the models themselves and the specification of the run parameters. This research has used the models as they are, no core code changes have been made. This means that no mistakes have been added to the existing code, but also that no mistakes that might be there have been identified. The codes have been well benchmarked and tested on experiment [48, 53, 19], but there could still be unknown mistakes underlying the results. The specification of the run parameters of CQL3D in particular is a second issue. There are many options in this code that could change the results in one or the other way. Some of these have been filtered out by comparing the runlists to pre-existing runlists for ITER and DIII-D runs, as described in Chapter 3. The settings used in the code were able to re-create within 10% the driven current profiles for ITER of CQL3D and GENRAY that were found in [48]. Nevertheless, one cannot rule out the possibility that human or conceptual mistakes were made in the process.

More confidence is gained in the results, because the GENRAY and CQL3D codes are both used to calculate the same properties. Using two codes has turned out to be very helpful in providing 'sanity checks' and also to correct mistakes. For instance, it turned out that the amount of cyclotron harmonics considered was defined differently in GENRAY and CQL3D, leading to unexpected behaviour in the CQL3D absorption results for cyclotron harmonics of higher than $n > 2$. This was remedied. As discussed in Chapter 3, a similar situation arose with the Enorm value, where CQL3D predicted completely different values than GENRAY for the wrong settings.

The kinetic profiles that are used in the modelling, are the result of a design objective in ST-F1. These have come out of internal 0-dimensional scaling studies and transport modelling with ASTRA [54]. However, it has not been experimentally verified that these profiles are attainable. Changing the profiles, might impact the driven current and accessibility of the machine. Especially the Ohkawa current drive found in this research is contingent on density profiles. If the density at the edge becomes too large, especially the 85GHz LFS O-mode option will be in cut-off.

Fisch-Boozer current-drive occurs on the order of the pitch-angle scattering time, while electrons are transported radially on the timescale of the particle confinement time. If the radial transport time of electrons is similar to the pitch angle scattering time, the driven current will be broadened and its efficiency possibly reduced [21]. The effect of radial transport on the current drive efficiency is thought to be relatively small, as the high energy electrons should be well confined in ST-F1, just as in DIII-D [53, 66]. This effect could lead to a broadening of the deposition of ECH and ECCD. To verify the degree of broadening and the effect on the driven current, radial transport and diffusion should be taken into account in following studies.

Reflection on model assumptions

The geometric optics equations used in GENRAY to determine the wave properties and propagation, hold when the wavelength of the cyclotron waves is smaller than the local space scale, and when the frequency of the wave is larger than the inverse of the timescale on which the parameters change [50]. In the description of the different dispersion relations in chapter 2, we have already seen that the geometric optics approximation is not always valid near resonances. Corrections for this (Ref. [40, 39]) have been taken into account for the cases with the highest current-drive, which change some of the outcomes in current-drive and absorption. This is mostly due to the different combination of parameters that is optimal, the maximum current-drive that is possible does not change much with these corrections.

The CQL3D code relies on the bounce-averaging assumption that particles are in the low collisionality, bounce average regime. For hot tokamak plasmas, the bounce averaging assumption that $\tau_b \ll \tau_{coll}$ is

often satisfied [51]. The condition for this regime, is that the collisionality $\nu_* \ll 1$. This is defined by the average times a particle is scattered before completing a banana orbit, is given by [67]:

$$v_* \equiv \frac{v_{\text{eff}}}{\omega_{\text{B}}} \sim \left(\frac{R_0}{r}\right)^{3/2} \left(\frac{qR_0}{v_T \tau_{90}}\right) \sim 0.01 \left(\frac{R_0}{r}\right)^{3/2} \left(\frac{qR_0 n_{20}}{T_{\text{k}}^2}\right) \ll 1, \tag{5.3}$$

with ϵ the inverse aspect ratio , q the safety factor, where we are in the banana regime if $\nu_* \ll 1$. This is well fulfilled in this device in the scenarios that are taken into account.

Both the GENRAY and CQL3D code have the capability to run in semi-relativistic or fully relativistic mode. For purposes of ECCD, and ITER like conditions, which correspond well with ST-F1 conditions, both methods are considered to give good results [68].

Synchrotron radiation could be an important energy loss mechanism in hot tokamaks, this radiation particularly causes energy loss in high-energy electron. These high-energy electrons account for a large part of the current-drive with ECCD [69], and this radiation could lead to some energy loss and decrease in current-drive [70]. Synchrotron radiation is theorised to be the main energy loss mechanism in very hot, very large fusion plasmas like the one DEMO will have [71]. The central electron temperature in DEMO is, however, expected to be three times the central temperature of ST-F1. In ST-F1, transport losse will still likely be dominant. Nonetheless, the electrons that carry the current, are for a large part the very energetic electrons. The synchrotron effect on current-drive could thus still be substantial. CQL3D does have the option to take into account this effect, but this required a different run-mode, and this is not implemented in this research. Later research could investigate the effect of synchrotron radiation on the EC current-drive efficiency.

5.7 Engineering limitations and implications

The top launch results suggest that a steerable launcher is necessary for TL. This is also as expected, but this research also points to the fact that it might also be desirable to be able to change the radial location of the launcher or to have available an array of launchers. Steerable launchers are well available and used, so this should not be a problem in implementation, although they would need active control to adapt to different temperatures and densities. The scalings with temperature and density show that the launched wave could quickly lose the absorption and resonance for changing conditions with a top launcher.

The ST has a relatively large ratio of $B_{pol}/B_{tor} \sim 1$ in steady state operation, while when starting up this ratio is 0. That means that the polarisation of the injected wave relative to the magnetic field changes. This effect is especially large for LFS launch, as the change in pitch angle from $B_{pol}/B_{tor} = 0$ to 1 would be 45° . Resulting in about $\sim$ half of the wave being reflected if the X-mode of that same frequency would be in cut-off. The control of these launchers is done mechanically, so the reaction time will in not be enough to adapt to the changing magnetic pitch angle in start-up scenarios. So either real-time polarisation control should be invented, or this effect will have to be taken into account. This research finds options, such as the 200 GHz mode, where the O and X mode waves both drive current in the same direction. In that case, the implementation of a LFS launcher might be possible. The current-drive efficiency possible with this launcher is not as high as the optimal cases of LFS launch, but this would make for a very simple launcher where control is not necessary. The CD efficiency and absorption location is then a superposition of the O and X mode waves dependent on the actual angle of the magnetic field.

In this study, the ability to launch high frequency electron cyclotron waves at high powers with gyrotrons was assumed to be possible. The operation of high-power ($P_{\text{output}} > 1$ MW) gyrotrons such as would be necessary for ST-F1 ECH & CD has been demonstrated for frequencies up to $170GHz$ [72]. For frequencies above $200GHz$, this is not yet the case, although it is likely these high frequencies will also be achieved since lower power (200 kW) gyrotrons are already being tested [72]. Since the highest current-drive frequencies were found for frequencies smaller than 170 GHz, this does not affect the general results.

5.8 Suggestions for future research

Synergetic interaction of EC current-drive with LHCD

Other CD mechanisms increase the parallel speed of the electron distribution. Thus increasing the ECCD CD efficiency. Especially interactions between lower hybrid current drive (LHCD) and ECCD have been observed, as LHCD has the effect of purely increasing the parallel velocity of electrons. To increase the overall and ECCD efficiency, the combination of these two current-drive methods can have a synergetic effect. For an ITER modelling study, this effect has been found to increase the ECCD current-drive by a factor $1.05 - 1.4$ depending on the amount of input power and the fraction of P_{LHCD}/P_{ECCD} [73, 74]. An experiment on the HL-2A tokamak also found a synergistic effect experimentally [75].
Other modelling work with GENRAY and CQL3D on the EAST tokamak, found there could also be a synergy effect between LHCD and Ohkawa current-drive. This study found a potential synergetic factor of up to 2.5 for the far- off-axis region ($\rho > 0.6$) [76]. This mechanisms traps low-speed electrons, that can then be un-trapped and efficiently accelerated by LHCD. This mechanism also has not been demonstrated experimentally.

Bernstein Waves

Research with waves in the electron cyclotron waves for spherical tokamaks mostly focuses on Bernstein waves due to the over-dense configuration [43]. This process shows higher dimensionless current-drive efficiencies than ECCD, so is also promising for a high field tokamak that does not operate in over-dense configuration [77]. It is a more complicated mechanism than ECCD, but is particularly interesting for start-up due to its efficient absorption. Power can be coupled to electron Bernstein waves (EBW) from the outboard side by mode conversion from O-mode or X-mode waves [78]. The mode conversion from each mode is optimised in a different region of the parameter space of parallel wavelength and wave frequency, so it is useful to take, both X-B and O-X-B conversions into account. The mode conversion is usually attempted by using the upper hybrid resonance (UHR). The O-mode, or O-X-B mechanism, works by sending O-mode waves into the plasma at such an angle to the magnetic field, that the O-mode cutoff is located spatially at the same place as the left-handed X-mode cutoff. The power is then coupled to the slow X-mode waves, which in turn mode convert to EBW's at the UHR [78]. This mechanism can be efficient, but the launch angle has to be chosen well, as this is a sensitive mechanism. The X-mode, or X-B, mechanism works by launching fast X-mode waves from the outboard side of the plasma, which goes through the UHR and couples again to the slow X-mode, in turn these convert to EBW's at the high density side of the UHR. This process is less sensitive than the O-X-B mechanism and works for a range of frequencies and launch angles. Start-up with the use of the O-X-B mechanism has been demonstrated at MAST [79].

Iterating transport and current-drive

Since this project has neglected radial transport, and it could have a significant effect on the power and current deposition width and current-drive, it would be relevant to investigate the radial transport and its effect. This might be done by using the ASTRA transport [54] with CQL3D, to iterate for self-consistent tranport, heating and current-drive. This is uniquely possible, as both codes are already implemented at Tokamak Energy. Expanding on this, GENRAY could be integrated into the ASTRA model. The ASTRA model mimics real-time operation of a tokamak, and the GENRAY deposition profiles could be inputted to investigate the effect of current and heat deposition on temperature profiles, transport and other relevant aspects.

Further investigation of the plasma current ramp-up phase and optimisation of ramp-up scenario

The ramp-up phase of the plasma current will be crucial for the operation of ST-F1. This phase is the mid-phase of every discharge, where the plasma current needs to be built up to achieve the level of confinement necessary for efficient operation. This research has shown that high current-drive efficiencies can be achieved for low density operation in ST-F1, but that assumes steady-state operation. CQL3D also has the option to decrease the time-step so much, that analysis of the build-up of the plasma current becomes possible. This can be very relevant in the ramping up of the plasma current.

It has become clear that the low density and relatively low temperature of the ramp-up phase, have implications for the power absorption and possible current-drive. It could be relevant to study the optimal temperature and density parameters to ramp up the current with EC waves as quickly as possible.

Chapter 6

Conclusions

Electron cyclotron heating and current-drive has practical advantages over other methods of heating and current-drive in (spherical) tokamaks. In the design of ST-F1, which will be the first large scale high-field spherical tokamak, the main considered option to provide these functions is E. For the operation of these devices, it is necessary to know the current-drive efficiency and its scaling, to be able to to drive a current at multiple locations in the machine. This research has conducted research into the potential of ECCD current-drive and heating in ST-F1. The study set out to answer the following research questions:

- What is the expected EC current drive efficiency in $\frac{\text{A}}{\text{W}}$ for ST-F1 in different discharge scenarios and for different launcher locations?
- Where in the ST-F1 plasma can how much current be driven?
- How does the maximum current-drive efficiency scale with the central temperature and density in ST-F1.

These research questions are answered question by question. Then, the other general findings are highlighted. Based on the findings and comparison with literature, suggestions for future research and implementation are given. Lastly, the relevance and implications of this work for the development of nuclear fusion is addressed.
Three scenarios were assessed: 1) A design point scenario with a central temperature and density of $T_e = 20$ keV $n_e = 1.37 \cdot 10^{20}/m^3$, 2) A high density scenario with $T_e = 10$ keV $n_e = 3.00 \cdot 10^{20}/m^3$ and 3) A low density scenario with $T_e = 10$ keV $n_e = 1.00 \cdot 10^{19}/m^3$.

The maximum current-drive efficiency that is found in this research for the design point scenario is **0.11** A/W with a 140 GHz O-mode top launcher. The dimensionless current-drive efficiency associated with this is similar to studies in conventional tokamaks. This value of 0.11 A/W is lower than the value of 0.15 A/W that has been used in the design of ST-F1 for auxiliary current-drive efficiency. It was obtained using a top launcher with 140 GHz at a radial location of R=1.8 m. This value would still allow the ST-F1 spherical tokamak to operate at a $Q_{\text{fusion}} > 2$ if other assumptions hold up. If the value of 0.15 A/W that is used in the system scoping code has to be reached, that means that other means of current-drive are necessary or that the design should be revisited to contain higher temperatures and lower density. It is also found, that there are multiple frequencies and launches, including LFS launches, possible to achieve values of (over) 0.1 A/W.

In the high density scenario, the optimal current drive efficiency that is found is 0.024 A/W. This value is reached with a 170 GHz O-mode top launcher. This indicates that when going to significantly higher densities, the frequency of the optimal launchers is due to change. It also indicates, that going to higher densities poses restrictive limits on the operation of ST-F1 related to current-drive. If 1.5 MA would have to be supplied by this launcher at this efficiency, 62.5 MW of EC power would be necessary.

For the low density scenario, which is typical for ramp-up conditions, a maximum achievable current-drive efficiency of 2 A/W is found with a LFS launcher of 125 X-mode GHz. This first harmonic X-mode

current-drive is, however, considered not to be a good option for steady state current-drive, as it is very dependent on the density and could become cut-off very quickly. The top launcher of 125 GHz O-mode was able to drive a current with an efficiency of 0.5 A/W. This means that there is potential for ECCD assisted plasma current ramp-up in these conditions.

The dependence of the current-drive efficiency on the absorption location was established for different launchers and frequencies. This study has shown that current can be driven at every normalised flux surface ρ when using different launchers. This means that ECCD can be a good tool for current-profile tailoring and to control MHD stability.

A general dependence of the current drive efficiency on temperature and density has been found to be similar to the theoretical scaling of $\propto \frac{Te}{ne \ln \lambda}$ with $\ln \lambda$ the Coulomb logarithm. This general dependence is reproduced for a LFS and a top launcher, to be valid near the regions of optimal current-drive.

This study finds that for the ST-F1 tokamak, the Ohkawa current-drive mechanism has a current-drive efficiency that is of the same order of the Fisch-Boozer current-drive mechanism, and for some launcher configurations actually has a higher current-drive efficiency. This Ohkawa current-drive should still be experimentally verified, and for purposes of bulk current-drive, the effect of this current-drive mechanism on the bootstrap current should also be taken into account.

The change of the LFS field pitch could lead to a part of the launched wave changing polarisation during a shot. Part of the wave could be reflected or drive a current on an unintended flux surface. A way to partly overcome the problems with the LFS field pitch has been proposed. This could work by using the second harmonic launched in O-or X-mode to overcome the X-mode cutoff and still drive a significant amount of current. This study finds that launching specific frequencies of second harmonic O- or X-mode from the LFS can be an option for heating and current drive purposes.

Areas of possible further work and implementations and shortcomings of this research were discussed. For this research itself, the radial diffusion and synchrotron radiation inclusion were seen as major options to be implemented.

This work has contributed to the body of literature by researching EC phenomena in high-field spherical tokamaks. The potential of ECCD in ST-F1 and other high-field spherical tokamaks, is found to be good, since the absolute current-drive efficiency in terms of A/W is significantly above that of conventional tokamaks due to the larger size of these tokamaks. The dimensionless current-drive efficiency was found to be similar to the one in conventional tokamaks.

Acknowledgements

I would like to thank the people at Tokamak Energy, especially Steven McNamara and Peter Buxton for their weekly insightful discussions, and Vladimir Shevchenko for his expertise and insight in the world of RF-waves. It is a shame that I haven't been able to physically work at Tokamak Energy with such wonderful people.
I would also like to thank my supervisors from the TU/e, Jan van Dijk and Hugo de Blank for their insight into what is important in a masters project and keen eye for abstract truths about formulas.
A great amount of aprreciation goes out to N. Bertelli of PPPL. A large part of this work could not have gone remotely as quick, thorough or correct without his help in understanding and debugging the GENRAY and CQL3D codes.
My friends and family have been a great comfort in the laborious process of writing a thesis, but most of all in staying relatively normal after working from a small room for a year. Special gratitude goes out to my parents and brother, Erik, Liesbeth and Bart, that are always there and hardly ever miss an opportunity to put me back on the ground when necessary.
Lastly, my gratitude goes out to Sterre, my support and refuge and never ending supply of cheer, for being just that.

Bibliography

[1] Word Energy Council. World energy scenarios 2019. *Word Energy Council: London, UK*, 1, 2019.

[2] Bipartisan Policy Center. Annual energy outlook 2020. *Energy Information Administration, Washington, DC*, 2020.

[3] R Toschi. Nuclear fusion, an energy source. *Fusion engineering and design*, 36(1):1–8, 1997.

[4] Sergio Focardi and Andrea Rossi. A new energy source from nuclear fusion. *Journal of Nuclear Physics, http://www. journal-of-nuclearphysics. com*, 2010.

[5] N Lopes Cardozo. Lecture notes fusion on the back of an envelope.

[6] M Keilhacker, A Gibson, C Gormezano, PJ Lomas, PR Thomas, ML Watkins, P Andrew, B Balet, D Borba, CD Challis, et al. High fusion performance from deuterium-tritium plasmas in jet. *Nuclear Fusion*, 39(2):209, 1999.

[7] J Pamela, A Bécoulet, D Borba, J-L Boutard, L Horton, and D Maisonnier. Efficiency and availability driven r&d issues for demo. *Fusion Engineering and Design*, 84(2-6):194–204, 2009.

[8] A Sykes, AE Costley, CG Windsor, O Asunta, G Brittles, P Buxton, V Chuyanov, JW Connor, MP Gryaznevich, B Huang, et al. Compact fusion energy based on the spherical tokamak. *Nuclear Fusion*, 58(1):016039, 2017.

[9] Egbert Westerhof. Non-inductive current drive. *Fusion Science and Technology*, 61(2T):312–319, 2012.

[10] M Gryaznevich, R Akers, PG Carolan, NJ Conway, D Gates, AR Field, TC Hender, I Jenkins, R Martin, MPS Nightingale, et al. Achievement of record β in the start spherical tokamak. *Physical review letters*, 80(18):3972, 1998.

[11] AW Morris, RJ Akers, GF Counsell, TC Hender, B Lloyd, A Sykes, GM Voss, and HR Wilson. Spherical tokamaks: present status and role in the development of fusion power. *Fusion engineering and design*, 74(1-4):67–75, 2005.

[12] NN Bakharev, FV Chernyshev, PR Goncharov, VK Gusev, AD Iblyaminova, VA Kornev, GS Kurskiev, AD Melnik, VB Minaev, MI Mironov, et al. Fast particle behaviour in the globus-m spherical tokamak. *Nuclear Fusion*, 55(4):043023, 2015.

[13] GM Voss, S Davis, A Dnestrovskij, A Kirk, PJ Knight, M Loughlin, MH O'brien, D Sychugov, A Tabasso, and HR Wilson. Conceptual design of a component test facility based on the spherical tokamak. *Fusion Engineering and Design*, 83(10-12):1648–1653, 2008.

[14] K Tobita, S Nishio, M Sato, S Sakurai, T Hayashi, YK Shibama, T Isono, M Enoeda, H Nakamura, S Sato, et al. Slimcs—compact low aspect ratio demo reactor with reduced-size central solenoid. *Nuclear fusion*, 47(8):892, 2007.

[15] S Nishio, K Tobita, T Isono, Y Nakamura, M Sato, S Sakurai, M Yamauchi, T Nishitani, K Tani, S Sengoku, et al. Technological and environmental prospects of low aspect ratio tokamak reactor vector. Technical report, 2005.

[16] AE Costley. Towards a compact spherical tokamak fusion pilot plant. *Philosophical Transactions of the Royal Society A*, 377(2141):20170439, 2019.

[17] Valentin Igochine et al. *Active control of magneto-hydrodynamic instabilities in hot plasmas*. Springer, 2015.

[18] M Henderson, G Saibene, C Darbos, D Farina, L Figini, M Gagliardi, F Gandini, T Gassmann, G Hanson, A Loarte, et al. The targeted heating and current drive applications for the iter electron cyclotron system. *Physics of plasmas*, 22(2):021808, 2015.

[19] CC Petty, RJ La Haye, TC Luce, DA Humphreys, AW Hyatt, J Lohr, R Prater, EJ Strait, and MR Wade. Complete suppression of the m= 2/n= 1 neoclassical tearing mode using electron cyclotron current drive in diii-d. *Nuclear Fusion*, 44(2):243, 2004.

[20] E Poli, G Tardini, H Zohm, E Fable, D Farina, L Figini, NB Marushchenko, and L Porte. Electron-cyclotron-current-drive efficiency in demo plasmas. *Nuclear Fusion*, 53(1):013011, 2012.

[21] Ronald Prater. Heating and current drive by electron cyclotron waves. *Physics of Plasmas*, 11(5):2349–2376, 2004.

[22] NJ Fisch and Allen H Boozer. Creating an asymmetric plasma resistivity with waves. *Physical Review Letters*, 45(9):720, 1980.

[23] Tihiro Ohkawa. Steady state operation of tokamaks by rf heating. *General Atomics Report GA-A13847*, 1976.

[24] PW Zheng, XY Gong, XQ Lu, JJ Cao, LH He, QH Huang, S Deng, JF Lin, and YJ Zhong. Comparative study of fisch-boozer and ohkawa current drive mechanisms for electron cyclotron waves. *Physics of Plasmas*, 25(7):072501, 2018.

[25] Xi Chen, Ron Prater, Craig Petty, John Lohr, David Su, Lang Lao, and Vincent Chan. Top launch for higher off-axis electron cyclotron current drive efficiency. In *EPJ Web of Conferences*, volume 203, page 01004. EDP Sciences, 2019.

[26] Y R Lin-Liu, V S Chan, and R Prater. Electron cyclotron current drive efficiency in general tokamak geometry, 2003.

[27] N B Marushchenko, H Maassberg, and Yu Turkin. Electron cyclotron current drive calculated for ITER conditions using different models. In *Nuclear Fusion*, volume 48, page 7, 2008.

[28] P W Zheng, X Y Gong, X Q Lu, J J Cao, L H He, Q H Huang, S Deng, J F Lin, and Y J Zhong. Comparative study of Fisch-Boozer and Ohkawa current drive mechanisms for electron cyclotron waves. *Physics of Plasmas*, 25(7):72501, 2018.

[29] Thomas Howard Stix. *The theory of plasma waves*. McGraw-hill, 1962.

[30] Thomas H Stix. *Waves in plasmas*. Springer Science & Business Media, 1992.

[31] Donald Gary Swanson. *Plasma waves*. CRC Press, 2003.

[32] Donald Gary Swanson. *Plasma kinetic theory*. CRC Press, 2008.

[33] Nathaniel J Fisch. Theory of current drive in plasmas. *Reviews of Modern Physics*, 59(1):175, 1987.

[34] A Krämer-Flecken. Microwave and far infrared diagnostics. *Fusion science and technology*, 45(2T):418–425, 2004.

[35] Syunichi Shiraiwa, Kazuaki Hanada, Makoto Hasegawa, Hiroshi Idei, Hiroshi Kasahara, Osamu Mitarai, Kazuo Nakamura, Nobuhiro Nishino, Hideaki Nozato, Mizuki Sakamoto, et al. Heating by an electron bernstein wave in a spherical tokamak plasma via mode conversion. *Physical review letters*, 96(18):185003, 2006.

[36] L Friedland and IB Bernstein. Geometric optics in plasmas characterized by non-hermitian dielectric tensors. *Physical Review A*, 22(4):1680, 1980.

[37] IB Bernstein, L Friedland, AA Galeev, and RN Sudan. Handbook of plasma physics. *MN Rosenbluth and RZ Sagdeev eds*, 1(3.2):367–418, 1983.

[38] E Mazzucato, I Fidone, and G Granata. Damping of electron cyclotron waves in dense plasmas of a compact ignition tokamak. *The Physics of fluids*, 30(12):3745–3751, 1987.

[39] MD Tokman, E Westerhof, and MA Gavrilova. Wave power flux and ray-tracing in regions of resonant absorption. *Plasma physics and controlled fusion*, 42(2):91, 2000.

[40] E Westerhof, MD Tokman, and MA Gavrilova. Ray-tracing through ec resonance and the wave energy flux. *Fusion engineering and design*, 53(1-4):47–51, 2001.

[41] M Bornatici, R Cano, O De Barbieri, and F Engelmann. Electron cyclotron emission and absorption in fusion plasmas. *Nuclear Fusion*, 23(9):1153, 1983.

[42] M Bornatici. Theory of electron cyclotron absorption of magnetized plasmas. *Plasma Physics*, 24(6):629, 1982.

[43] CB Forest, PK Chattopadhyay, RW Harvey, and AP Smirnov. Off-midplane launch of electron bernstein waves for current drive in overdense plasmas. *Physics of plasmas*, 7(5):1352–1355, 2000.

[44] Jakub Urban, Joan Decker, Yves Peysson, Josef Preinhaelter, Vladimir Shevchenko, Gary Taylor, Linda Vahala, and George Vahala. A survey of electron bernstein wave heating and current drive potential for spherical tokamaks. *Nuclear Fusion*, 51(8):083050, 2011.

[45] YR Lin-Liu, VS Chan, and R Prater. Electron cyclotron current drive efficiency in general tokamak geometry. *Physics of Plasmas*, 10(10):4064–4071, 2003.

[46] DA Ehst and CFF Karney. Approximate formula for radiofrequency current drive efficiency with magnetic trapping. *Nuclear fusion*, 31(10):1933, 1991.

[47] RW Harvey, MG McCoy, and GD Kerbel. Power dependence of electron-cyclotron current drive for low-and high-field absorption in tokamaks. *Physical review letters*, 62(4):426, 1989.

[48] R Prater, D Farina, Yu Gribov, RW Harvey, AK Ram, Y-R Lin-Liu, E Poli, AP Smirnov, F Volpe, E Westerhof, et al. Benchmarking of codes for electron cyclotron heating and electron cyclotron current drive under iter conditions. *Nuclear fusion*, 48(3):035006, 2008.

[49] PV Minashin, AB Kukushkin, and RW Harvey. Modelling of the electron cyclotron resonance heating and current drive in the t-15-md tokamak with genray and cql3d codes. *Ser. Thermonuclear Fusion*, 40(2):65–72, 2017.

[50] AP Smirnov and RW Harvey. The genray ray tracing code. *CompX Report CompX-2000-01*, 2001.

[51] RW Harvey and MG McCoy. The cql3d fokker-planck code. In *Proceedings of the IAEA Technical Committee Meeting on Simulation and Modeling of Thermonuclear Plasmas*, pages 489–526, 1992.

[52] CC Petty, R Prater, J Lohr, TC Luce, WR Fox, RW Harvey, JE Kinsey, LL Lao, and MA Makowski. Detailed measurements of the electron cyclotron current drive efficiency on diii-d. *Nuclear fusion*, 42(12):1366, 2002.

[53] CC Petty, R Prater, TC Luce, RA Ellis, RW Harvey, JE Kinsey, LL Lao, J Lohr, MA Makowski, and K-L Wong. Effects of electron trapping and transport on electron cyclotron current drive on diii-d. *Nuclear fusion*, 43(8):700, 2003.

[54] P.N. Yushmanov G. V. Pereverzev. Astra, automated system for transport analysis. `https://w3.pppl.gov/~hammett/work/2009/Astra_ocr.pdf`. Accessed: 9 March, 2020.

[55] Ronald H Cohen. Effect of trapped electrons on current drive. *The Physics of fluids*, 30(8):2442–2449, 1987.

[56] Bastiaan J Braams and Charles FF Karney. Conductivity of a relativistic plasma. *Physics of Fluids B: Plasma Physics*, 1(7):1355–1368, 1989.

[57] EF Jaeger, LA Berry, RW Harvey, JR Myra, RJ Dumont, CK Phillips, DN Smithe, DB Batchelor, PT Bonoli, MD Carter, et al. Self-consistent full-wave/fokker-planck calculations for ion cyclotron heating in non-maxwellian plasmas. In *AIP Conference Proceedings*, volume 787, pages 23–30. American Institute of Physics, 2005.

[58] TC Luce, YR Lin-Liu, RW Harvey, G Giruzzi, PA Politzer, BW Rice, JM Lohr, CC Petty, and R Prater. Generation of localized noninductive current by electron cyclotron waves on the diii-d tokamak. *Physical review letters*, 83(22):4550, 1999.

[59] G Ramponi, D Farina, MA Henderson, E Poli, O Sauter, G Saibene, H Zohm, and C Zucca. Physics analysis of the iter ecw system for optimized performance. *Nuclear Fusion*, 48(5):054012, 2008.

[60] N Bertelli, AA Balakin, E Westerhof, and MN Buyanova. Eccd calculations in iter by means of the quasi-optical code. *Nuclear Fusion*, 50(11):115008, 2010.

[61] MW Brookman, ME Austin, KW Gentle, CC Petty, DE Ernst, Y Peysson, J Decker, and K Barada. Experimental measurement of ech deposition broadening: Beyond anomalous transport. In *EPJ Web of Conferences*, volume 147, page 03001. EDP Sciences, 2017.

[62] J Stober, L Barrera, K Behler, A Bock, A Buhler, H Eixenberger, L Giannone, W Kasparek, M Maraschek, A Mlynek, et al. Feedback-controlled ntm stabilization on asdex upgrade. In *EPJ Web of Conferences*, volume 87, page 02017. EDP Sciences, 2015.

[63] A Snicker, E Poli, O Maj, L Guidi, A Köhn, H Weber, G Conway, M Henderson, and G Saibene. The effect of density fluctuations on electron cyclotron beam broadening and implications for iter. *Nuclear Fusion*, 58(1):016002, 2017.

[64] G Taylor, PC Efthimion, CE Kessel, RW Harvey, AP Smirnov, NM Ershov, MD Carter, and CB Forest. Efficient generation of noninductive, off-axis, ohkawa current, driven by electron bernstein waves in high β, spherical torus plasmas. *Physics of plasmas*, 11(10):4733–4739, 2004.

[65] RW Harvey and RO Dendy. A trapped-passing fluid model for tokamak neoclassical transport. *Physics of Fluids B: Plasma Physics*, 4(4):902–910, 1992.

[66] RW Harvey, O Sauter, R Prater, and P Nikkola. Radial transport and electron-cyclotron-current drive in the tcv and diii-d tokamaks. *Physical review letters*, 88(20):205001, 2002.

[67] Jeffrey P Freidberg. *Plasma physics and fusion energy*. Cambridge university press, 2008.

[68] YM Hu, YJ Hu, and YR Lin-Liu. A relativistic theory of electron cyclotron current drive efficiency. *Fusion Science and Technology*, 59(4):684–689, 2011.

[69] F Albajar, M Bornatici, G Cortes, J Dies, F Engelmann, J Garcia, and J Izquierdo. Importance of electron cyclotron wave energy transport in iter. *Nuclear Fusion*, 45(7):642, 2005.

[70] M Bornatici and U Ruffina. The effect of radiative slowing down on current drive by electron cyclotron radiation in fusion plasmas. *Nuclear fusion*, 35(5):613, 1995.

[71] J Garcia, G Giruzzi, JF Artaud, V Basiuk, J Decker, F Imbeaux, Y Peysson, and M Schneider. Analysis of demo scenarios with the cronos suite of codes. *Nuclear Fusion*, 48(7):075007, 2008.

[72] MKA Thumm, GG Denisov, Keishi Sakamoto, and Minh Quang Tran. High-power gyrotrons for electron cyclotron heating and current drive. *Nuclear Fusion*, 59(7):073001, 2019.

[73] A Polevoi, A Zvonkov, T Oikawa, A Kuyanov, M Shimada, A Saveliev, and Yu Gribov. Assessment of current drive efficiency and the synergetic effect for eccd and lhcd and the possibility of long pulse operation in iter. *Nuclear fusion*, 48(1):015002, 2008.

[74] SY Chen, BB Hong, Y Liu, W Lu, J Huang, CJ Tang, XT Ding, XJ Zhang, and YJ Hu. Numerical analysis on the synergy between electron cyclotron current drive and lower hybrid current drive in tokamak plasmas. *Plasma Physics and Controlled Fusion*, 54(11):115002, 2012.

[75] Lu Wei, Chen Shao-Yong, Tang Chang-Jian, Bai Xing-Yu, Zhang Xin-Jun, and Hu You-Jun. Nonlinear dependence of the synergetic current by the combined effect of eccd and lhcd on the power ratio on hl-2a tokamak. *Chinese Physics Letters*, 30(6):065203, 2013.

[76] PW Zheng, XY Gong, XH Yin, LH He, XQ Lu, JJ Cao, QH Huang, S Deng, JF Lin, YJ Zhong, et al. Synergy effect of the ohkawa current drive of electron cyclotron waves and the lower hybrid current drive: a new mechanism. *Nuclear Fusion*, 59(5):054003, 2019.

[77] H Idei, T Onchi, K Mishra, H Zushi, T Kariya, T Imai, O Watanabe, R Ikezoe, K Hanada, M Ono, et al. Electron heating of over-dense plasma with dual-frequency electron cyclotron waves in fully non-inductive plasma ramp-up on the quest spherical tokamak. *Nuclear Fusion*, 60(1):016030, 2019.

[78] AK Ram and Steven Donald Schultz. Excitation, propagation, and damping of electron bernstein waves in tokamaks. *Physics of Plasmas*, 7(10):4084–4094, 2000.

[79] VF Shevchenko, MR O'Brien, D Taylor, AN Saveliev, et al. Electron bernstein wave assisted plasma current start-up in mast. *Nuclear Fusion*, 50(2):022004, 2010.